MICROMECHANICAL STUDIES OF PROGRESSIVE FAILURE OF S2 GLASS/TOUGHENED EPOXY COMPOSITES AND COMPOSITE JOINTS

by

CHIN KEUNG CHEUNG

A dissertation submitted to the Graduate Faculty in Engineering in partial fulfillment of the requirements for the degree of Doctor of Philosophy, The City University Of New York

2006

ProQuest Information and Learning Company
300 North Zeeb Road
P.O. Box 1346
Ann Arbor, MI 48106-1346

This manuscript has been read and accepted for the Graduate Faculty in Engineering in satisfaction of the dissertation requirement for the degree of Doctor of Philosophy.

Prof. Benjamin Liaw

Date — Chair of Examining Committee

Dean Mumtaz K. Kassir

Date — Executive Officer

Prof. Benjamin Liaw, Dept of Mechanical Engineering, The City College

Prof. Feridun Delale, Dept of Mechanical Engineering, The City College

Prof. Jackie Li, Dept of Mechanical Engineering, The City College

Prof. Hong-Hui Yu, Dept of Mechanical Engineering, The City College

Prof. Assimina A. Pelegri, Mechanical & Aerospace Engineering, Rutgers University

Supervision Committee

THE CITY UNIVERSITY OF NEW YORK

ABSTRACT

MICROMECHANICAL STUDIES OF PROGRESSIVE FAILURE OF S2 GLASS/TOUGHENED EPOXY COMPOSITES AND COMPOSITE JOINTS

by

CHIN KEUNG CHEUNG

Adviser: Professor Benjamin Liaw

In this dissertation, micromechanical studies of progressive failure of S2 glass/toughened epoxy composites and composite joints under tensile loading tested from low to elevated temperature are presented. Because of their superiority in light-weight, high specific stiffness, strength and toughness S2 glass/toughened epoxy composites have been used to replace traditional metals and conventional composites with brittle resin in many engineering structures. One of the salient features of the thermomechanical behavior of unidirectional S2-glass fiber/toughened-epoxy matrix composites is that when loaded under uniaxial tension, its dominant failure mode is fiber breakage, instead of the more-frequently observed matrix cracking in most commercial composite materials with untoughened matrix. The main objective of this research is to use micromechanics-based experimental-analytical-numerical approaches to investigate the progressive failure of this advanced composite under uniaxial tensile load at various temperatures.

Two micromechanical approaches were adopted for the study of progressive failure of dog-bone tensile specimens: a Mechanics-of-Materials approach for unidirectional lay-up configuration and a 3-D Elasticity approach for cross-ply, angle-ply and quasi-isotropic lay-up configurations. The dominant failure mode for unidirectional

specimens was fiber breakage. Using Strength of Materials and the rule of mixture, stress-strain curves for unidirectional specimens were predicted in good agreement with experimental results. For the cross-ply, angle-ply and quasi-isotropic configurations, the dominant failure modes were transverse matrix cracking and/or shear failure. A 3-D Elasticity approach was adopted to simulate the stress-strain curves and failure progression. The predictions matched the experimental results very well.

For the composite strips with a center hole and pin-joint specimens, several design parameters (e.g., hole/pin size, the distance from the hole center of the pin-joint specimen to edge, stacking sequence, temperature, etc.) were varied. Damaged-induced stress-strain curves for [0°], [90°] and [±45°] dog-bone specimens under uniaxial tension were first characterized experimentally to document damage evolution along the longitudinal direction (i.e., fiber breakage), perpendicular to the longitudinal direction (i.e., transverse matrix cracking) and shear failure, respectively. A nonlinear elastic orthotropic material model based on these data was then proposed. This constitutive law was implemented in a commercial finite element code, ANSYS, to calculate the apparent stress-strain curves for composite strips with a center hole and to map their associated patterns of progressive failure. Good agreement was found between the numerical simulations and experimental results.

With the extensive experimental-analytical-numerical studies conducted in this research, the progressive failure behaviors of S2 glass/toughened epoxy composites and composite joints were understood in details. The conclusions obtained by this study should help engineers improve their future design in using this advanced composite.

ACKNOWLEDGMENTS

I would like to dedicate this work to my parents and family, who have been giving me endless support for so many years. I would also like to acknowledge my mentors, Professors Benjamin Liaw and Feridun Delale, who offered continuous valuable advice, guidance and suggestions. In addition, I would like to thank Professors Jackie Li and Hong-Hui Yu from Department of Mechanical Engineering at City College of New York as well as Professor Assimina Pelegri from Department of Mechanical and Aerospace Engineering at Rutgers University for serving on my Ph.D. Dissertation Committee.

I would also like to thank my research colleague: Messrs. Jianjun Liu, Yanxiong Liu and Huapei Wan, and all my friends who have worked in the Material Processing and Solid Mechanics Laboratory, Department of Mechanical Engineering, City College of New York.

Finally, I would like to thank the financial and equipment support provided by U.S. Army TACOM-TARDEC (Contract No. DAAE07-96-C-X-121, Program Managers: Mr. Gregory Chapelle and Dr. Basavaraju B. Raju), by PSC-CUNY (RF 62466-00 31, RF 63431-00 32, RF 64437-00 33, RF 65738-00 34, RF 66475-00 35 and RF 67514-00 36) and by the CUNY Graduate School and University Center. Part of equipment used in this study was purchased through funding from New York State Graduate Research and Technology Initiative (NYS-GRTI).

TABLE OF CONTENTS

LISTS OF TABLES

LISTS OF FIGURES

CHAPTER 1

INTRODUCTION

The concept of composite material is very old. According to historians, ancient Egyptians constructed straw-reinforced clay bricks. The first fiberglass boat was made in the early 1940's [4]. The use of composite materials has continued to grow as new applications were discovered. This is due to many advantages of composite materials: lightweight, high specific values in stiffness and strength, high fatigue tolerance, etc., for applications to diverse structures from aircrafts, spacecrafts, submarines and surface ships to robot components, prosthetic devices, civil structures, automobiles and rail vehicles. The primary use of composite materials for those applications is fiber-reinforced materials [5]. The U.S. Army is interested in using composite materials for military vehicles such as armored tanks because of the afore-mentioned advantages. Indeed, partial funding of this research was provided by U.S. Army Tank-Automotive and Armaments Command-Tank Automotive Research, Development, and Engineering Center (TACOM-TARDEC). In this research, progressive failure in layered composites made of S2 glass/toughened epoxy was studied using micromechanics-based approaches. Since its matrix is made of toughened epoxy, the failure mode of this composite with unidirectional lay-up configuration tested under uniaxial tensile load is fiber brakeage. However, research on fiber brakeage of composite materials is limited. On the other hand, research on the matrix cracking has been well studied. Some simple modifications on those previous investigations were proposed in this study to account for the effect of change in failure mode. Effect of stress concentrations in this class of composites (e.g., composites with holes, pin-loaded composite joints, etc.) will also be considered.

The main objective of this research is to understand extensively about the progressive failure of S2 glass/toughened epoxy composites under tensile loading at various temperatures. With the proposed experimental-analytical-numerical approach, this study provides in-depth analyses of the different failure modes dominating failure progression in S2 glass/toughened epoxy composites with various types of lay-up configurations. For instance, the uncommon fiber breakages occurred in the unidirectional composites under tensile loading as well as the transverse matrix cracking and/or shear failure in cross-ply, angle-ply and quasi-isotropic composites. Results from the extensive studies conducted in this research for the progressive failure behaviors of S2 glass/toughened epoxy composites and composite joints should lead to valuable information for engineers to improve their future design in using this class of advance composites.

The following chapters are broken down as Chapter 2: Literature Review, which summarizes previous studies conducted by other researchers in areas relevant to the current work; Chapter 3: Methods of Approach, which provides an overview of the methods used in this dissertation; Chapter 4: Micro-Mechanics Based Study of S2 Glass/Toughened Epoxy Composite Tensile Specimens, which gives detail descriptions of the experimental work and theoretical models on the study of the composites under uniaxial tension at various temperatures; . The experimental work and finite element simulations of composite strips with stress concentrations are presented in Chapter 5: Composite Strips with a Center Hole or a Pin-Joint. The last two chapters are Chapter 6: Conclusions and Chapter 7: References, respectively.

CHAPTER 2

LITERATURE REVIEW

In this literature review, three main areas were considered: 2.1 studies of damage in composites, 2.2 studies of damage of composite strips with openings or joints and 2.3 other related topics.

2.1 Studies of Damage in Composites

In the past few decades, many research areas on thermomechanical behaviors of composite materials have been explored, varying from the effects of composite constituents to different failure models. For example, Aboudi and Benveniste [13] studied the constitutive relations for cracked metal matrix composites. The prediction could be used for isotropic inelastic materials, including cracked unidirectional and laminated metal matrix composites. Aveston and Kelly [23] investigated the tensile first cracking strain and strength of hybrid composites and laminates. Some suggestions about the dimension of the fiber and the thickness of the transverse ply are important for the study. Grande *et al*. [74] studied fiber-matrix bond strengths of glass, ceramic and metal matrix composites. Sun *et al*. [184] proposed a continuum theory for a laminated medium. Voyiadjis and Park [202] developed the interfacial and local damage analyses of metal matrix composites. Wei and Sankar [207] investigated the effects of processing on the mechanical behavior of silicon nitride (Si_3N_4) ceramics through their microstructure. Nuismer and Tan [159] deliberated an approximate elasticity theory solution, which was given for the stress-strain relations of cracked composite lamina. It is shown explicitly that the cracked lamina compliances depend upon the overall laminate construction in which the lamina is contained. Laws [135] discussed the problem of determining the

overall thermoplastic moduli of transversely isotropic composites. The classical self-consistent method was used to obtain precise formulae for the overall moduli of certain fiber- and platelet-reinforced composites. Manne and Tsai [149] studied design optimization of laminated composite plates using Tsai-Wu criterion. Aboudi [16] took into account the effect of wave propagation in damaged composite materials. His paper is especially helpful for dynamic responses of composites subject to impulsive loading. Auersperg *el al.* [22] considered the behavior of mixed-mode interfacial fracture toughness. Benveniste [26] investigated the problem of contact between the constituents in composites. Birman and Byrd [28] explored the effect of matrix cracks on damping in unidirectional and cross-ply ceramic matrix composites. Chamis and Minnetyan [32] presented an equation, called multi-factor-interaction-model (MFIM), which is of a computationally effective product form representing coupled interactions. Even though the model is versatile, it is lacking details of application. Chang *et al.* [37,40] performed tests on Fiberite T300/1034-C graphite epoxy composites to measure the characteristic lengths in tension and in compression and the rail shear strength. The results indicated the variability of rail shear strength with the volume fraction of zero degree plies in the laminate. This research group also analyzed laminated composite structures with a thick cross-section. A three-dimensional finite element program was developed to calculate the stresses, strains, and deformations of thick laminated composites. Chow and Lu [47] investigated the development of evolution laws of anisotropic damage. Some suggestions of conducting experiments were given in their paper. Christensen and Lo [48] presented a series of solutions for the effective shear moduli of two types of composite materials. Delameter *et al*. [57] provided an infinite elastic solid containing a doubly periodic

rectangular array of slit-like cracks. The solid was subjected to a uniform stress resulting in a state of plane strain. DeTeresa and Larsen [58] were able to derive interaction parameters for the Tsai-Wu tensor polynomial theory of strength for composite materials. Dwivedi and Espinosa [62] modeled intersonic crack propagation in fiber-reinforced composites with contact and cohesive laws. Fanella and Krajcinovic [66] and Fonseka and Krajcinovic [69] developed a nonlinear analytical model based on the principles of continuum damage mechanics, which was proposed for the stress-strain behavior of fiber reinforced concrete subjected to monotonic compressive and tensile loadings. Hale [78] reviewed the physical properties of composite materials. Hashin *et al*. [86-91] used a variational approach to investigate the theory of the elastic behavior of multiphase and cracked materials. He then studied the self-consistent scheme approximation on conductivity of particulate composites, and the elastic behavior of fiber reinforced materials of arbitrary transverse phase geometry. Hill [95-98] provided a detailed analysis in his self-consistent mechanics of composite materials. He also studied the elastic properties of reinforced solids. In addition, Hill explained the theory of mechanical properties of fiber-strengthened materials and its elastic behavior. Hwang and Han [107] studied analytically the cumulative damage during fatigue. Kachanov [116,117] provided a microscopically-based model of brittle-elastic behavior of compressed rock. He also discussed the continuum model of media with cracks [118]. Kedlaya and Pelegri [122] produced an analytical model for failure prediction of graphite/epoxy laminates with induced intermittent surge in applied load during fatigue. Krajcinovic and his associates [128-132,182,183] studied the brittle deformation processes using a mesomechanical model. Later he also proposed a geometrically consistent representation for the set of

internal variables defining an arbitrary distribution of flat, planar microcracks and studied the creep of structures within a continuous damage mechanics framework. Laws [133-135] gave a direct solution to the problem of determining the interaction energy associated with a slit crack in an arbitrarily anisotropic solid. He also detailed the overall thermoelastic moduli of transversely isotropic composites according to the self-consistent method. Rawlinson [171] developed the use of cross-ply and angle-ply composite test specimens to generate improved material property data. Reifsnider *et al*. [172] provided the mechanics for the responses of composite laminates with damage initiation, damage growth, stress redistribution, fracture, and nondestructive testing. Srolovitz and Beale [181] showed computer simulation of failure in an elastic model with randomly distributed defects. Sumarac and Krajcinovic [182,183] focused on the formulation of a self-consistent process model for a perfectly elastic solid weakened by an ensemble of microcracks. Talreja [185,186] investigated the continuum mechanics characterization of damage in composite materials. Vinson and Woldesenbet [201] studied fiber orientation effects on high strain rate properties of graphite/epoxy composites. Wang and Crossman [204] suggested improved numerical (finite element) procedure for investigating the stress fields in symmetrically laminated composites of finite dimensions. Willis [211] showed bound and self-consistent estimates of the overall properties of anisotropic composites. Yan and Mall [213] presented a cohesive-shear-lag model, which was developed to analyze the cycling stress-strain behavior of unidirectional fiber-reinforced ceramic matrix composites. Zhang *et al.* [220] studied the tensile failure mechanisms of ceramic and polymer matrix composites at room and elevated temperatures.

Other researchers studied the effect of fiber ordinations. Tao and Sun [193] conducted an experimental investigation in interlaminar fracture behavior and toughness of multi-directional composite laminates. The finding is that the delamination crack always ends up along the 0°/θ° interface. Allen, Harris, Groves and Norell [19] also wrote a paper about experimental study of stiffness loss in cross-ply laminates with curved matrix cracks when three or more 90^o plies are stacked in succession. The results and the experiment data were compared. Meanwhile, Whitney's paper [209] determined analytically the effective of elastic moduli and thermal expansion coefficients for a $[\text{laminate}/90°_m]_S$ composite containing transverse crack through the middle $90°_m$ layers. Rhee and Chi [173] studied the elastic work factor η of multi-directional CLS specimen, which was calculated numerically as a function of delamination length. Once the effect of stacking sequence on η was determined, the value was then used to estimate fracture toughness G_c for graphite/epoxy composites, which had ±45° plies in them. Finally, Schön [174] determined coefficients of friction of composite delamination surfaces.

New composite materials have also been studied by many researchers. For instance, progressive failure of woven composite panels under high transverse pressure was studied by Feng *et al*. [67]. Also, Gommer *et al.* [72] used Tsai-Wu failure criterion to measure the tensile strengths for woven fabric composite materials at different angles. Chen *et al.* [42] studied damage and failure mechanisms of glass fiber reinforced polyphenylene sulfide. Khondleer *et al.* [124] studied knitted composites materials under tensile and compressive load types.

The concern of matrix cracking is particularly popular. Wang *et al.* [203] dealt with simulation for growth of multiple matrix cracks in composite laminates subjected to both static and fatigue loads. A new concept of effective flaws was introduced which replaces the conventional constant ply strength criterion. Dvorak *et al.* [60,61] determined the overall stiffness and compliances, thermal expansion coefficients, and stress and strain lamina, which contained a given density of open transverse cracks, and was subjected to uniform mechanical loads and thermal changes. The evolution procedure was based on the self-consistent method and was similar, in principle, to that used in finding elastic constants of unidirectional composites. They assumed that cracks were initiated from a nucleus created by localized fiber debonding and matrix cracking. Cracks may propagated in two directions on planes, which were parallel to the fiber axis and perpendicular to the mid-plane of the ply. In general, for thin plies, the crack propagated along with fiber axis. For the thick plies, the crack propagated perpendicular to fiber axis. Their theory predicted a significant increase in strength with decreasing ply thickness in constrained thin plies. The strength of the thick plies was found to be constant, but it might be reduced by pre-existing damage. Strengths of plies of intermediate thickness and of unconstrained thick plies were evaluated as well. These are examples of many papers dealing with matrix cracking.

Aboudi and Benveniste [13], presented two different methods to determine the effective elastic moduli of a cracked body under plane stress or plane strain condition. They compared their models with one self-consistent method, and found that the latter approach underestimates the moduli and yields an unrealistic result. Aboudi [14] proposed a self-consistent method to predict the loss stiffness of cracked solids, which

involved a doubly periodic rectangular array of cracks. However, the major failure mode was the matrix cracking. Allen *et al.* [18,20] developed a theoretical model based on continuum mechanics and applied it to matrix cracking in laminated composites. The model seems to have a good agreement with their experimental results. However, the authors suggested further development and extensive experimental verification are needed. In addition, the model is limited to transverse matrix cracks only. Attiogbe and Darwin [21] utilized a self-consistent energy method to develop a model to predict the effective moduli of a transversely isotropic cracked solid. Benveniste and Aboudi [25] developed a continuum model for fiber-reinforced materials with debonding. Daniel and Anastassopolulos [51] studied failure mechanisms under the microscope in a cross-ply silicon carbide glass-ceramic composite under axial tensile loading. Failure initiation took place in the 90° layer. It took the form of radial matrix cracks around the fibers, followed by interfacial cracks, which in turn coalesced into transverse macrocracks. Daniel and Lee [52] demonstrated damage development under monotonic loading in five cross-ply graphite/epoxy laminates. The laminates exhibited three characteristic ranges of varying stiffness. Daniel *et al.* [52-54] explained how the model gave closed-form solutions for stress distributions, crack densities and reduced stiffness of the damaged layers and the laminate. The research group also investigated failure modes and criteria for their occurrence in composite sandwich columns and beams. Delale *et al.* [56] explained tensile damage behavior of ceramic matrix composites under high temperatures. Dougill and Rida [59] extended possible applications of a material idealization that had been termed the progressively fracturing solid. Groves *et al*. [75] attempted to identify the mechanisms for the initiation and growth of matrix cracks and to

determine the effect of matrix cracking on the stiffness loss in cross-ply laminates. Hahn and Tsai [77] discussed the behavior of composite laminates after initial failures. Harris *et al*. [83] theorized stiffness loss in quasi-isotropic laminates due to microstructural damage. Herakovich *et al*. [92] demonstrated damage in composite laminates, where the effects of transverse cracks were concerned. Highsmith and Reifsnider [93] presented paper showing the results of an experimental program and an analytical modeling, indicating that most of the observed matrix cracking can be predicted and the effects on stiffness calculated with various degrees of accuracy depending upon the sophistication of the model used. Budiansky and O'Connell [30] first investigated elastic moduli of a cracked body using the self-consistent method. Hoenig [99-101] studied the effects of elastic moduli of a non-randomly cracked body. He also investigated the near-tip behavior of a crack and a flat elliptical crack in a plane anisotropic elastic body. Horii and Nemat-Nasser [102] followed up with the overall moduli of solids with microcracks. Aboudi [15] studied stiffness reduction of cracked bodies. Ilankamban and Krajcinovic [110] constructed a constitutive theory for progressively deteriorating brittle solids. Johnson and Chang [113,114] performed study of the impact of matrix cracking-initiated damage on the response and the strength of composite laminates subjected to uniaxial tension. Kassapoglou and Lagace [120] developed a closed form solution for the interlaminar stress field in angle-ply and cross-ply laminates. Krajcinovic and Fonseka [128] theorized the continuous damage theory of brittle materials. Krajcinovic *et al*. [132] developed a phenomenological theory describing the process of gradual damage of brittle rods leading to their ultimate rupture. Lee and Daniel [138] provided a simplified shear lag analysis using a progressive damage scheme, which was proposed for cross-ply

composite laminates under uniaxial tensile loading. Liaw *et al*. [143,144] discussed the tension-induced damages of S2 glass/toughened epoxy composites at room and elevated temperatures. They also provided an experimental technique for *in situ* tensile testing of ceramic matrix composites at elevated temperatures within a scanning electron microscope. Lim and Hong [145] predicted the transverse cracking and stiffness reduction in cross-ply laminated composites. Masters and Reifsnider [150] comprised an investigation of cumulative damage development in quasi-isotropic graphite/epoxy laminates. Ogin, *et al*. [162] examined the stiffness reduction due to matrix cracking in a [0°/90°]s glass fiber reinforced plastic (GFRP) laminate under both quasi-static and fatigue loading. The stiffness reduction was shown to be directly proportional to the density of cracks, which accumulated in the transverse plies. Peters [168] demonstrated the strength distribution of the 90° ply in [0°/90°/0°] graphite-epoxy laminates. Shannag [177] introduced the interface debonding in fiber reinforced cement-matrix composites. Talreja [186] examined the effects of transverse cracking on the stress-strain responses of composite laminates. Tan and Nuismer [187] showed that the progressive matrix cracking of composite laminates that contained a cracked 90^o ply and was subjected to uniaxial tensile or shear loading could be modeled using a fracture mechanics approach and an elasticity theory. Tsai *et al*. [196,197] investigated the behavior of cracked cross-ply composite laminates under shear loading. They further discussed the progressive matrix cracking of cross-ply composite laminates under biaxial loading. Yokozeki and Aoki [216] assessed the damage process of transverse cracks in cross-ply and quasi-isotropic toughened CFRP laminates under static loading. In 1991, Abrate [17] published a paper,

which gave an overview of the problem of matrix cracking in laminated composite materials. Several types of loading with the parameters were reviewed.

The understanding of progressive failure due to fiber failure has also been looked into even though this area of research needs to explore more. Mi *et al.* [152] constructed a model for progressive mixed-mode delamination in fiber composites. Non-linear finite element method was used. Although, the method worked, however, the meshes used in their non-linear finite element computer program were coarse, as the authors described them too excessively "Peaky"! Meanwhile, Huang [103] studied the progressive failure process in a multidirectional composite laminate subjected to an arbitrary thermo-mechanical loading. He used classical laminate theory and maximum normal stress criterion. However, only the last ply failure stress in x-direction was compared. Irvine and Ginty [111] also studied the progressive fracture of fiber composite utilizing Real-time Ultrasonic C-Scan (RUSCAN) experimental facility and the Composite Durability Structure Analysis (CODSTRAN) computer code. The final stresses were compared for graphite/epoxy angle-ply laminates with different fiber orientations. Indeed, the previous two papers only dealt with the ultimate stress. That is, their studies are not "progressive failure" at all. Harris *et al.* [84] detected fiber cracking by acoustic emission. Cheung *et al.* [46] studied the temperature effect on progressive damage in S2 glass/toughened epoxy composites. A micromechanics-based finite element analysis was developed to obtain a damage-induced stress-strain curve. Good agreement was found between the numerical prediction and experimental data. Christensen [49] derived the necessary and sufficient conditions for composite lamina failure within a laminate from separate criteria for fiber failure and for matrix failure. He then developed a 3-dimensional lamination

theory to forecast the "out-of-plane" stresses in a thick composite [50]. However, the paper lacks of experimental support. Tandon and Kim [192] examined micromechanical failure modes in a unidirectional composite when subjected to tensile loading parallel to the fibers.

2.2 Studies of Damage of Composite Strips with Openings or Joints

The research in composites with holes or pin-joints has always been very popular due to their importance in engineering applications. Experimental technique to improve data collection is one of the popular areas. Baumann *et al.* [24] investigated new scanning technique using computed tomograghy (CT) X-ray. Some of the images were presented with dye to enhance the film radiographs and photographs. Bogdanovich and Yushanov [29] presented a novel 3-D variational approach aiming at analyzing crack propagation in adhesively bonded composite joints. They found that the loading conditions for the bonded joint and Mode I and Mode II deformations significantly contributed to the progressive failure process. Hart-Smith [85] addressed two of the best-known spurious sources of scatter in the measured strengths of fibrous composite laminates: the design of the test coupons and their imperfect manufacture and testing. Highsmith [94] studied the edge replication of transverse cracks for laminated composites in his paper.

Cheng and Tsao [44] studied the problems and made suggestions for using saw drill and candlestick drill in composite materials to generate holes. Hult and Janson [104] investigated the material damage in structural analysis. Sehgal *et al*. [176] used diagraph modeling and matrix approach to develop a failure mode analysis of rolling element bearings. Shimokawa *et al*. [178] showed the effect of isothermal aging on ultimate strength of high-temperature composite materials for SST structures. Ueng and Lin [199]

inspected the stress concentrations in composite laminates. Whitney and Nuismer [208] studied the stress fracture criteria for laminated composites containing stress concentrations.

Different types of joints have also been studied by many researchers. Camanho and Matthews [31] developed a 3-D finite element model to predict damage progression and strength reduction of mechanically fastened joints in carbon fiber-reinforced plastics that fail in bearing, tension and shear-out modes. The model is based on a three-dimensional failure criterion and a constitutive equation that takes into account the effects of damage on the material elastic properties. The comparison of experimental and numerical predictions was satisfactory. Chang *et al.* [39] studied progressive failure in bolted composite joints. Their method was similar to Chang *et al.* [34], which considered pinned composite joints instead. Dano *et al.* [55] conducted stress and failure analyses of mechanically fastened joints in composite laminates. Chen and Lee [43] studied failure analyses of composite laminates with bolted joints under bending loads. The approach involved maximum stress theory and delamination criterion. Ericksson *et al*. [64] presented a special purpose finite element method for designing multiple-fastener composite joints subject to an arbitrary loading condition. Garbo and Ogonowskit [70] provided strength predictions of composite laminates with unloaded fastener holes. Hamada, *et al*. [79] performed a study on predicting the joint strength of mechanical fasteners. Hung and Chang [105,106] studied the bearing failure and response of a mechanically fastened laminated composite joint. They further investigated the strength and failure of bolted composite joints subjected to bypass loads. Jiang *et al*. [112] performed experimental investigation and finite element analysis to explore the

mechanisms of the early stage self-loosening of bolted joints under transverse cyclic loading. Kallmeyer *et al.* [119] developed a finite element model for predicting time-dependent deformations and damage accumulation in laminated composite bolted joints. Kim *et al*. [127] included both nonlinear mechanical properties and fabrication residual thermal stresses of adhesive in the stress calculation of adhesively bonded tubular single lap carbon/epoxy composite-steel joints. Lee and Hahn [136] discussed the computational modeling of composite integral fit joints. Lee and Cho [137] predicted the tensile load capability of co-cured steel-composite tubular single lap joints due to thermal degradation. Lin and Jen [146] considered the strength of bolted and bonded single-lapped composite joints in tension. Lyer, *et al*. [148] conducted a three-dimensional finite element analysis of an elastic, double rivet-row, and aluminum alloy lap joint with non-countersunk aluminum rivets. Schulz *et al*. [175] developed a tension-mode fracture model for bolted joints in laminated composites. Tang [191] studied the failure of composite joints under combined tension and bolt loads. Tay *et al*. [194] presented the results of accelerated curing of adhesives in bonded joints by induction heating. Wang *et al*. [205] completed an investigation, which was performed to study the bearing failure of mechanically fastened fiber-reinforced laminated composite joints. Yang [214] designed and provided analysis of composite pipe joints under tensile loading.

Researchers also explored the area of pin-loaded joints. Chang *et al.* [33-36,39-41] conducted extensive studies on the design of composite laminates containing pin-loaded or mechanically fastened holes. They showed how the design parameters could be found to result in maximum failure load and in maximum failure load per unit weight. Later Chang and his colleagues developed a method to predict the

failure mode of fiber reinforced composite laminates containing one or two pin-loaded holes. The stress distribution in the laminate was calculated using finite element method, and next applying the Yamada-Sun failure criterion in conjunction with the proposed failure hypothesis to predict the failure load and failure mode. They also calculated the failure strength and failure modes of composite laminates containing a pin-loaded hole for materials exhibiting nonlinearly elastic behaviors. The authors claimed that their prediction is more accurately than those methods used only linear stress-strain analysis when the laminates show nonlinear behavior. Chang *et al.* [37,38] studied progressive damage of notched laminate composites subjected to tensile loading. The authors applied classical lamination theory to predict the stresses and the strains. Combining with a proposed property degradation model, they used the calculated stress-strain results to predict the damage accumulated in laminates. Chang [39] also studied the effect of pin load distribution on the strength of pin-loaded holes in laminated composites. A finite element method implemented with Yamada-Sun failure criterion and Chang-Scott-Springer characteristic curve was used to predict the strengths and failure modes. Hyer *et al*. [108] displayed the effects of pin elasticity, clearance, and friction on the stresses around the hole edge in a pin-loaded orthotropic plate. Whitworth *et al.* [210] conducted failure analysis of composite pin loaded joints. Jong [115] investigated the stresses around pin-loaded holes in elastically orthotropic or isotropic plates. Lessard and Shokrieh [142] showed two-dimensional modeling of pinned-joint failure in composites. Liu *et al*. [147] compared the thickness effects on pinned joints for composites. Tsai and Morton [198] investigated the failure stress analysis of a pin-loaded composite plate. Xiao *et al*. [212] developed a calculation method based on M-CLT (Modified Classical

Lamination Theory) for the friction coefficient of a CFRP (carbon fiber reinforced plastic) composite laminate edge. Zhang *et al*. [218] conducted an investigation for the study of the effects of friction on the three-dimensional stress state around pin-loaded holes in laminated composites. Zhang and Ueng [219] investigated the stresses around a pin-loaded hole in orthotropic plates. Aktaş *et al*. [218] conduct experimental and numerical studies of strengths of composite pinned-plates. Okutan *et al*. [164-166] studied failure strength of pin-loaded woven-glass-fiber reinforced epoxy laminates. İçten *et al.* [109] investigated progressive failure analysis of pin-loaded of woven composites. Kelly *et al.* [123] studied the effect of bolt-hole clearance on bearing strength of CFRP composites.

Etheridge *et al*. [65], they showed the effect of lay-up and constraint on tensile notch strength. Genin and Hutchinson [71] analyzed mechanical attachments for a brittle-matrix fiber-reinforced cross-ply composite. Goncalves and Almeida [73] proposed a method based upon the maximum hole deformation to predict the tensile strength of carbon/epoxy laminates containing one or two pin loaded holes. Kim *et al*. [125] compared notched strength and fracture criterion in fabric composite plates containing a circular hole. Kim *et al*. [126] studied the plane stress analysis of two rigid circular inclusions. Nguyen [155] wrote about three-dimensional modeling of damage in laminated composites containing a central hole. Ohki *et al*. [163] studied the fracture behavior and strength in a flat braided bar with a circular hole tested by static and fatigue loading. Shokrieh *et al*. [179,180] studied the progressive fatigue damage in composite materials. Tan [187-190] developed a progressive failure model for laminated composites containing stress concentrations subjected to in-plane loading. They then proposed

approximated stress analyses for orthotropic composite laminates containing an elliptical opening under uniaxial normal loads. Ukadgaonker [200] developed stress analysis of a plate containing two circular holes having tangential stresses. Yang and Chow [215] described the anisotropic states of stress, strain and damage of unidirectional graphite/epoxy composite plates containing a central hole subjected to off-axis uniaxial tension.

2.3 Other Related Topics

Thomason [195] considered the size effect on glass-fiber-reinforced polyamide 6.6 (E and S types glasses). He found that the size of the fibers was very important for the composite strength. Other areas of research in composite materials include the following: Fenske and Vizzini [68] developed a new criterion, which accounts for the full stress state in the resin layer. Ely *et al*. [63] in their experimental study studied the corrosion effect of the glass fiber/polymer composite materials. Prabhu and Lambros [170] investigated 3-D nature of stress filed in the near tip region of a cracked orthotropic plate. Their study shows that the stress filed depends on fiber orientation and thickness of the composite materials, but is independent of crack length. Meske and Schnack [151] used X-ray to measure stress. The advantage of using X-ray is that 3-D stresses in the interior can be measured. Peel and Jensen [167] studied elastomer (rubber) matrices reinforced by specially impregnated fibers. Yu and Davidson [217] presented in their paper a 3-dimensional crack tip element for the determination of energy release rate. This element can also be used to represent different types of laminated plates containing delaminations. Kawai *et al*. [121] studied T800H/Epoxy composites under room and high temperatures (100°C) off-axis fatigue. A fatigue damage mechanics model was

developed using non-dimensional effective stress, and its capability to describe the off-axis *S-N* (stress amplitude *vs.* number of cycle) relationship for the composites. Comparisons with the classical fatigue failure models for composites were also presented in their paper. Berhan *et al*. [27] looked into the damage effect in bio-structures. They suggested the 3D nature of bonds might be simulated very well in 2D simulations for the overall network behavior. Cheung *et al*. [45] studied bending-induced damages in composites at room and elevated temperatures. Guan and Gibson [76] described the development of a finite element model and a closed-form model for studying viscoelastic damping in woven fabric-reinforced polymer matrix composites. Lemaitre *et al*. [139-141] explained the application of damage concepts to predict creep-fatigue failures and developed a continuous damage mechanics model for ductile fracture. The model later was used to predict plastic or creep fatigue failure in structures. Mikata and Taya, [153] articulated a stress field in a coated continuous fiber composite under thermo-mechanical loadings. Nemat-Nasser and Taya, [154] discussed the effective moduli of an elastic body containing periodically distributed voids. Noh and Whitcomb [156] simulated the progressive damage of thick viscoelastic laminates with the homogenization technique. Nuismer and Labor [157,158] used the average stress failure criterion for tension and compression testing, which gave acceptable strength results. O'Brien [160] described the stiffness change as a nondestructive damage measurement. Oda [161] provided a method for evaluating the effect of crack geometry on the mechanical behavior of cracked rock masses. Prabhu and Lambros [170] investigated the three dimensional nature of stress fields in the near tip region of a cracked orthotropic plate. Wang *et al*. [206] developed a

theoretical analysis of cyclic fatigue damage and associated anisotropic property degradation in a random short-fiber composite.

Finally, the above literature review certainly cannot exhaust all previous studies related to this dissertation. Several books containing information worthwhile mentioned in this review are given in references [1-9].

CHAPTER 3

METHODS OF APPROACH

In this research, a hybrid experimental-theoretical approach was adopted to study the progressive failure mechanisms of S2 glass/toughened epoxy composite dog-bone shaped specimens and strips with a center hole or a pin-joint at various temperatures. All specimens were made of 24-ply laminae with a 44% fiber volume fraction. Various stacking sequences were considered: the unidirectional $[0°]_{24\text{-ply}}$ and $[90°]_{24\text{-ply}}$, the cross-ply $[0°_3/90°_3]_{2S}$ and $[90°_3/0°_3]_{2S}$, the angle-ply $[+45°_3/–45°_3]_{2S}$ and the quasi-isotropic $[0°_3/+45°_3/90°_3/–45°_3]_S$, $[90°_3/+45°_3/0°_3/–45°_3]_S$ $[+45°_3/0°_3/–45°_3/90°_3]_S$. Experimental results showed that the failure mechanism in each stacking sequence and specimen type was dominated by different failure modes. For this reason, three different theoretical-numerical approaches were adopted to analyze the experimental results.

3.1 Unidirectional [0°] Tensile Specimens

Since the matrix was made from toughened epoxy, when unidirectional specimens were under tensile loading, fiber breakage occurred. This peculiar type of failure mode was not commonly found in most composites. In this study, a micromechanical approach based on mechanics of materials and the rule of mixtures was developed for theoretical modeling of damage progression in this type of specimens.

3.2 Cross-Ply, Angle-Ply and Quasi-Isotropic Tensile Specimens

For cross-ply, angle-ply and quasi-isotropic tensile specimens, the dominant failure modes are transverse matrix and shear cracking. Analytical procedures based on the method developed by Daniel and his associates [51,52,138,196,197] were adopted to predict the progressive failure for those configurations.

3.3 Composite Strips with a Center Hole or a Pin-Joint

Because of their complicated geometry, micromechanics-based approach, which accounts for the damaged mechanical behaviors of individual fiber, the matrix and their interface, is no longer feasible for analyzing composite strips with stress concentration (e.g., a center hole or a pin-joint). Instead, the damaged composite was deemed as a nonlinear elastic orthotropic material with finite orthotropic failure strains. The damaged nonlinear elastic orthotropic stress-strain curves were obtained from the above-mentioned tensile tests of the dog-bone specimens. That is, the tensile stress-strain curves from [0°], [90°] and [±45°] specimens are treated as the longitudinal, transverse and shear properties of an orthotropic composite. These nonlinear orthotropic curves were then incorporated into the commercially available general-purpose finite element software: ANSYS for numerical simulations of progressive failure of composite strips with stress concentration tested in this research.

CHAPTER 4

MICRO-MECHANICS BASED STUDY OF S2 GLASS/TOUGHENED EPOXY COMPOSITE TENSILE SPECIMENS

4.1 The Experimental Work

4.1.1 The material and the specimens

The material used in this research is S2-glass/toughened epoxy composite. The fibers are S2 glass (tape code: 91C, 20 end round glass, OCF S-2 449AA 750 yd/lb.) procured from Owens Corning. The matrix is toughened epoxy resin (NCT-301) procured from Newport Adhesives and Composites, Inc. Composiflex, Inc., manufactured the composite specimens with a specified fiber volume fraction (44%) for use in an MTS universal testing system equipped with an environmental chamber. Four types of stacking sequences were used in this study: the $[0°]_{24\text{-ply}}$ unidirectional, the $[0°_3/90°_3]_{2S}$ cross-ply, the $[+45°_3/–45°_3]_{2S}$ angle-ply and the $[0°_3/+45°_3/90°_3/–45°_3]_S$ quasi-isotropic. For tensile tests, two types of dog-bone shaped specimens with dimensions shown in Figure 4-1.1 were adopted. Type 1 geometry was used for all lay-up configurations except for the [0°] specimens whereas Type 2 geometry was used exclusively for the [0°] specimens.

4.1.2 Tensile testing in MTS

4.1.2.1 Description of experiments: The dog-bone shaped specimens were tested under uniaxial tension in the environmental chamber of a 22-kip MTS servo-hydraulic universal testing machine at –60°C, –20°C, room temperature, 75°C, and 125°C, respectively. Specimens of all lay-up configurations were tested at these five temperatures with the exception of the unidirectional [0°] specimens, which were tested only at the room and high temperatures. Figure 4-1.2 shows the MTS universal testing

system with the servo-hydraulic grips and the environmental chamber. Both loading and elongation histories were recorded through a National Instruments (NI)-DAQ based LabView data acquisition system. For high and low temperature testing, both the specimen and hydraulic grips were soaked at the desired temperature for at least 20 minutes before running the experiment. This was to avoid thermal mismatching between the specimen and the hydraulic grips. In addition, a digital camera was connected to a computer to capture the surface strain development and crack evolution of the specimen. The captured images were analyzed using NI-IMAQ and Photoshop software.

From the vendors, the moduli of elasticity along the longitudinal and transverse directions of the orthotropic fibers and of the isotropic matrix used in this study are 79.5, 7.84 and 14.0 GPa, respectively. Table 4-1.1 lists the experimentally-measured composite longitudinal stiffness E_c corresponding to five stacking sequences. As a comparison the table also lists E_c based on the conventional rule of mixtures. The discrepancies may result from manufacturing imperfection.

Table 4-1.1 Composite stiffness for various lay-up configurations tested in MTS.

Lay-Up Configuration	Composite Stiffness, E_c (GPa)	
	Measured	Calculated from Rule of Mixtures
$[0°]_{24\text{-ply}}$	45.0	44.6
$[0°_3/90°_3]_{2S}$	25.5	26.6
$[0°_3/45°_3/90°_3/–45°_3]_S$	21.0	21.5
$[+45°_3/–45°_3]_{2S}$	14.0	14.6
$[90°]_{24\text{-ply}}$	13.0	13.0

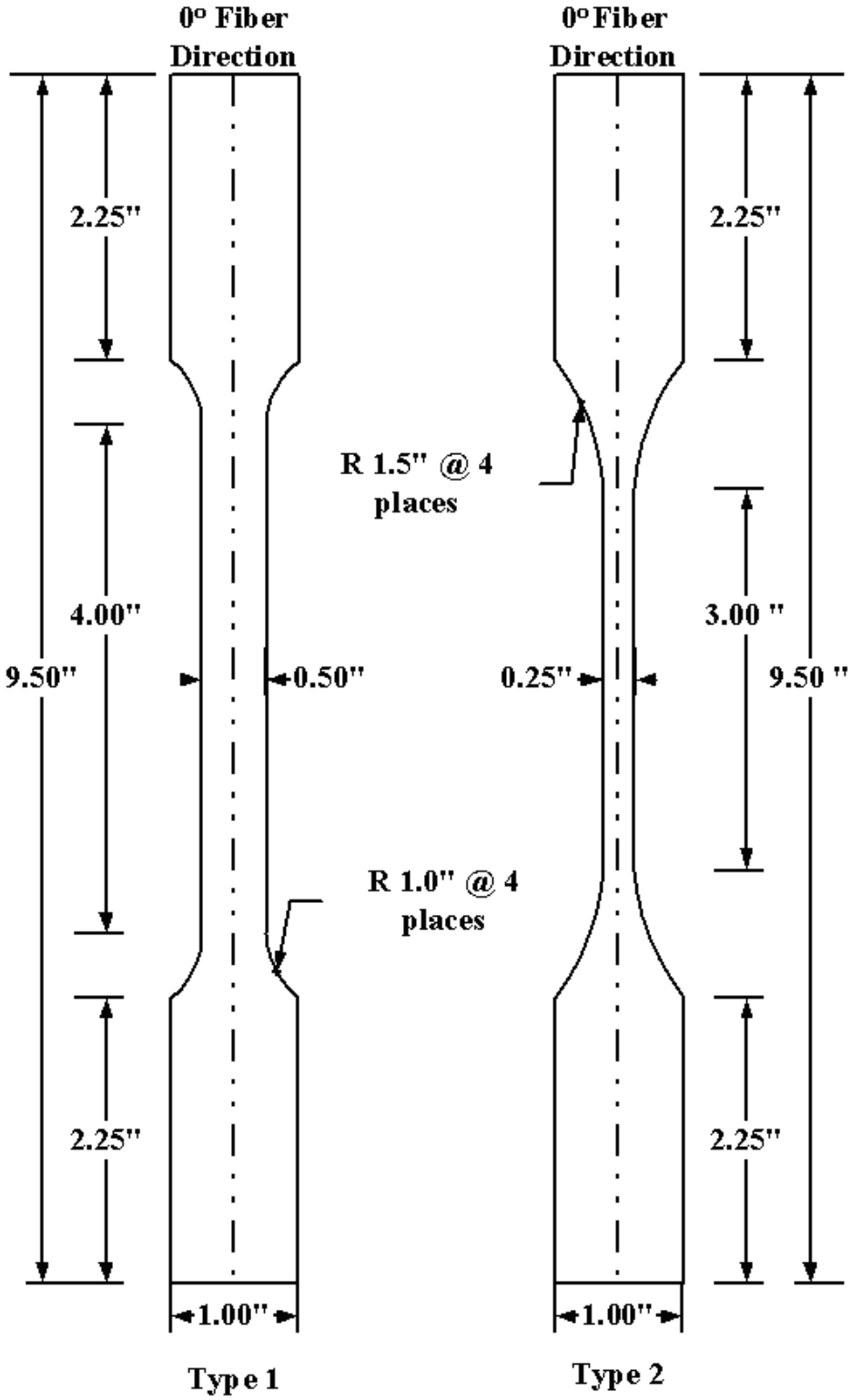

Figure 4-1.1 Dog-bone shaped specimens used in MTS tensile testing.

Figure 4-1.2 The MTS universal testing machine equipped with hydraulic grips and an environmental chamber.

4.1.2.2 <u>Results</u>: The results at room temperature for the unidirectional $[0°]_{24\text{-ply}}$, the cross-ply $[0°_3/90°_3]_{2S}$, the angle-ply $[+45°_3/–45°_3]_{2S}$ and the quasi-isotropic $[0°_3/+45°_3/90°_3/–45°_3]_S$ composites are shown in Figure 4-1.3. For each stacking sequence at least 4 specimens were tested and the results look quite consistent. For all configurations, as shown in Figure 4-1.3, the stress-strain curves have a linear portion corresponding to the undamaged state, followed by a non-linear portion corresponding to the damaged state.

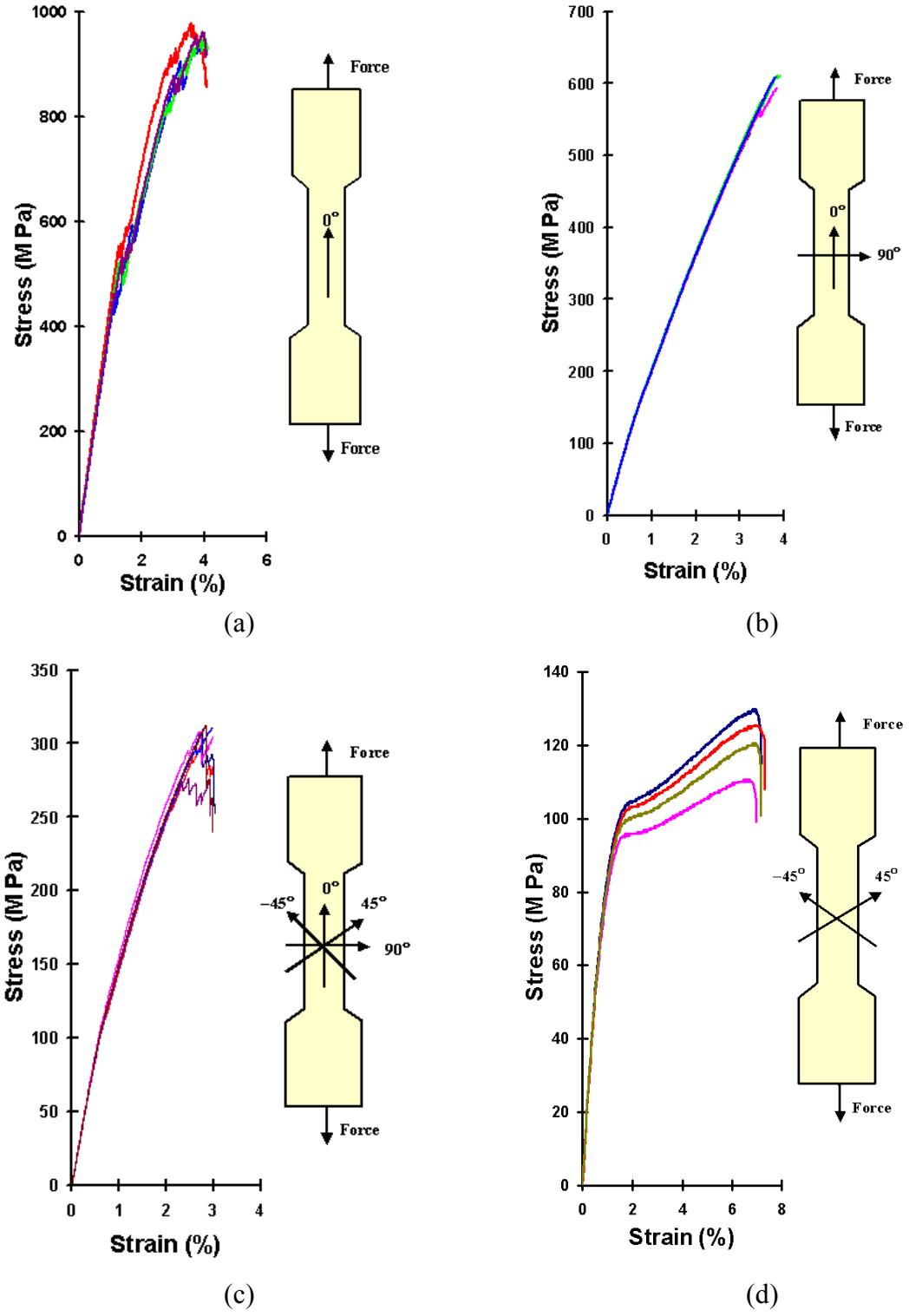

Figure 4-1.3 Tensile-induced damaged stress-strain curves for (a) unidirectional $[0°]_{24\text{-ply}}$, (b) cross-ply $[0°_3/90°_3]_{2S}$, (c) quasi-isotropic $[0°_3/+45°_3/90°_3/-45°_3]_S$ and (d) angle-ply $[+45°_3/-45°_3]_{2S}$ composites at room temperature.

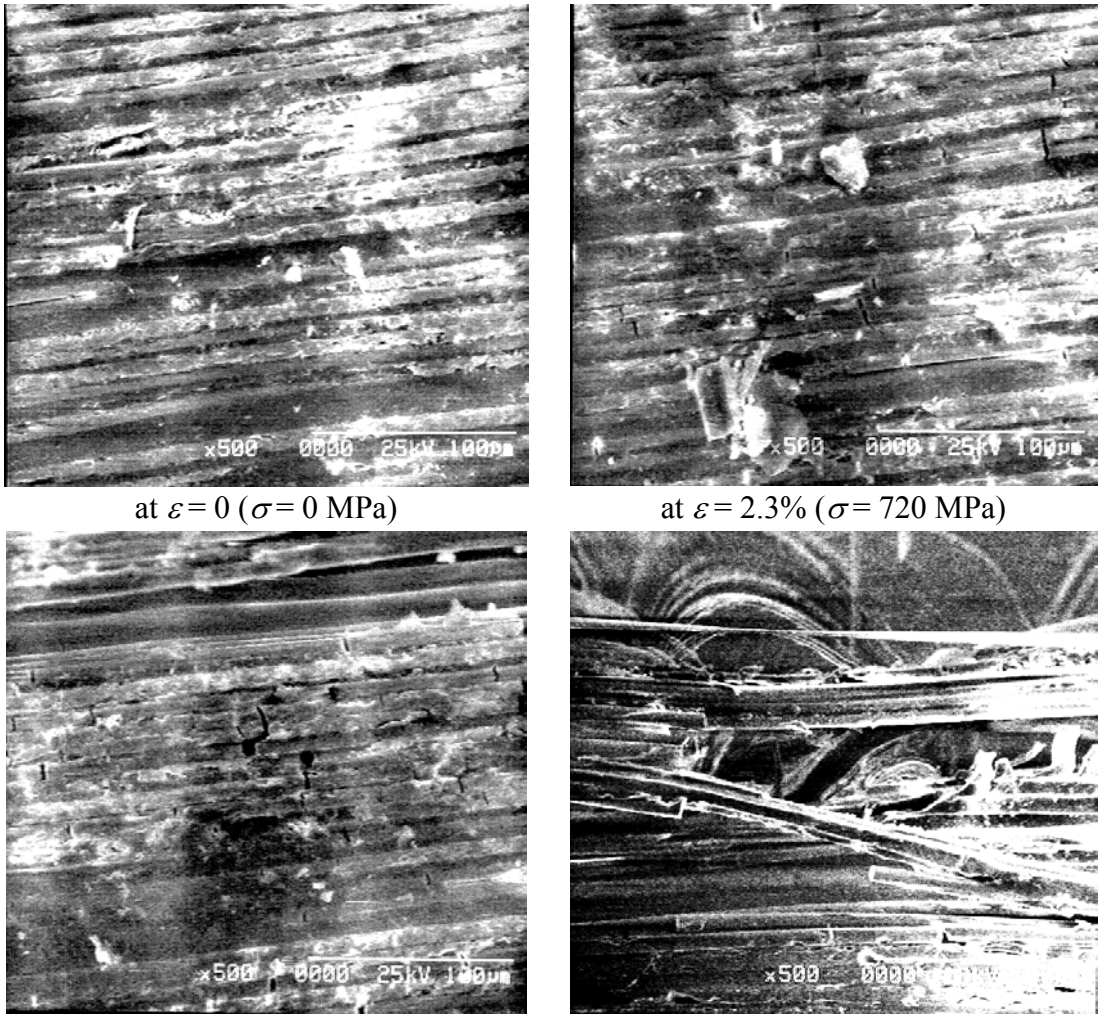

at $\varepsilon = 0$ ($\sigma = 0$ MPa) at $\varepsilon = 2.3\%$ ($\sigma = 720$ MPa)

at $\varepsilon = 3.8\%$ ($\sigma = 930$ MPa) at $\varepsilon = 4.0\%$ ($\sigma = 950$ MPa, Fiber Breakage)

Figure 4-1.4 *In situ* SEM microfractographs showing fiber breakage and fiber-matrix interfacial debonding in a [0°] composite.

The shape of the non-linear portion varies with various lay-up configurations, which have different failure modes. For instance, as shown in Figure 4-1.4, which are four microfractographs taken *in situ* (i.e., pictures taken while the specimen was under loading) in a Hitachi S-2400 scanning electron microscope (SEM), fiber breakage followed by fiber-matrix interfacial debonding is the dominant failure mode, in unidirectional $[0°]_{24\text{-ply}}$ specimens. On the other hand, shear cracking along the fiber-matrix interface followed by delamination is the dominant failure mode in angle-ply

$[+45°_3/-45°_3]_{2S}$ specimens, as shown in the SEM microfractograph, Figure 4-1-5, while the dominant failure mode in cross-ply $[0°_3/90°_3]_{2S}$ specimens is transverse matrix cracking in the 90° layers followed by damage in the 0° layers.

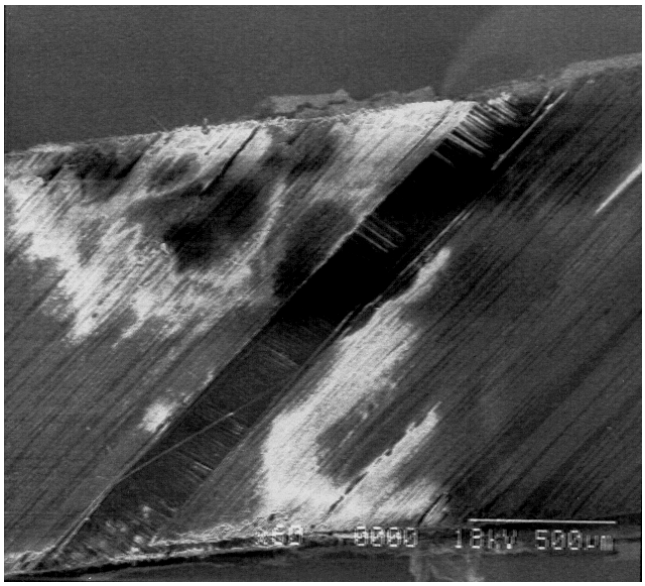

Figure 4-1.5 *In situ* SEM microfractograph showing shear failure and delamination in a [±45°] composite.

As mentioned earlier, a digital camera was used to take series of pictures of the cross-ply, the angle-ply and the quasi-isotropic composites during tensile testing. Figure 4-1.6 shows the damage patterns of a cross-ply $[90°_3/0°_3]_{2S}$ specimen at 0.5%, 1.0%, 1.5%, 2.0%, 2.5% and 3.5% of strain, respectively. During the initial loading phase, as shown in Figures 4-1.6(a) and (b) the number of transverse matrix cracks in the 90° layers increased as the strain increased. Thus one can conclude that the initial failure mode for the [90°/0°]-type (hence, intuitively, the [0°/90°]-type) of specimens is transverse matrix cracking. However, the number of cracks became saturated when the strain level was increased further, as depicted in Figures 4-1.6(c) to (f). This behavior indicated that other failure modes, e.g., fiber breakage and fiber-matrix interfacial debonding in the 0° layers may become dominant.

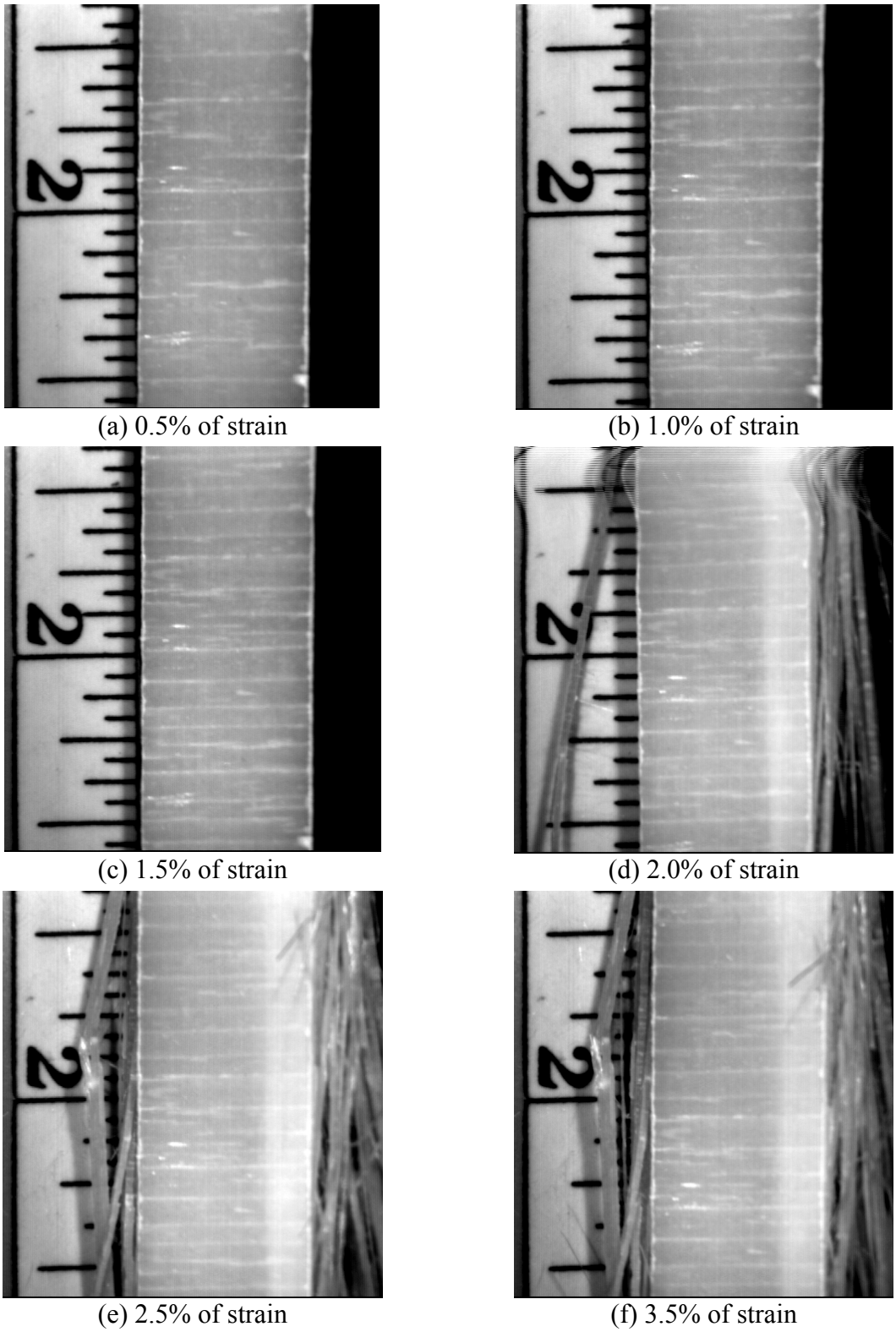

(a) 0.5% of strain (b) 1.0% of strain

(c) 1.5% of strain (d) 2.0% of strain

(e) 2.5% of strain (f) 3.5% of strain

Figure 4-1.6 Fractographs of a cross-ply $[90°_3/0°_3]_{2S}$ specimen taken during room-temperature tensile testing at different strain levels.

Figure 4-1.7 shows the failure progression of an angle-ply $[+45°_3/–45°_3]_{2S}$ specimen at 1.0%, 2.0%, 3.0%, 4.0%, 5.0% and 7.5% of strain, respectively. As shown in Figures 4-1-7(a) and (b), shear cracks along fiber-matrix interfaces occurred in one group of the 45° layers (say, the +45° layers) in the beginning. When higher strain was applied, these shear cracks became saturated and shear cracking appeared in the other group of the 45° layers (say, the –45° layers), as indicated in Figures 4-1-7(c) to (e). Eventually, the ensuing delamination between the +45° and the –45° layers, as shown in Figure 4-1.7(f), caused the final catastrophic failure.

For quasi-isotropic specimens, in stead of the conventional lay-up configuration of $[0°_3/+45°_3/90°_3/–45°_3]_S$, the stacking sequences: $[90°_3/45°_3/0°_3/–45°_3]_S$ and $[45°_3/0°_3/–45°_3/90°_3]_S$ were used for easy picture taking. Figure 4-1.87 shows the progressive failure of a $[90°_3/45°_3/0°_3/–45°_3]_S$ specimen at 0.5%, 1.0%, 1.5%, 2.0%, 2.5% and 3.0% of strain, respectively, whereas Figure 4-1.9 shows the damage evolution in a $[45°_3/0°_3/–45°_3/90°_3]_S$ specimen loaded at 0.5%, 1.0%, 1.5%, 2.0%, 2.5% and 3.0% of strain, respectively. As expected, the combination of these two figures indicates that failure progression in the quasi-isotropic lay-up configuration should be the combination of the cross-ply and angle-ply configurations. That is, the weakest 90° layers will be damaged first due to transverse matrix cracking. It should be followed by shear cracking in one group of 45° layers then the other group of 45° layers. The 0° layers should fail the last. During this process, delamination may have occurred and further weakened the composite.

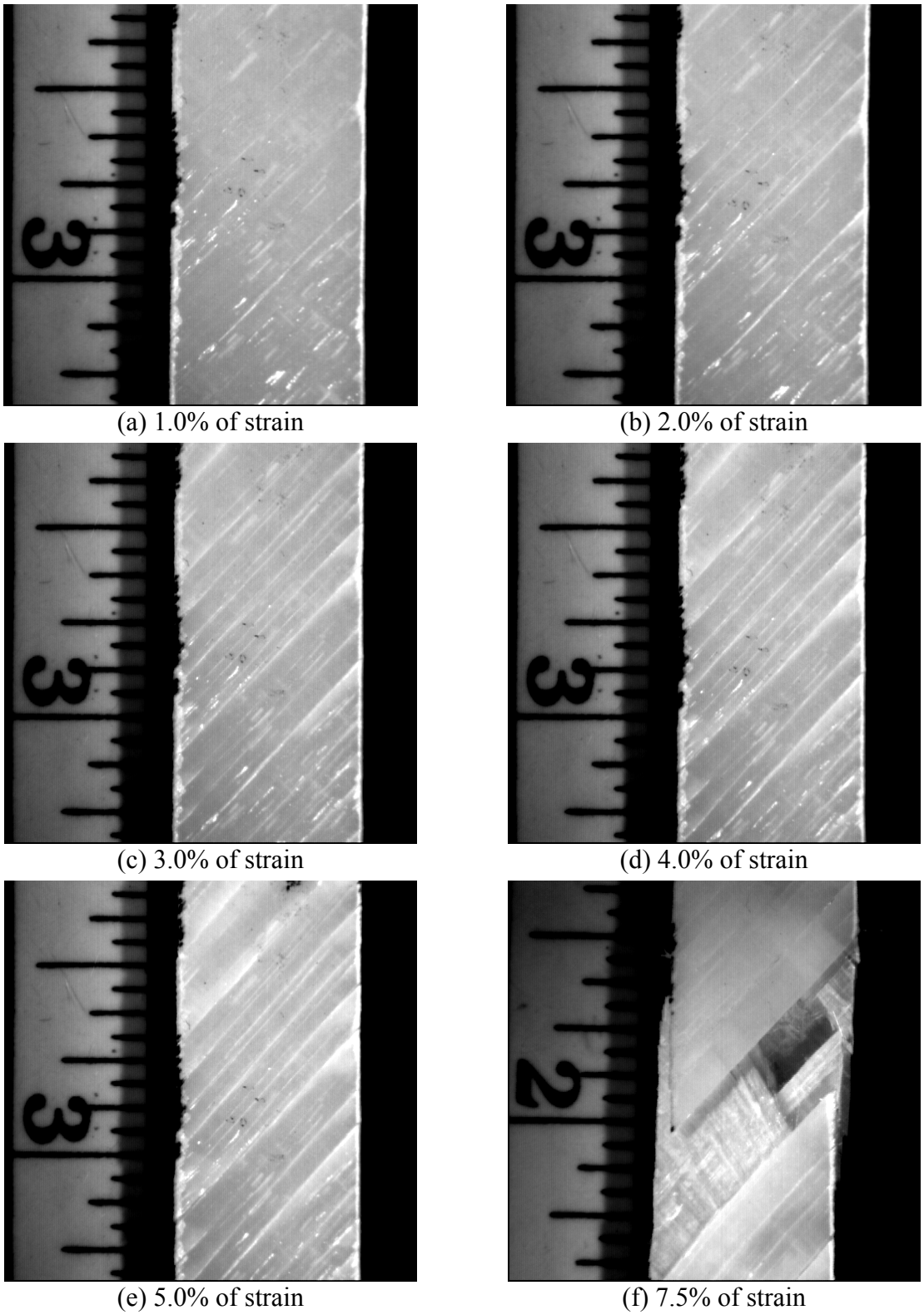

(a) 1.0% of strain (b) 2.0% of strain

(c) 3.0% of strain (d) 4.0% of strain

(e) 5.0% of strain (f) 7.5% of strain

Figure 4-1.7 Fractographs of an angle-ply $[+45°_3/-45°_3]_{2S}$ specimen taken during room-temperature tensile testing at different strain levels.

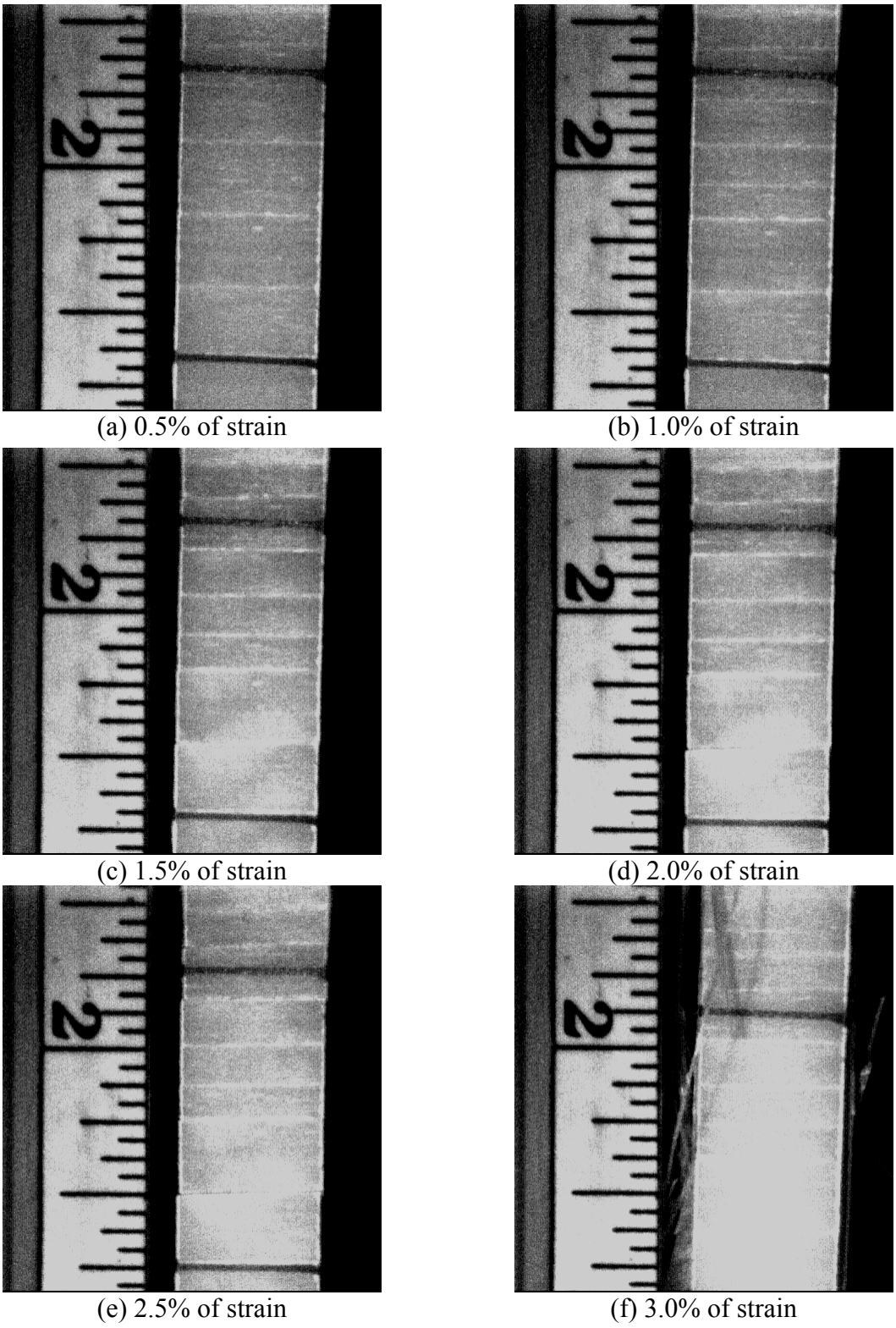

(a) 0.5% of strain (b) 1.0% of strain

(c) 1.5% of strain (d) 2.0% of strain

(e) 2.5% of strain (f) 3.0% of strain

Figure 4-1.8 Fractographs of a quasi-isotropic $[90°_3/+45°_3/0°_3/-45°_3]_S$ specimen taken during room-temperature tensile testing at different strain levels.

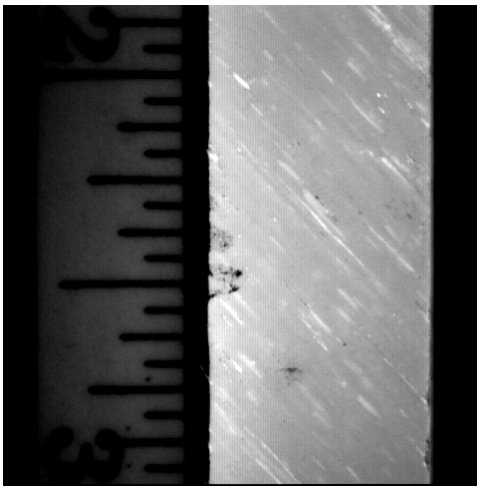

(a) 0.5% of strain

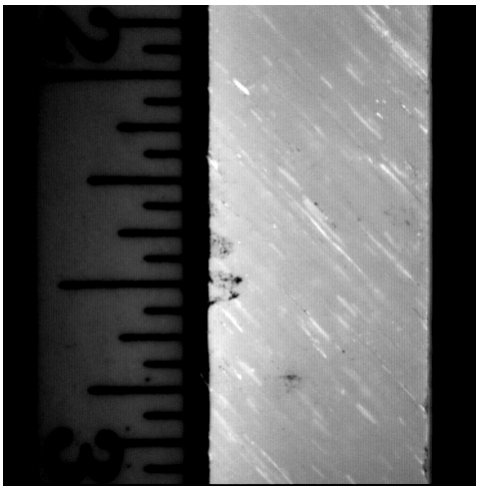

(b) 1.0% of strain

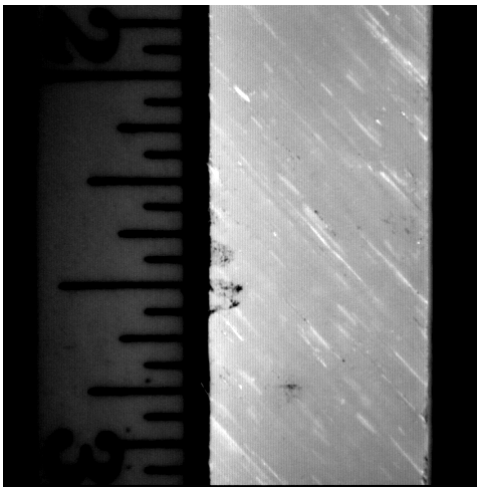

(c) 1.5% of strain

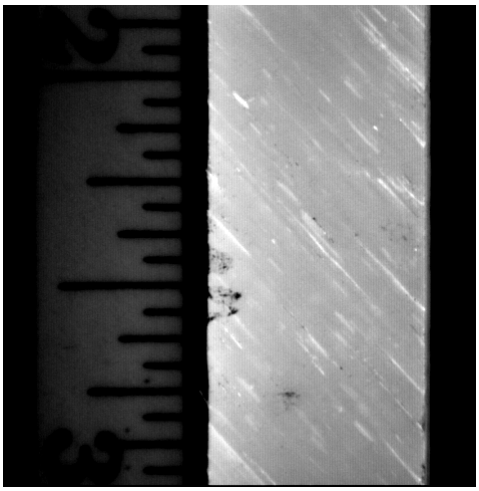

(d) 2.0% of strain

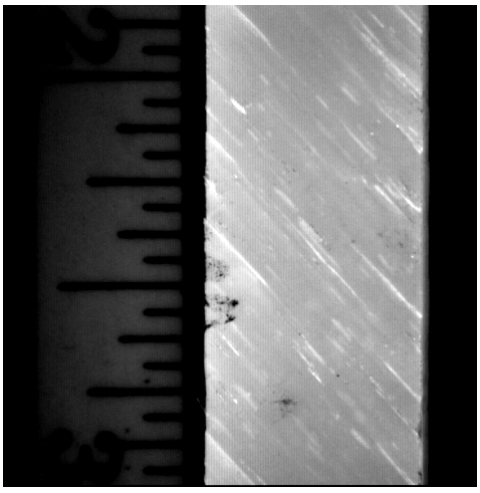

(e) 2.5% of strain

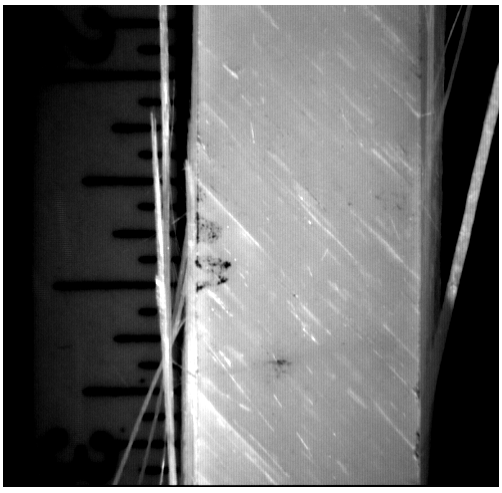

(f) 3.0% of strain

Figure 4-1.9 Fractographs of a quasi-isotropic $[+45°_3/90°_3/-45°_3/0°_3]_S$ specimen taken during room-temperature tensile testing at different strain levels.

In summary, the effect of lay-up configuration can be seen clearly in Figure 4-1.10(a), where the results for four different configurations are plotted together. As expected, since the fibers are much stronger than the matrix, the unidirectional $[0°]_{24\text{-ply}}$ specimens have the highest strength (950 MPa), which decreases significantly in order for the cross-ply $[0°_3/90°_3]_{2S}$, the quasi-isotropic $[0°_3/+45°_3/90°_3/–45°_3]_S$, and finally the angle-ply $[+45°_3/–45°_3]_{2S}$. Indeed, the ultimate strength (105MPa) of the angle-ply specimen is only 11% of that of the unidirectional specimen. By the same token, since the fibers are much stiffer than the matrix, the stiffness also decreases in the same order from the highest value for the $[0°]_{24\text{-ply}}$ to the lowest value for $[+45°_3/–45°_3]_{2S}$. On the other hand, the strains at failure decrease in the same order except for the $[+45°_3/–45°_3]_{2S}$ specimens where it increases significantly. This may be due to the large strain produced due to shear failure and delamination between the +45° and the –45° layers. Such a large strain at failure renders the damage behavior of the angle-ply composite to that of a ductile metal.

The same specimens were also tested at 75°C and 125°C using the environmental chamber of the MTS machine. The results are shown in Figures 4-1.11 and 4-1.12, respectively. At elevated temperatures the basic shape of the stress-strain curves did not change and the tensile damage behavior was similar. This conclusion can be obtained easily by examining Figures 4-1.10(a) to (c), which summarizes the results for four configurations at room temperature, 75°C and 125°C, respectively. To show the temperature effect for each lay-up configuration, its temperature-dependent stress-strain curves are plotted together as depicted in Figure 4-1.13, which indicates that the effect of higher temperature is reducing the strength and stiffness while increasing the strain at

failure in comparison with those at room temperature. For example the ultimate strength of the unidirectional $[0°]_{24\text{-ply}}$ specimens reduced from approximately 975 MPa at room-temperature to about 760 MPa at 125°C; a significant decrease of 22%. On the other hand, the strain at failure of the same unidirectional specimens increased from 7.5% at room temperature to 13% at 125°C, a profound increase of 73%.

Tensile experiments were also carried out at lower temperatures (–60°C and –20°C) for the cross-ply $[0°_3/90°_3]_{2S}$, angle-ply $[+45°_3/–45°_3]_{2S}$ and quasi-isotropic $[0°_3/45°_3/90°_3/–45°_3]_S$ specimens. Liquid nitrogen was supplied to the MTS-equipped environmental chamber to create the desire temperature. Whenever a specimen was placed in the chamber, condensation formed on the surfaces inside the chamber, particular around the hydraulic grips, when temperature was below the ice point. Thus slippage occurred and the unidirectional $[0°]_{24\text{-ply}}$ specimens never failed completely in low temperature tests. Figure 4-1.14 shows the effect of lower temperatures on three lay-up configurations. In general, the specimens behaved more stiff and brittle, especially on the linear portion of the stress-strain curves. This stiff and brittle behavior still occurred on the nonlinear portion of the stress-strain curves, where damage of the specimens became significant. However, for the cross-ply $[0°_3/90°_3]_{2S}$ specimens the trend was reversed. The $[0°_3/90°_3]_{2S}$ specimens tested at –60°C and –20°C were more "ductile" than those tested at room and high temperatures. This may be due to the undesirable slippage at the hydraulic grips when tested at low temperatures since the 0° layers of this type of specimens are very strong. Figure 4-1.13(d) also shows that the "ductile" behavior observed in the [±45°] specimens tested at room and high temperatures. This behavior was much subdued at low temperature.

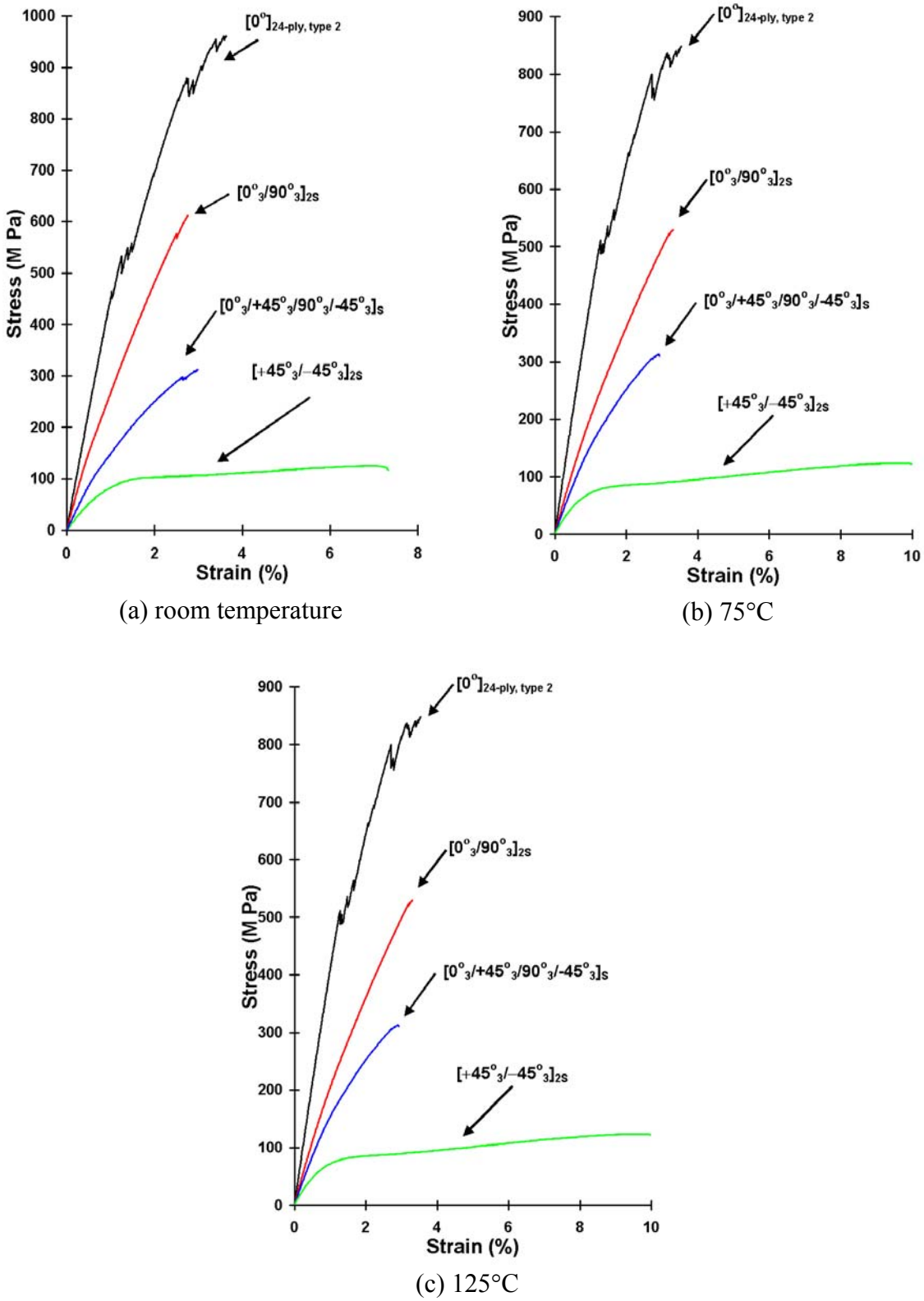

Figure 4-1.10 Comparison of tensile-damaged stress-strain curves at (a) room, (b) 75°C and (c) 125°C for various lay-up configurations.

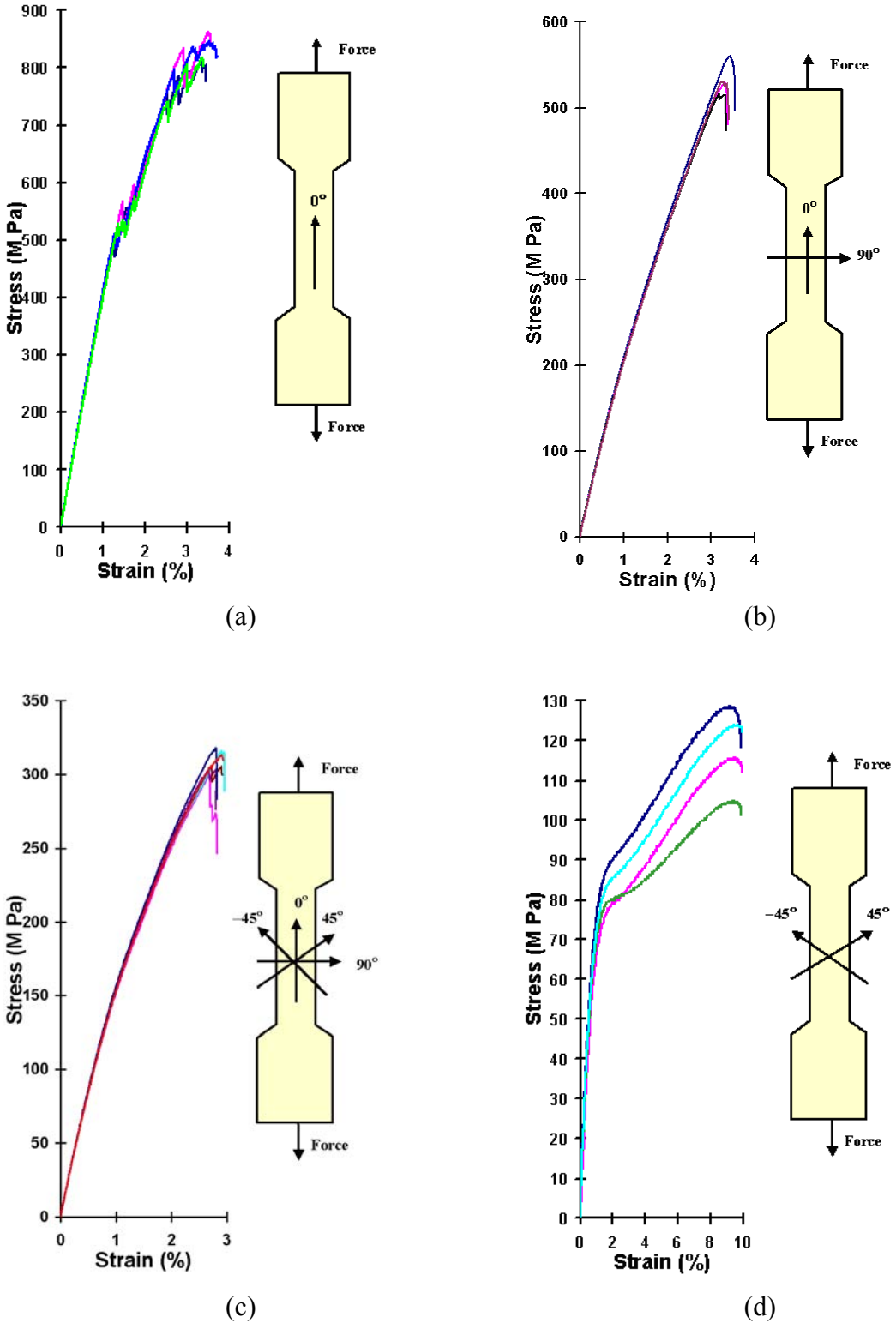

Figure 4-1.11 Tensile-induced damaged stress-strain curves for (a) unidirectional $[0°]_{24\text{-ply}}$, (b) cross-ply $[0°_3/90°_3]_{2S}$, (c) quasi-isotropic $[0°_3/+45°_3/90°_3/-45°_3]_S$ and (d) angle-ply $[+45°_3/-45°_3]_{2S}$ composites at 75°C.

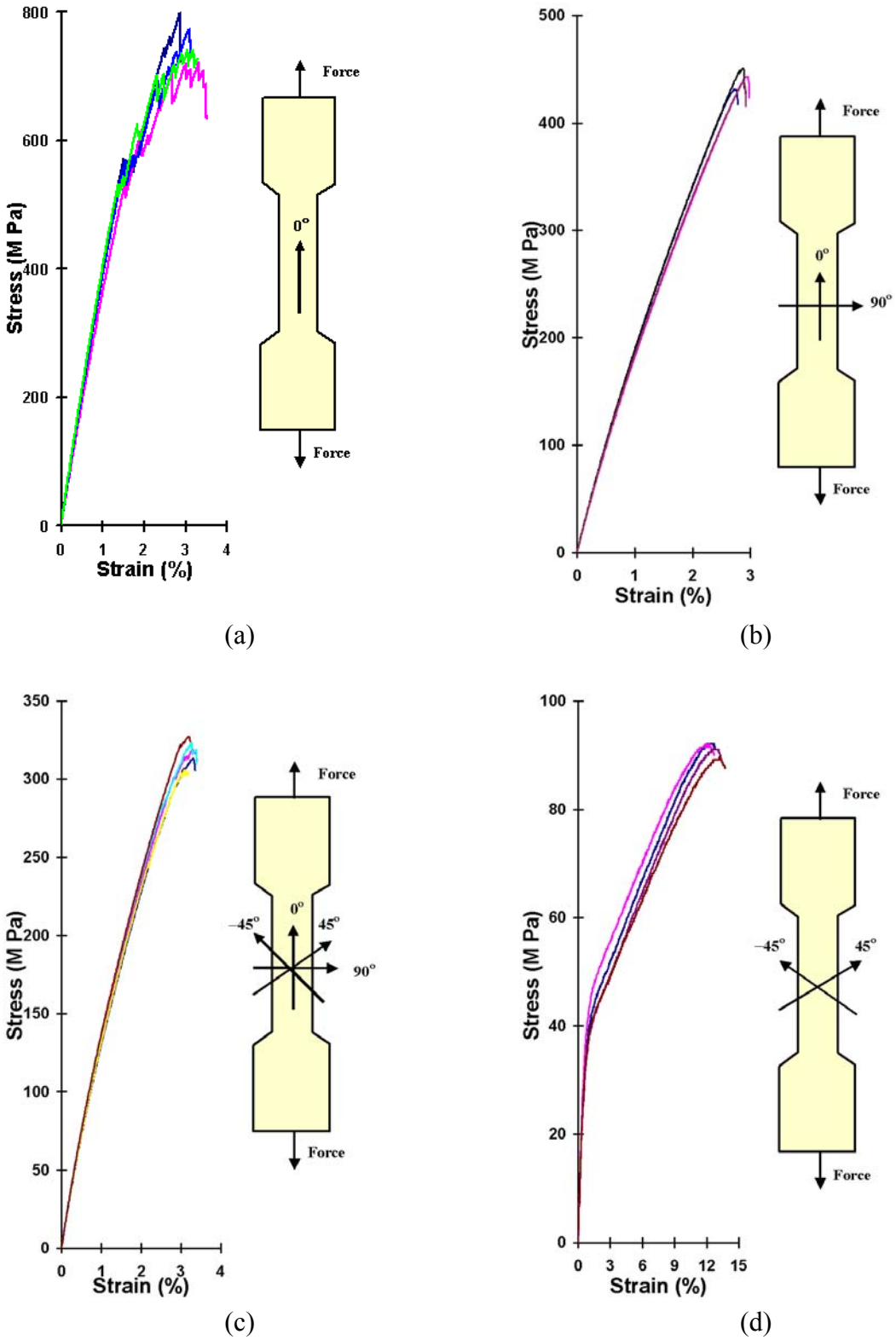

Figure 4-1.12 Tensile-induced damaged stress-strain curves for (a) unidirectional $[0°]_{24\text{-ply}}$, (b) cross-ply $[0°_3/90°_3]_{2S}$, (c) quasi-isotropic $[0°_3/+45°_3/90°_3/–45°_3]_S$ and (d) angle-ply $[+45°_3/–45°_3]_{2S}$ composites at 125°C.

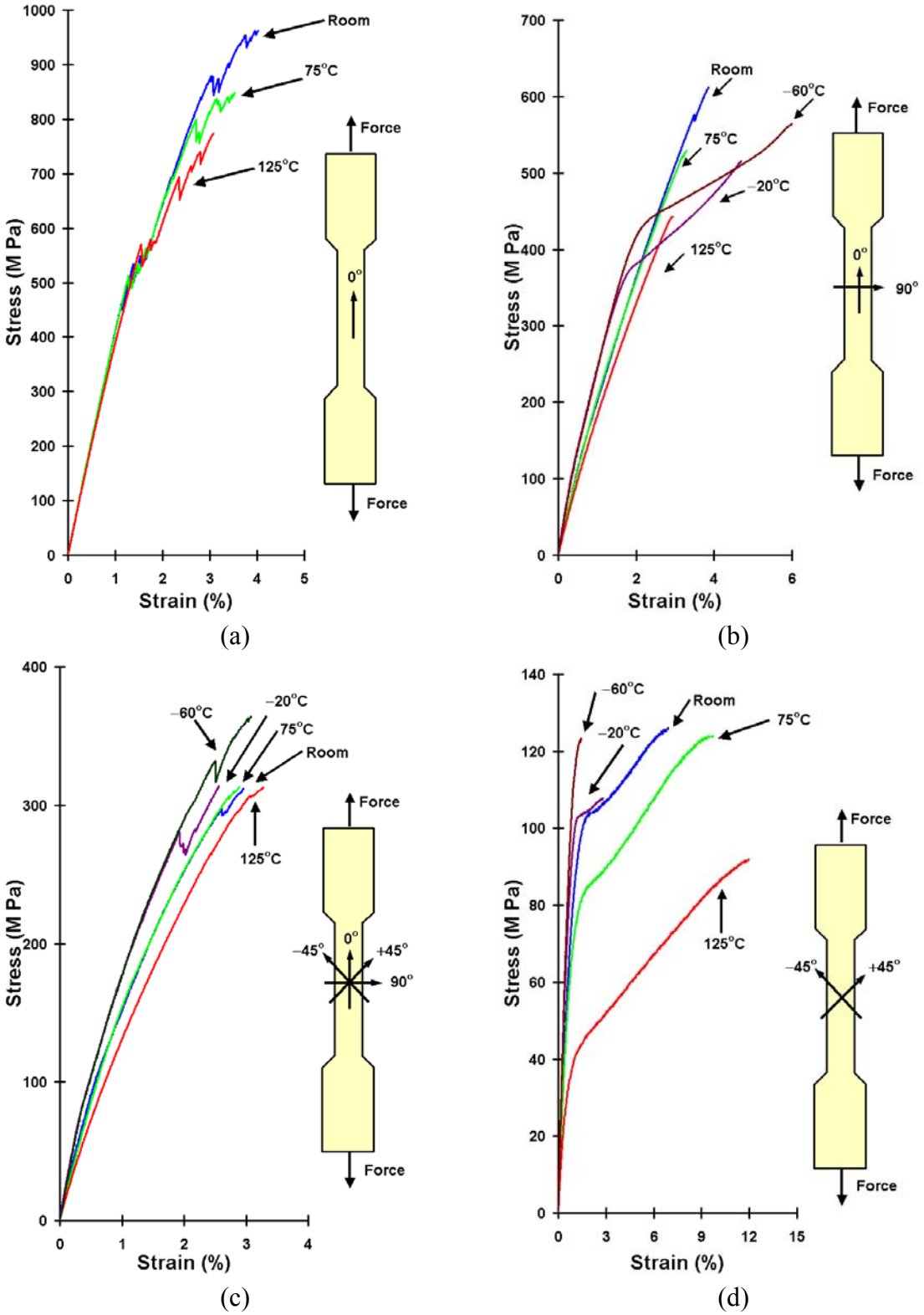

Figure 4-1.13 Temperature effect on the stress-strain curves of S2 glass/toughened epoxy composite specimens of (a) $[0°]_{24\text{-ply}}$, (b) $[0°_3/90°_3]_{2S}$, (c) $[0°_3/+45°_3/90°_3/-45°_3]_S$ and (d) $[+45°_3/-45°_3]_{2S}$ under uniaxial tension.

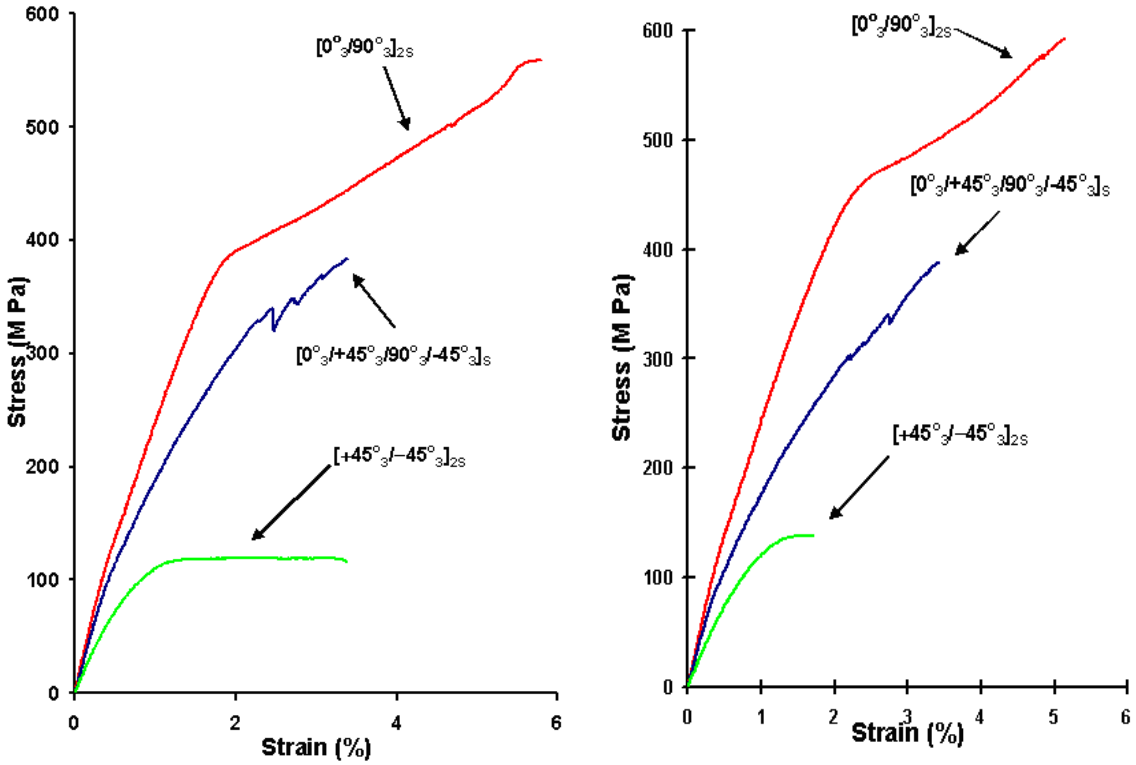

(a) –20°C (b) –60°C

Figure 4-1.14 Comparison of tensile-damaged stress-strain curves at (a) –20°C and (b) –60°C for various lay-up configurations.

4.2 Micromechanical Models for [0°] Specimens

As shown from the experimental results in Section 4.1, when a [0°] S2 glass fiber/toughened epoxy matrix composite was loaded by uniaxial tension, instead of the commonly encountered matrix cracking, fiber breakage occurred first then followed by fiber-matrix debonding. This is due to the extremely compliant nature of the toughened epoxy matrix. To account for this interesting effect, micromechanics-based unit-cell models based on mechanics of materials and the rule of mixtures were proposed to predict the failure progression of this type of specimens.

4.2.1 Micromechanics-based unit cells

In this section, unit-cell models, which take fiber-alignment pattern and fiber breakage into account, will be proposed. Two ideal fiber-alignment patterns are considered. The first is a square pattern, which assumes no dislocation in position between two adjacent lines of fibers, whereas the second is a hexagonal pattern, which possesses dislocation in position between two adjacent lines of fibers. As one may surmise, the behavior of a typical unidirectional composite with an irregularly packed fiber alignment, which occurs due to processing imperfection, may fall between the scopes of these two ideal patterns.

4.2.1.1 Square fiber-alignment: As shown in Figure 4-2.1, we first assumed the S2 glass fibers were aligned to form a square, where the notation F represents fibers, M the matrix, r the fiber radius, θ_1 the angle from the horizontal diameter of a fiber to its adjacent fiber, B the spacing between the outer surfaces of two neighboring fibers, and a the distance from center to center of two adjacent fibers.

The fiber volume fraction V_f is calculated as:

$$V_f = \frac{2\pi r^2}{a^2} \qquad 4\text{-}2.1$$

Rearrange the above equation, the distance a can be calculated:

$$a = \sqrt{\frac{2\pi r^2}{V_f}} \qquad 4\text{-}2.2$$

In this study, r = 5μm and V_f = 44% are given by the manufacture. Therefore the value of a from Equation 4-2.2 is 18.9μm.

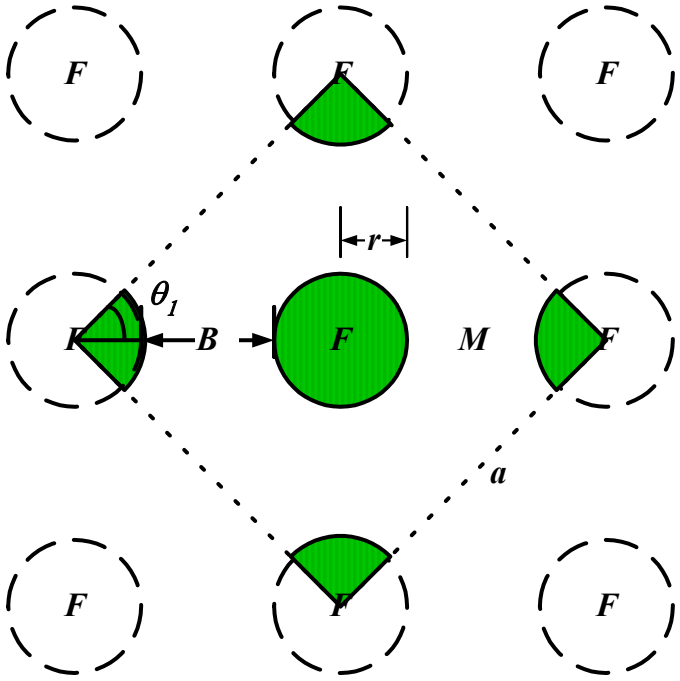

Figure 4-2.1 Square fiber alignment.

From Figure 4-2.1, the angle θ_1 can be assumed to be 45°. Therefore the distance between two fibers in the same plane can be easily calculated as:

$$B = \frac{a}{\sqrt{2}} - 2r \qquad 4\text{-}2.3$$

With a = 18.9μm, B becomes 3.36μm.

4.2.1.2 Hexagonal fiber-alignment: Figure 4-2.3 shows the S2 glass fibers are oriented to form a hexagon, where again the notation *F* represents fibers, *M* the matrix, *r* the fiber radius, θ_2 the angle from the horizontal diameter of a fiber to its adjacent fiber, *B* the spacing between the outer surfaces of two neighboring fibers, *a* the distance from center to center of two adjacent fibers, and *H* the vertical distance between two fibers.

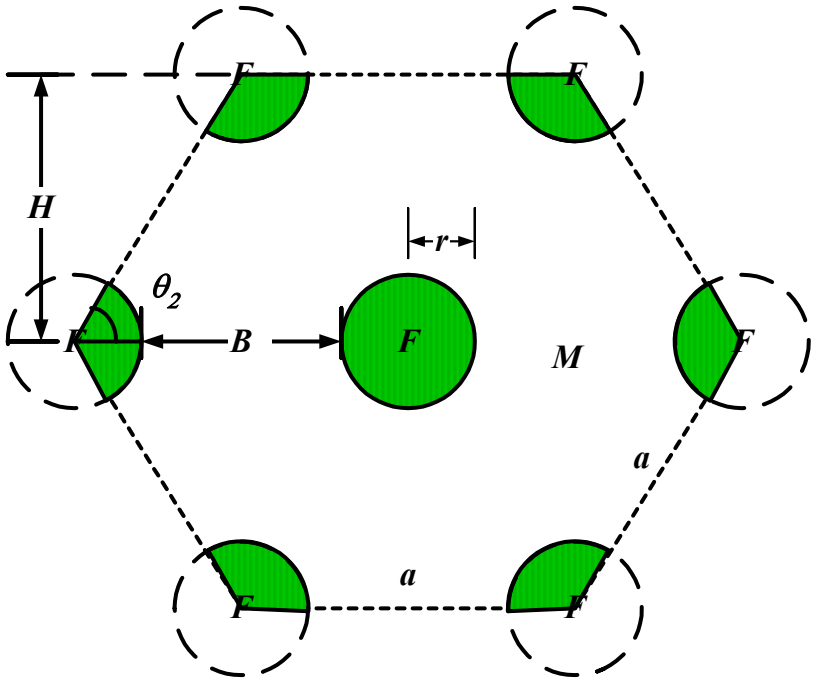

Figure 4-2.2 Hexagonal fiber orientation.

The fiber volume fraction V_f is calculated as:

$$V_f = \frac{\pi r^2}{Ha} \qquad 4\text{-}2.4$$

If the angle θ_2 is 60°, the relationship between *a* and *H* will be:

$$H = \frac{a\sqrt{3}}{2} \qquad 4\text{-}2.5$$

Substitute Equation 4-2.5 into Equation 4-2.4, we have:

$$a = \left(\frac{2\pi}{\sqrt{3}} \bullet \frac{r^2}{V_f} \right)^{\frac{1}{2}} \qquad 4\text{-}2.6$$

For r = 5μm and V_f = 44%, a is then calculated to be 14.4 μm. Therefore, H and B are 12.4μm and 4.36μm, respectively.

4.2.1.3 Fiber breakage: Now consider the case of fiber breakage without matrix cracking under constant strain. Figure 4-2.3 shows a block of unidirectional composite with its fibers forming a square fiber-alignment pattern. Assume that the left column of fibers, marked by double-shaded lines in Figure 4-2.3, had been broken at the top surface of the block while the matrix contained in that slice of composite remains intact. Hence, the parameter L, which represents fiber length of the unit cell, is the periodicity of fiber breakage along the fiber direction. Similar condition can also occur to the case of hexagonal fiber packing.

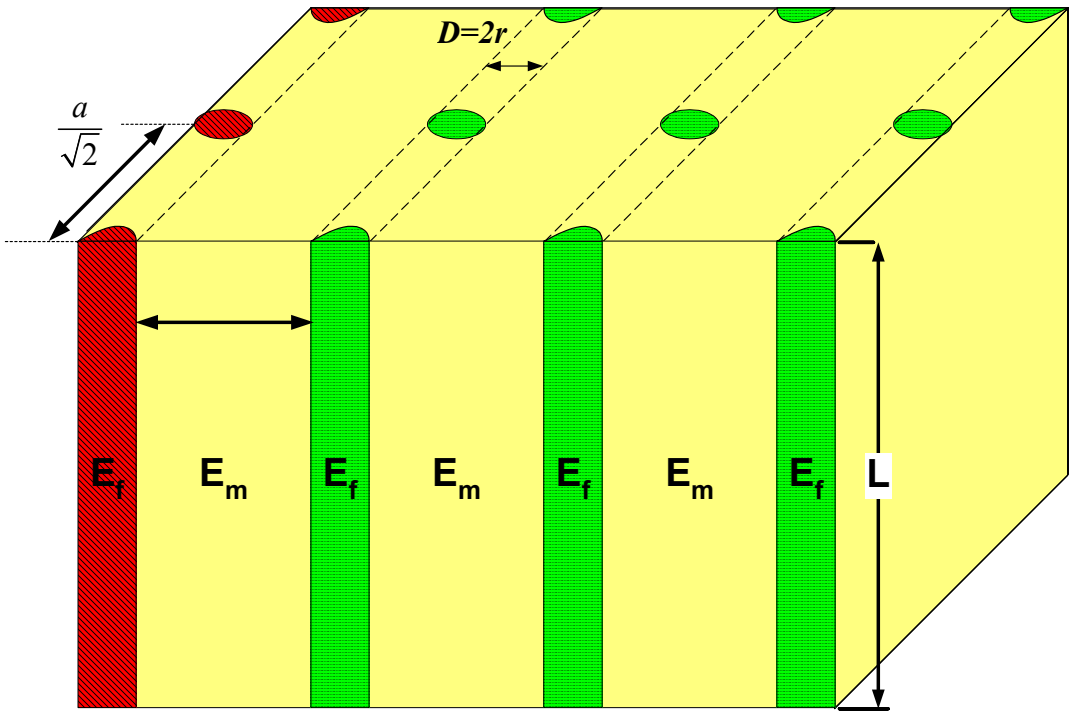

Figure 4-2.3 Broken fibers in a square pattern.

4.2.2 Micromechanical analyses

To further understanding the natural of micro-damage, one should look at the fiber packing of the specimens. Figure 4-2.4 shows the process of simulating (a) a random pattern of fiber packing by (b) a square pattern of fiber packing. When loaded along the fiber direction, we assume a column of fibers will break together at the same time, as illustrated in Figure 4-2.4(c). Similar scheme can be easily applied to the case of hexagonal fiber packing.

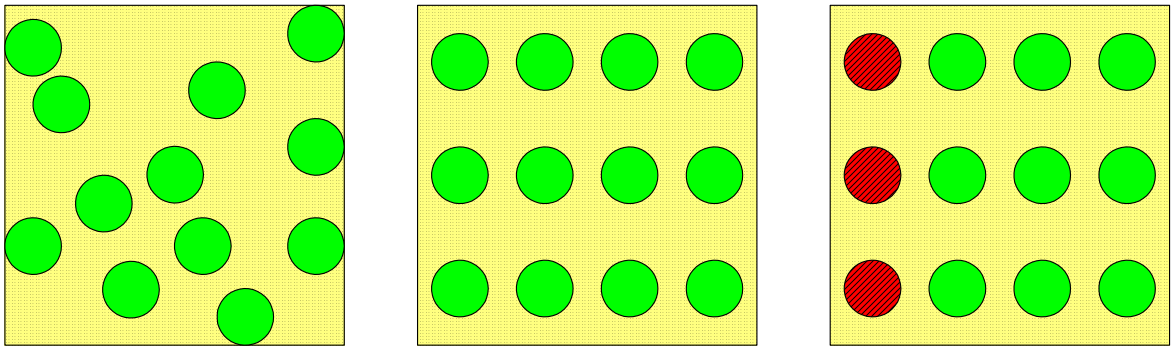

Figure 4-2.4 Typical fiber packing patterns: (a) random pack, (b) square pack with fibers intact, and (c) square pack with a column of broken fibers.

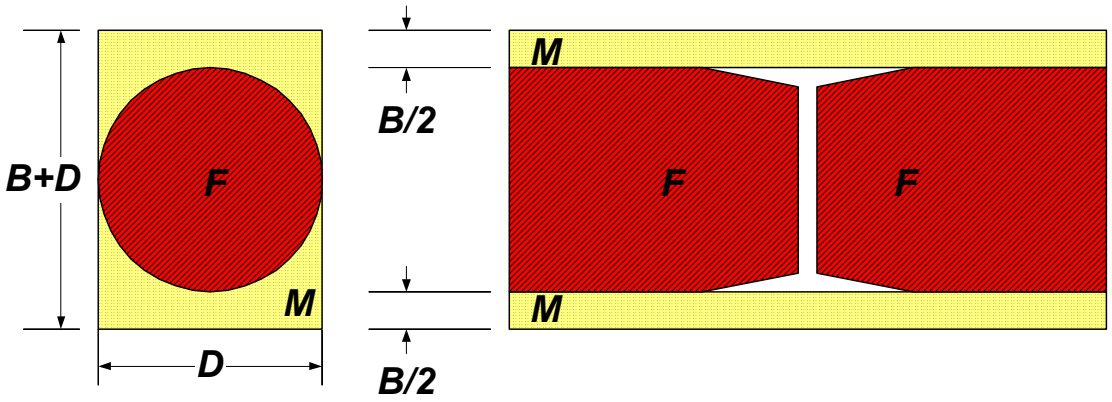

Figure 4-2.5 A basic cell for [0°] specimens, where B and D are the dimensions of the rectangular cell, F and M represent fiber and matrix, respectively.

Consider the basic cell of a $[0°]_{24\text{-ply}}$ specimen shown in Figure 4-2.5, where $D = 2r$ is the fiber diameter and B, as defined before, is the spacing between the outer surfaces

of two neighboring fibers. If neither the fiber nor the matrix is cracked, using the rule of mixtures, we can obtain the effective longitudinal moduli of this non-cracked basic cell as:

$$E_{\text{eff,N}} = V_{\text{eff,N}f} E_f + V_{\text{eff,N}m} E_m \qquad \text{4-2.7}$$

Here E_f and E_m are the Young's moduli of the fiber and the matrix, respectively; whereas $V_{\text{eff,N}f}$ and $V_{\text{eff,N}m}$ are the effective fiber and matrix volume fractions of the uncracked cell, respectively. It can be easily proven that:

$$V_{\text{eff,N}f} = \frac{\pi D}{4\left(B + D\right)} \qquad \text{4-2.8}$$

and

$$V_{\text{eff,N}m} = 1 - V_{\text{eff,N}m} \qquad \text{4-2.9}$$

On the other hand, if the fiber is broken while the matrix is not damaged, the effective longitudinal moduli of this cracked basic cell becomes:

$$E_{\text{eff,C}} = \alpha E_m \qquad \text{4-2.10}$$

where the dimensionless correctional factor α is:

$$\alpha = \frac{B + \left(1 - \frac{\pi}{4}\right) D}{B + D} \qquad \text{4-2.11}$$

The factor α is introduced to account for the fact that the matrix still attach in a cracked basic cell even though the fiber is already broken. For an S2 glass fiber used in this study, $D = 2r = 10\mu\text{m}$. For a square pattern, since $B = 3.36\mu\text{m}$ as derived above, therefore $V_{\text{eff,N}f}$ and α are equal to 58.8% and 0.41, respectively. In the case of fibers packed in a hexagonal shape, the values of B, $V_{\text{eff,N}f}$ and α are 4.36μm, 54.7% and 0.45, respectively.

Assume the fiber in the basic cell shown in Figure 4-2.5 is broken. If we insert the broken basic cell at the center of (k–2) unbroken basic cells to form a computational unit cell, as shown in Figure 4-2.6. Because of symmetry of this computational unit cell, the positive integer k must be odd and at least be 3. In the sequel, we will call such a computational unit as k-fiber model. Physically, it implies that 1 out of k fibers in the cell has been broken. In this study, we assume 8 different types of fiber breakage; namely, 17-, 15-, 13-, 11-, 9-, 7-, 5- and 3-fiber models, respectively.

The shaded and blank circles in Figure 4-2.6 correspond to the broken and unbroken fibers, respectively. The letters C, N and M denote the cracked area, non-cracked area, and the pure matrix area containing no fibers, respectively. In order to calculate the equivalent modulus of elasticity along fiber direction of a k-fiber model, the effective volume fractions of the cracked, the non-crack, and the pure matrix regions: $V_{\text{eff,C},k}$, $V_{\text{eff,N},k}$ and $V_{\text{eff,M}}$ need to be determined first. These parameters can be easily proven to be:

$$V_{\text{eff,C},k} = \frac{D}{k\left(B+D\right)}$$
$$V_{\text{eff,N},k} = \frac{\left(k-1\right)D}{k\left(B+D\right)} \qquad \text{4-2.12}$$
$$V_{\text{eff,M}} = \frac{B}{\left(B+D\right)}, \text{ for all models}$$

Note here that $V_{\text{eff,M}}$ does not depend on k, the number of fibers contained in the computational unit cell. Finally, for the k-fiber model, the effective modulus of elasticity along the fiber direction can now be obtained using the rule of mixtures:

$$E_{C,k} = V_{\text{eff,C},k}E_{\text{eff,C}} + V_{\text{eff,M}}E_m + V_{\text{eff,N},k}E_{\text{eff,N}} \qquad \text{4-2.13}$$

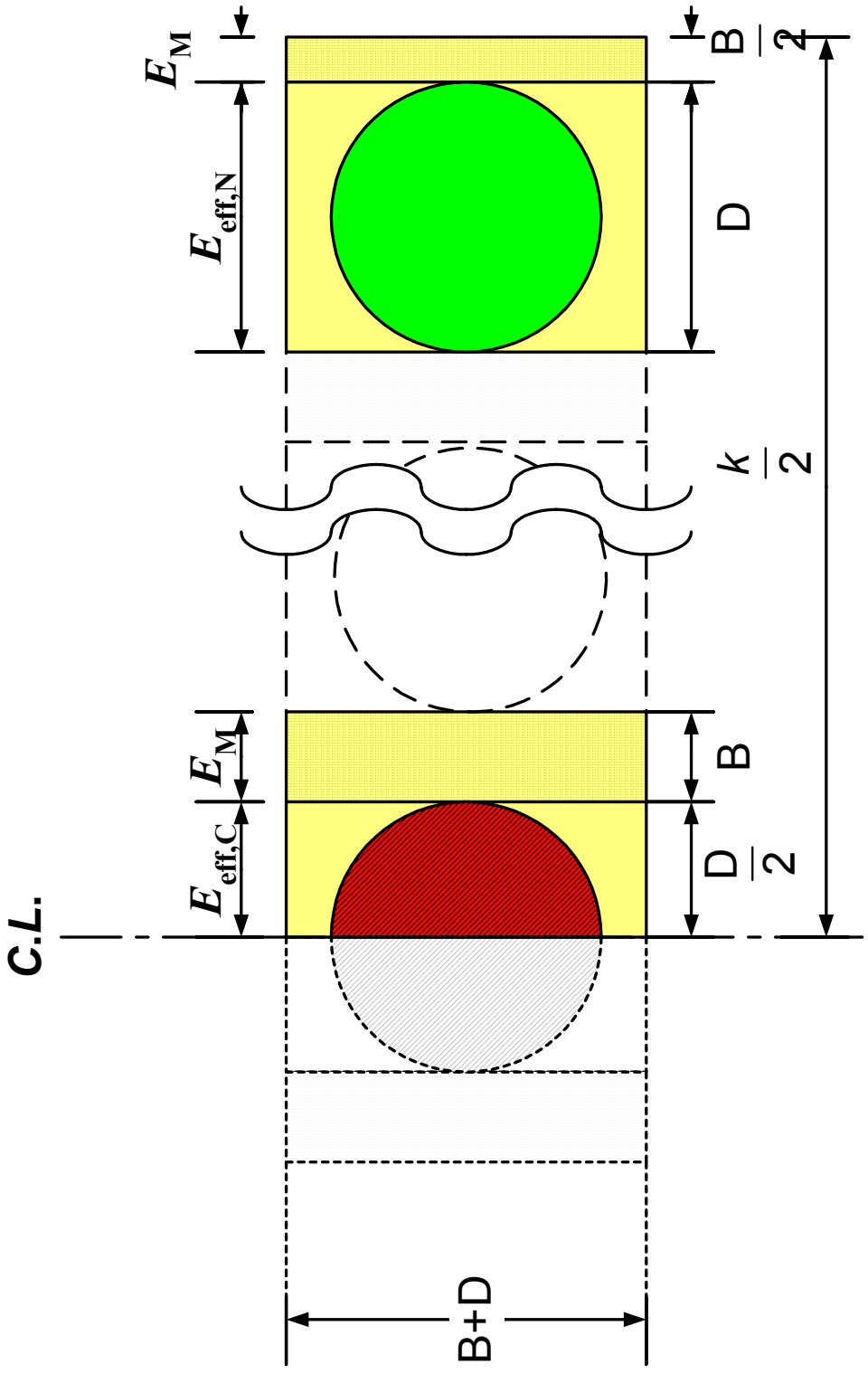

Figure 4-2.6 The computation half k-fiber unit cell.

In addition, we assume that the transverse modulus E_{Ct} remains the same and can be obtained through the rule of mixtures as:

$$E_{Ct} = \frac{E_f E_m}{V_m E_f + V_f E_m} \qquad 4\text{-}2.14$$

To construct the predicted stress-strain curve, the initial stress must be known. With the aid of *in situ* SEM testing (see Figure 4-1.4, *p*. 28), the initial strain to cause the first fiber to break was measured about 0.025%, which according to the rule of mixtures corresponded to an initial failure stress of about 10.7 MPa. The results show that for the [0^o] specimens, as the load increased, crack density, i.e., number of fiber breaks per unit area, also increased until it reached a saturated state. During this process fiber-matrix interfacial debonding also occurred. In the early stage of damage, only one in *k* fibers broke (see Figure 4-2). As the load was increased, more fibers were broken; first, say one in 17 fibers broke, called 17-fiber model (i.e., one out of 17 fibers in a unit cell was broken); which was followed by 15-, 13-, 11-, 9-, 7-, 5-, then finally 3-fiber model. It is not practical to use higher number for the fiber breakage, even though it was shown that one fiber broke in approximately 250 fibers during the early loading strain. There were almost no different when use higher number of fiber breakage. All these models were accompanied by fiber-matrix debonding, whose extension was governed by a constant interfacial fracture toughness, G_c (≈2,000 N/m), and an interfacial shear similar to Coulomb friction. In addition, as more fibers broke due to increasing strain, the effective modulus dropped as the result of broken fibers relaxed the stress of the specimen. This concept is similar to the classical statistics-based Chain-of-Bundles model (see Harlow *et al*. [80-82], Phoenix *et al*. [169]). This micromechanics model was incorporated into a

standard finite element software package, ANSYS, for calculating the required strain to advance fiber-matrix interfacial cracks. With Equation 4-2.13, the rule of mixtures and ANSYS results, all the effective moduli with different number of broken fibers were plotted for square and hexagonal arrays in Figures 4-2.7 and 4-2.8, respectively.

The predicted stress-strain curves high-lighted in these two figures were constructed by fitting the experimental results, as shown in Figure 4-2.9, which compares room-temperature stress-strain curves between theoretical predictions (square and hexagonal fiber alignments) and experimental data for unidirectional $[0°]_{24\text{-ply}}$ S2 glass fiber/toughened epoxy matrix composite under uniaxial tension. The linear portion of the curve was matched up to 0.025% strain using the rule of mixtures. For the square fiber alignment model, from the rule of mixtures slope to the 17-fiber modeling, stress was reduced due to fiber brakeage and the theoretical result matched the experimental data up to about 0.03% of the strain. Next the 15-fiber modeling covered the range of stain of 0.03% to 0.065%. It was followed by the 13-fiber modeling, where the strain range of 0.065% to 0.11% had been matched up well. The procedure was continued for the remaining models for a strain value up to 3%. Beyond that range, the proposed model was no longer valid since other failure modes (e.g., matrix cracking), which were not included in the proposed model, might have developed. The same procedure was applied to the hexagonal fiber alignment model and the simulated stress-strain curve is also shown in Figure 4-2.9.

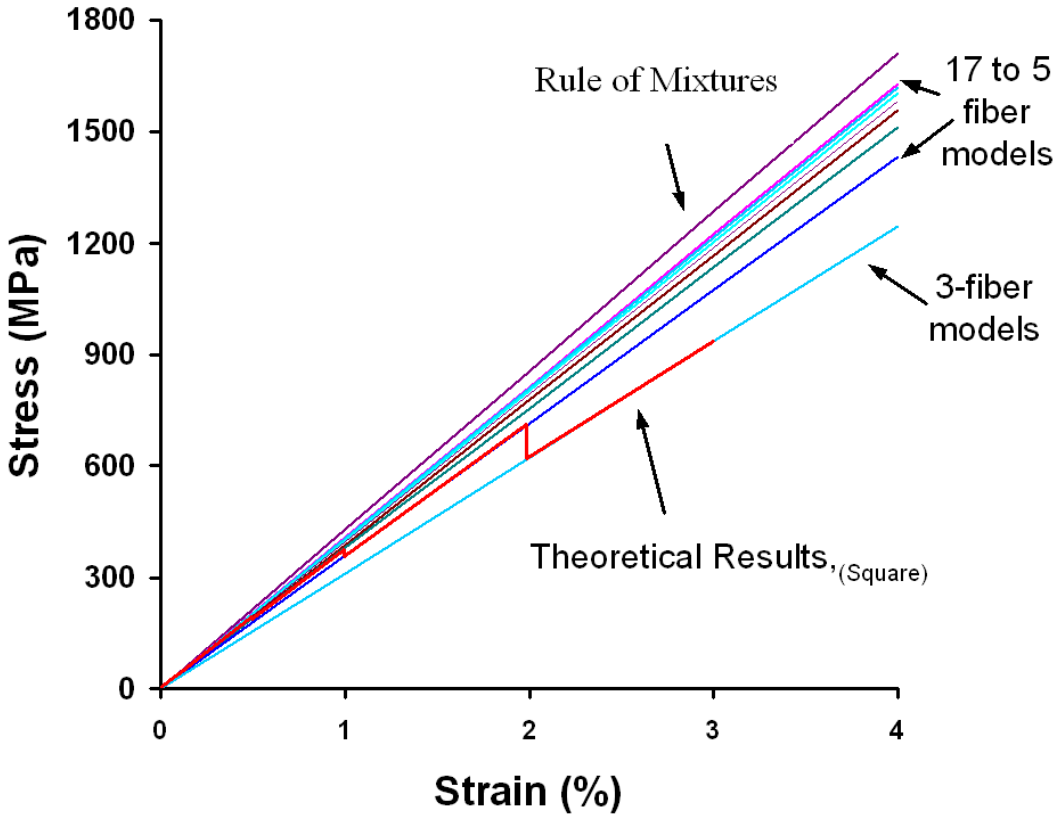

Figure 4-2.7 Determination of the theoretical prediction based on the square model for the stress-strain relation of a unidirectional $[0°]_{24\text{-ply}}$ composite tested under uniaxial tension at room-temperature.

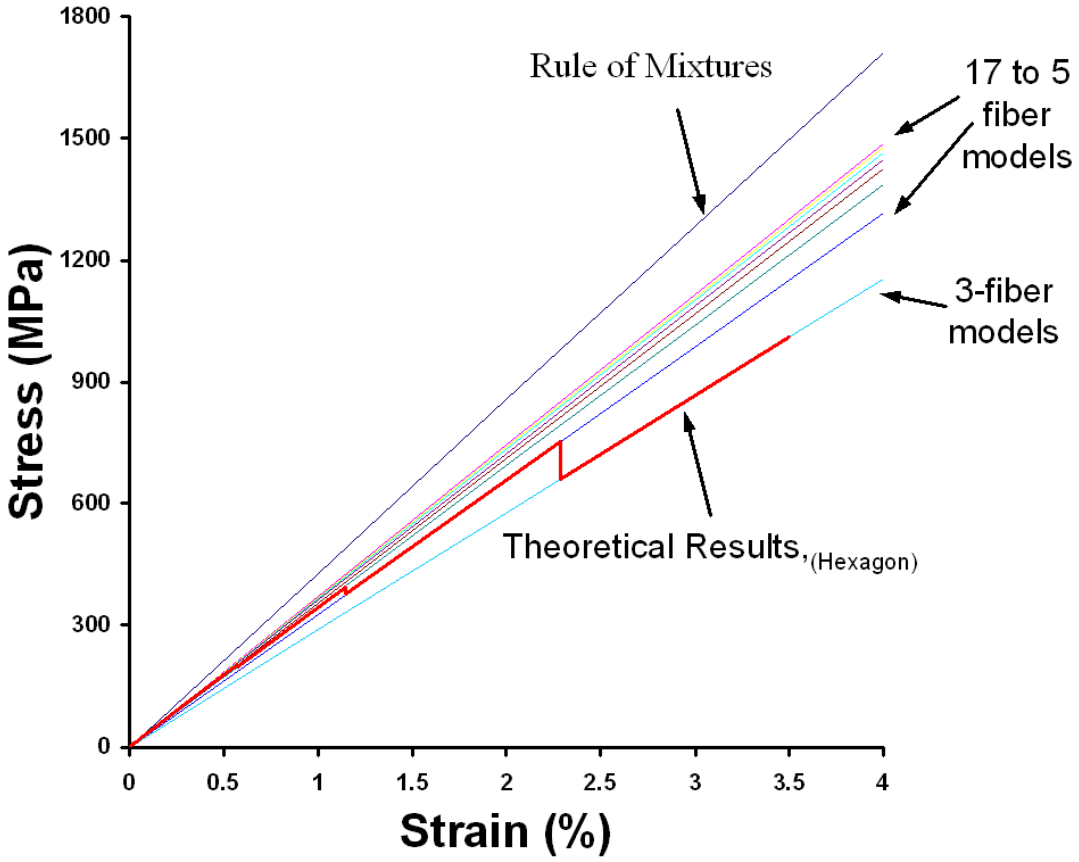

Figure 4-2.8 Determination of the theoretical prediction based on the hexagonal model for the stress-strain relation of a unidirectional $[0°]_{24\text{-ply}}$ composite tested under uniaxial tension at room-temperature.

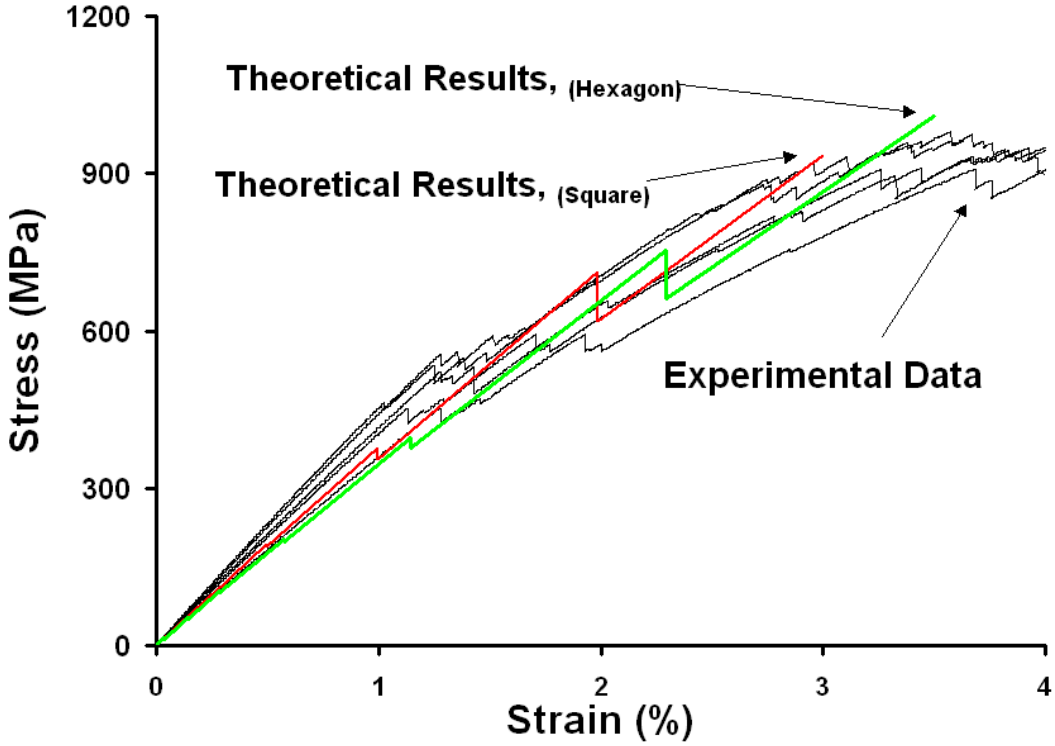

Figure 4-2.9 Comparison of room-temperature stress-strain curves between theoretical predictions and experimental data for unidirectional $[0°]_{24\text{-ply}}$ S2 glass fiber/toughened epoxy matrix composite under uniaxial tension.

4.3 Theoretical Models for Damaged Composite Laminates Under Uniaxial Tension

The following section explores the progressive failure of cross-ply, angle-ply and quasi-isotropic composite laminates under tensile loading. Although, as shown by experiment in Section 4.1, the damage modes for these configurations are not the same, the initial failure mode always starts with the "weakest" lamina, where damage occurs within the matrix (matrix cracking) or along the fiber-matrix interface (interfacing and shear cracking). For the cross-ply [0°/90°] specimens, the initial dominant failure mode is transverse cracking (in the form of matrix cracking or interfacing cracking) in the 90° layers. For the angle-ply [+45°/–45°] specimens, the initial dominant failure mode is shear cracking in one group of the 45°. Finally, the initial failure in the quasi-isotropic [0°/+45°/90°/–45°] specimens contains both transverse and shear crackings. To simulate these observations, theoretical models based on a scheme proposed by Daniel and his associates [51,52,138,196,197] were used to predict the progressive failure for those configurations in this study.

4.3.1 The $[0°_3/90°_3]_{2S}$ specimens

As recommended in Composite Materials Handbook-MIL 17 [2], the uniaxial tensile strength for $[0°_3/90°_3]_{2S}$ specimens can be determined using the equation:

$$F^{ut}_{[0°]} = CPF\left(F^{ut}_{[0°/90°]}\right) \qquad 4\text{-}3.1$$

where $F^{ut}_{[0°]}$ and $F^{ut}_{[0°/90°]}$ are the ultimate strengths for $[0°]_{24\text{-ply}}$ and $[0°_3/90°_3]_{2S}$ specimens, respectively. Here *CPF* is the cross-ply factor defined as:

$$CPF = \left[\frac{E_L \left(\frac{E_L + E_T}{2} \right) - \left(\nu_{LT} E_T \right)^2}{\left(\frac{E_L + E_T}{2} \right)^2 - \left(\nu_{LT} E_T \right)^2} \right] \qquad 4\text{-}3.2$$

where E_L and E_T are the longitudinal and transverse moduli of the lamina, respectively. ν_{LT} is the Poisson's ratio and assumed as 0.3. As reported in Section 4.1, E_L (from tensile tests of $[0°]_{24\text{-ply}}$ specimens) and E_T (from tensile tests of $[90°]_{24\text{-ply}}$ specimens) are 45 and 13 GPa, respectively. Therefore the crossply factor, CPF was calculated as 1.562. The room-temperature ultimate strength for the $[0°]_{24\text{-ply}}$ specimens, $F^{ut}_{[0°]}$, was 950 MPa as obtained from experiments. The room-temperature uniaxial tensile strength of the $[0°_3/90°_3]_{2S}$ specimens was then found to be 608 GPa, which agrees very well with the experimental finding (approximately 608 GPa).

When a $[0°_3/90°_3]_{2S}$ composite specimen under direct tension, since all [90°] layers fail much earlier than the [0°] layers, thus only the [0°] layers will carry the entire load. Intuitively, one may assume the ultimate strength of the $[0°_3/90°_3]_{2S}$ specimens is half of the ultimate strength of the $[0°]_{24\text{-ply}}$ specimens if the [0°] and [90°] layers have the same thickness. If so, the uniaxial strength of $[0°_3/90°_3]_{2S}$ specimens should have been 475 GPa instead of 608 GPa. The discrepancy may result from the remnant load-transfer capability of the broken 90° layers through interlaminar shear. Thus, even though a [90°] layer has failed, it still can strengthen the composite by providing shear tractions between its two neighboring [0°] layers. Such a load-carrying interlaminar shear transfer forms the basis of the theoretical model proposed by Daniel and his associates

[51,52,138,196,197], which was adopted in this study for predicting tensile-damaged stress-strain relations in layered composites.

Each group of $[0°_3]$ (or $[90°_3]$) layers in a $[0°_3/90°_3]_{2S}$ specimen investigated in this study was first treated as a [0°] (or a [90°]) layer with a triple thickness. The lay-up configuration of the 24-layer composite will become an 8-layer composite of the stacking sequence: [0°/90°/**0°/90°/90°/0°**/90°/0°]. The middle four layers, which are bold-faced, can be assumed as a unit cell and carries half of the load for the original 24-layer composite.

To obtain the stress-strain relation for the composite, consider a 4-layer $[0°/90°]_S$ cross-ply laminate with transverse cracks, as shown in Figure 4-3.1. Assume the displacement filed in this laminate is [196,197]:

$$\begin{aligned} u_1 &= a_1 z^2 + a_2 z + a_3 \\ v_1 &= a_4 z^2 + a_5 z + a_6 \\ u_2 &= a_7 z^2 + a_8 z + a_9 \\ v_2 &= a_{10} z^2 + a_{11} z + a_{12} \end{aligned} \qquad \text{4-3.3}$$

where u_1 and v_1 are the displacements in the x- and y-directions in Layer 1, respectively; u_2 and v_2 are the displacements in the x-and y-directions in Layer 2, respectively; a_i (i = 1 to 12) are constants and z is the thickness direction coordinate.

For the [0°] layers, the out-of-plane shear stresses are:

$$\begin{bmatrix} \tau_{1xz} \\ \tau_{1yz} \end{bmatrix} = \begin{bmatrix} S_{55} & S_{45} \\ S_{45} & S_{44} \end{bmatrix} \begin{bmatrix} \gamma_{1xz} \\ \gamma_{1yz} \end{bmatrix} \qquad \text{4-3.4}$$

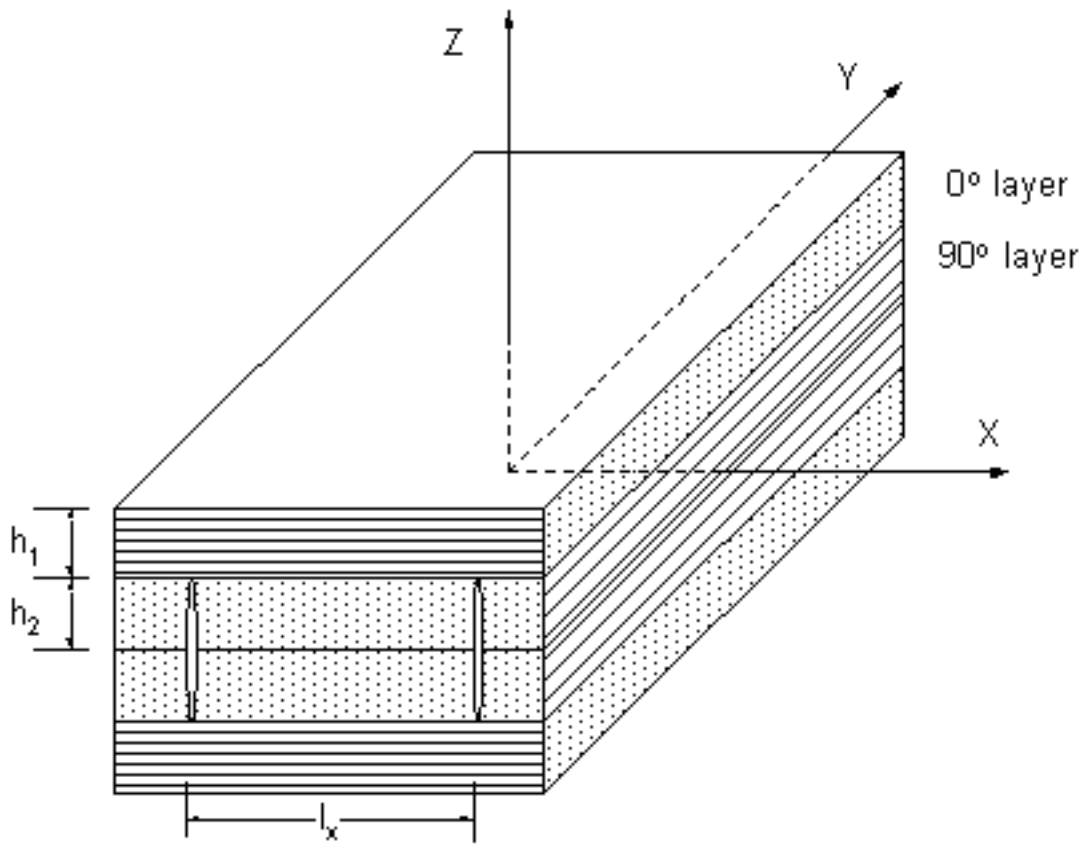

Figure 4-3.1 A four-layer cross-ply laminate with transverse cracks.

Since

$$\gamma_{1xz} = \frac{\partial u_1}{\partial z} = 2a_1 z + a_2$$
$$\gamma_{1yz} = \frac{\partial v_1}{\partial z} = 2a_4 z + a_5 \qquad 4\text{-}3.5$$

therefore

$$\begin{bmatrix} \tau_{1xz} \\ \tau_{1yz} \end{bmatrix} = \begin{bmatrix} S_{55} & S_{45} \\ S_{45} & S_{44} \end{bmatrix} \begin{bmatrix} 2a_1 z + a_2 \\ 2a_4 z + a_5 \end{bmatrix} \qquad 4\text{-}3.6$$

Similarly, for the [90°] layers, the out-of-plane shear stresses are:

$$\begin{bmatrix} \tau_{2xz} \\ \tau_{2yz} \end{bmatrix} = \begin{bmatrix} S'_{55} & S'_{45} \\ S'_{45} & S'_{44} \end{bmatrix} \begin{bmatrix} 2a_7 z + a_8 \\ 2a_{10} z + a_{11} \end{bmatrix} \qquad 4\text{-}3.7$$

In the above two equations,

$$
\begin{aligned}
S_{44} &= G_{13}\sin^2\phi + G_{23}\cos^2\phi \\
S_{45} &= \left(G_{23} - G_{13}\right)\cos\phi\sin\phi \\
S_{55} &= G_{13}\cos^2\phi + G_{23}\sin^2\phi \\
S'_{44} &= G_{13}\sin^2\theta + G_{23}\cos^2\theta \\
S'_{45} &= \left(G_{23} - G_{13}\right)\cos\theta\sin\theta \\
S'_{55} &= G_{13}\cos^2\theta + G_{23}\sin^2\theta
\end{aligned}
\qquad \text{4-3.8}
$$

At $z = h_1 + h_2$ (i.e., the top surface, see Figure 4-3.1), $\tau_{1xz} = \tau_{1yz} = 0$

$$
\left[0\right] = \begin{bmatrix} S_{55} & S_{45} \\ S_{45} & S_{44} \end{bmatrix} \begin{bmatrix} 2a_1\left(h_1 + h_2\right) + a_2 \\ 2a_4\left(h_1 + h_2\right) + a_5 \end{bmatrix} \qquad \text{4-3.9}
$$

where, h_1 and h_2 are the thicknesses of the 0° and 90° layers, respectively. Therefore

$$
\begin{bmatrix} a_2 \\ a_5 \end{bmatrix} = -2\left(h_1 + h_2\right) \begin{bmatrix} a_1 \\ a_5 \end{bmatrix} \qquad \text{4-3.10}
$$

At $z = 0$ (i.e., the mid-plane, see Figure 4-3.1), $\tau_{2xz} = \tau_{2yz} = 0$,

$$
\left[0\right] = \begin{bmatrix} S'_{55} & S'_{45} \\ S'_{45} & S'_{44} \end{bmatrix} \begin{bmatrix} a_8 \\ a_{11} \end{bmatrix} \qquad \text{4-3.11}
$$

Therefore

$$
\begin{bmatrix} a_8 \\ a_{11} \end{bmatrix} = \left[0\right] \qquad \text{4-3.12}
$$

At $z = h_2$ (i.e., the interlaminar face, see Figure 4-3.1), $\begin{bmatrix} \tau_{1xz} \\ \tau_{1yz} \end{bmatrix} = \begin{bmatrix} \tau_{ixz} \\ \tau_{iyz} \end{bmatrix}$, where τ_{ixz} and τ_{iyz} are the interlaminar-shear stresses

$$
\begin{bmatrix} \tau_{ixz} \\ \tau_{iyz} \end{bmatrix} = \begin{bmatrix} S_{55} & S_{45} \\ S_{45} & S_{44} \end{bmatrix} \begin{bmatrix} \left(2h_2 - 2h_1 - 2h_2\right)a_1 \\ \left(2h_2 - 2h_1 - 2h_2\right)a_4 \end{bmatrix} \qquad \text{4-3.13}
$$

Therefore

$$\begin{bmatrix} a_1 \\ a_4 \end{bmatrix} = -\frac{1}{2h_1}\begin{bmatrix} S_{55} & S_{45} \\ S_{45} & S_{44} \end{bmatrix}^{-1}\begin{bmatrix} \tau_{ixz} \\ \tau_{iyz} \end{bmatrix} \quad \text{4-3.14}$$

Similarly, at $z = h_2$, $\begin{bmatrix} \sigma_{2xz} \\ \sigma_{2yz} \end{bmatrix} = \begin{bmatrix} \sigma_{ixz} \\ \sigma_{iyz} \end{bmatrix}$

$$\begin{bmatrix} \sigma_{ixz} \\ \sigma_{iyz} \end{bmatrix} = 2h_2\begin{bmatrix} S'_{55} & S'_{45} \\ S'_{45} & S'_{44} \end{bmatrix}\begin{bmatrix} a_7 \\ a_{10} \end{bmatrix} \quad \text{4-3.15}$$

Therefore

$$\begin{bmatrix} a_7 \\ a_{10} \end{bmatrix} = \frac{1}{2h_2}\begin{bmatrix} S'_{55} & S'_{45} \\ S'_{45} & S'_{44} \end{bmatrix}^{-1}\begin{bmatrix} \sigma_{ixz} \\ \sigma_{iyz} \end{bmatrix} \quad \text{4-3.16}$$

Substitute a_i into the assumed displacement filed, Equation 4-3.3, the equations become:

$$\begin{bmatrix} u_1 \\ v_1 \end{bmatrix} = \left(\frac{z^2 - 2(h_1 + h_2)z}{-2h_1}\right)\begin{bmatrix} S_{55} & S_{45} \\ S_{45} & S_{44} \end{bmatrix}^{-1}\begin{bmatrix} \tau_{1xz} \\ \tau_{1yz} \end{bmatrix} + \begin{bmatrix} a_3 \\ a_6 \end{bmatrix} \quad \text{4-3.17}$$

$$\begin{bmatrix} u_2 \\ v_2 \end{bmatrix} = \left(\frac{z^2}{2h_2}\right)\begin{bmatrix} S'_{55} & S'_{45} \\ S'_{45} & S'_{44} \end{bmatrix}^{-1}\begin{bmatrix} \tau_{2xz} \\ \tau_{2yz} \end{bmatrix} + \begin{bmatrix} a_9 \\ a_{12} \end{bmatrix} \quad \text{4-3.18}$$

At $z = h_2$,

$$\begin{bmatrix} u_1 \\ v_1 \end{bmatrix} = \begin{bmatrix} u_2 \\ v_2 \end{bmatrix} \quad \text{4-3.19}$$

$$\begin{bmatrix} a_9 \\ a_{12} \end{bmatrix} - \begin{bmatrix} a_3 \\ a_6 \end{bmatrix} = \left(h_2 + \frac{h_2^2}{2h_1}\right)\begin{bmatrix} S_{55} & S_{45} \\ S_{45} & S_{44} \end{bmatrix}^{-1}\begin{bmatrix} \tau_{ixz} \\ \tau_{iyz} \end{bmatrix} - \left(\frac{h_2}{2}\right)\begin{bmatrix} S'_{55} & S'_{45} \\ S'_{45} & S'_{44} \end{bmatrix}^{-1}\begin{bmatrix} \tau_{ixz} \\ \tau_{iyz} \end{bmatrix} \quad \text{4-3.20}$$

Integrate Equations 4-3.17 and 4-3.18 with respected to *z,* the average in-plane displacements are developed for the two layers.

$$\begin{bmatrix} \overline{u}_i \\ \overline{v}_i \end{bmatrix} = \int \frac{1}{h_i}\begin{bmatrix} u_i \\ v_i \end{bmatrix} dz \quad \text{4-3.21}$$

Therefore

$$\begin{bmatrix}\bar{u}_1\\ \bar{v}_1\end{bmatrix}=\left(\frac{h_1}{3}+h_2+\frac{h_2^2}{2h_1}\right)\begin{bmatrix}S_{55} & S_{45}\\ S_{45} & S_{44}\end{bmatrix}^{-1}\begin{bmatrix}\tau_{ixz}\\ \tau_{iyz}\end{bmatrix}+\begin{bmatrix}a_3\\ a_6\end{bmatrix} \qquad 4\text{-}3.22$$

$$\begin{bmatrix}\bar{u}_2\\ \bar{v}_2\end{bmatrix}=\left(\frac{h_2}{6}\right)\begin{bmatrix}S'_{55} & S'_{45}\\ S'_{45} & S'_{44}\end{bmatrix}^{-1}\begin{bmatrix}\tau_{ixz}\\ \tau_{iyz}\end{bmatrix}+\begin{bmatrix}a_9\\ a_{12}\end{bmatrix} \qquad 4\text{-}3.23$$

Combine Equations 4-3.20, 4-3.22 and 4-3.23, the interlaminar shear stresses can be expressed as:

$$\begin{bmatrix}\sigma_{ixz}\\ \sigma_{iyz}\end{bmatrix}=-[H]\begin{bmatrix}\bar{u}_2-\bar{u}_1\\ \bar{v}_2-\bar{v}_1\end{bmatrix} \qquad 4\text{-}3.24$$

where

$$[H]=\left\{\left(\frac{h_1}{3}\right)\begin{bmatrix}S_{55} & S_{45}\\ S_{45} & S_{44}\end{bmatrix}^{-1}+\left(\frac{h_2}{3}\right)\begin{bmatrix}S'_{55} & S'_{45}\\ S'_{45} & S'_{44}\end{bmatrix}^{-1}\right\}^{-1} \qquad 4\text{-}3.25$$

is known as the interlaminar-shear-stress stiffness matrix, which can be proved to be:

$$[H]=\begin{bmatrix}H_{11} & 0\\ 0 & H_{22}\end{bmatrix} \qquad 4\text{-}3.26$$

where

$$H_{11}=\frac{3G_{13}G_{23}}{h_2G_{13}+h_1G_{23}}$$

$$H_{22}=\frac{3G_{13}G_{23}}{h_1G_{13}+h_2G_{23}} \qquad 4\text{-}3.27$$

As shown in Figure 4-3.2, the equilibrium conditions of the free-body diagrams of the layers are:

$$\begin{bmatrix}\frac{\partial N_{2x}}{\partial x}+\frac{\partial N_{2xy}}{\partial y}\\ \frac{\partial N_{2xy}}{\partial x}+\frac{\partial N_{2y}}{\partial y}\end{bmatrix}=-\begin{bmatrix}\tau_{ixy}\\ \tau_{iyz}\end{bmatrix}=-\begin{bmatrix}\frac{\partial N_{1x}}{\partial x}+\frac{\partial N_{1xy}}{\partial y}\\ \frac{\partial N_{1xy}}{\partial x}+\frac{\partial N_{1y}}{\partial y}\end{bmatrix} \qquad 4\text{-}3.28$$

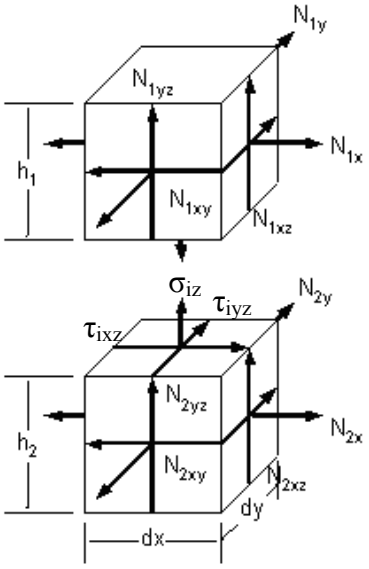

Figure 4-3.2 Free-body diagrams for [0°] and [90°] layers.

From the stress-strain relations:

$$[\sigma]=[Q][\varepsilon]+[\sigma]^R \tag{4-3.29}$$

We can obtained the force-displacement relations for the two layers as:

$$\begin{aligned} N_{1x} &= \left(Q_{11}\frac{\partial \overline{u}_1}{\partial x} + Q_{12}\frac{\partial \overline{v}_1}{\partial y} + \sigma_{1x}^R \right) h_1 \\ N_{1y} &= \left(Q_{12}\frac{\partial \overline{u}_1}{\partial x} + Q_{22}\frac{\partial \overline{v}_1}{\partial y} + \sigma_{1y}^R \right) h_1 \\ N_{1xy} &= Q_{66}\left(\frac{\partial \overline{u}_1}{\partial y} + \frac{\partial \overline{v}_1}{\partial x} \right) h_1 \end{aligned} \tag{4-3.30}$$

$$\begin{aligned} N_{2x} &= \left(Q'_{22}\frac{\partial \overline{u}_2}{\partial x} + Q'_{12}\frac{\partial \overline{v}_2}{\partial y} + \sigma_{2x}^R \right) h_2 \\ N_{2y} &= \left(Q'_{12}\frac{\partial \overline{u}_2}{\partial x} + Q'_{11}\frac{\partial \overline{v}_2}{\partial y} + \sigma_{2y}^R \right) h_2 \\ N_{2xy} &= Q'_{66}\left(\frac{\partial \overline{u}_2}{\partial y} + \frac{\partial \overline{v}_2}{\partial x} \right) h_2 \end{aligned} \tag{4-3.31}$$

where, $\sigma_{1x}^R, \sigma_{1y}^R, \sigma_{2x}^R$ and σ_{2y}^R are residual stresses in 0° and 90° layers. They satisfy the self-equilibrium conditions

$$\sigma_{1x}^{R} h_1 + \sigma_{2x}^{R} h_2 = 0$$
$$\sigma_{1y}^{R} h_1 + \sigma_{2y}^{R} h_2 = 0 \qquad \text{4-3.32}$$

Substituting N_i into equilibrium conditions of the free-body diagrams, the governing equations are developed as:

$$Q'_{22}\frac{\partial^2 \overline{u}_2}{\partial x^2} + Q'_{12}\frac{\partial^2 \overline{v}_2}{\partial x \partial y} + Q'_{66}\left(\frac{\partial^2 \overline{u}_2}{\partial y^2} + \frac{\partial^2 \overline{v}_2}{\partial x \partial y}\right) = \frac{H_{11}}{h_2}\left(\overline{u}_2 - \overline{u}_1\right)$$

$$Q_{11}\frac{\partial^2 \overline{u}_1}{\partial x^2} + Q_{12}\frac{\partial^2 \overline{v}_1}{\partial x \partial y} + Q_{66}\left(\frac{\partial^2 \overline{u}_1}{\partial y^2} + \frac{\partial^2 \overline{v}_1}{\partial x \partial y}\right) = \frac{H_{11}}{h_1}\left(\overline{u}_1 - \overline{u}_2\right) \qquad \text{4-3.33}$$

$$Q'_{11}\frac{\partial^2 \overline{v}_1}{\partial y^2} + Q'_{12}\frac{\partial^2 \overline{u}_2}{\partial x \partial y} + Q'_{66}\left(\frac{\partial^2 \overline{u}_2}{\partial x \partial y} + \frac{\partial^2 \overline{v}_2}{\partial x^2}\right) = \frac{H_{22}}{h_2}\left(\overline{v}_2 - \overline{v}_1\right)$$

$$Q_{22}\frac{\partial^2 \overline{v}_1}{\partial y^2} + Q_{12}\frac{\partial^2 \overline{u}_1}{\partial x \partial y} + Q_{66}\left(\frac{\partial^2 \overline{u}_1}{\partial x \partial y} + \frac{\partial^2 \overline{v}_1}{\partial x^2}\right) = \frac{H_{22}}{h_1}\left(\overline{v}_1 - \overline{v}_2\right)$$

These governing equations can be written as the initial notations form for [0°] and [90°] layers,

$$Q_{22}\overline{u}_{2,xx} + Q_{12}\overline{v}_{2,xy} + Q_{66}\left(\overline{u}_{2,yy} + \overline{v}_{2,xy}\right) = \frac{H_{11}}{h_2}\left(\overline{u}_2 - \overline{u}_1\right)$$
$$Q_{11}\overline{u}_{1,xx} + Q_{12}\overline{v}_{1,xy} + Q_{66}\left(\overline{u}_{1,yy} + \overline{v}_{1,xy}\right) = \frac{H_{11}}{h_1}\left(\overline{u}_1 - \overline{u}_2\right)$$
$$Q_{11}\overline{v}_{1,yy} + Q_{12}\overline{u}_{2,xy} + Q_{66}\left(\overline{u}_{2,xy} + \overline{v}_{2,xx}\right) = \frac{H_{22}}{h2}\left(\overline{v}_2 - \overline{v}_1\right) \qquad \text{4-3.34}$$
$$Q_{22}\overline{v}_{1,yy} + Q_{12}\overline{u}_{1,xy} + Q_{66}\left(\overline{u}_{1,xy} + \overline{v}_{1,xx}\right) = \frac{H_{22}}{h_1}\left(\overline{v}_1 - \overline{v}_2\right)$$

where Q_{11}, Q_{12}, Q_{22} and Q_{66} are stiffness parameters of the basic lamina, and $\overline{u}_1$, $\overline{v}_1$, $\overline{u}_2$ and $\overline{v}_2$ are the displacement of the 0° and 90° layers in the *x*- and *y*-directions, respectively.

Now assume the new displacement field as [196,197]:

$$\begin{aligned}\bar{u}_1 &= C_1 x + C_2 y + C_5 \sinh(\alpha_1 x)\\ \bar{u}_2 &= C_1 x + C_2 y + C_6 \sinh(\alpha_1 x)\\ \bar{v}_1 &= C_3 x + C_4 y + C_7 \sinh(\alpha_2 x)\\ \bar{v}_2 &= C_3 x + C_4 y + C_8 \sinh(\alpha_2 x)\end{aligned} \qquad \text{4-3.35}$$

and the non-zero terms are:

$$\begin{aligned}\bar{u}_{1,xx} &= \alpha_1^2 C_5 \sinh(\alpha_1 x)\\ \bar{u}_{2,xx} &= \alpha_1^2 C_6 \sinh(\alpha_1 x)\\ \bar{v}_{1,xx} &= \alpha_2^2 C_7 \sinh(\alpha_2 x)\\ \bar{v}_{2,xx} &= \alpha_2^2 C_8 \sinh(\alpha_2 x)\end{aligned} \qquad \text{4-3.36}$$

Substitute Equations 4-3.35 and 4-3.36 into Equation 4-3.34, we obtain:

$$\begin{cases} Q_{22}\left[\alpha_1^2 C_6 \sinh(\alpha_1 x)\right] = \dfrac{H_{11}}{h_2}(C_6 - C_5)\sinh(\alpha_1 x) \\ Q_{22}\alpha_1^2 C_6 = \dfrac{H_{11}}{h_2}(C_6 - C_5) \end{cases} \qquad \text{4-3.37}$$

$$\begin{cases} Q_{11}\left[\alpha_1^2 C_5 \sinh(\alpha_1 x)\right] = \dfrac{H_{11}}{h_1}(C_5 - C_6)\sinh(\alpha_1 x) \\ Q_{11}\alpha_1^2 C_5 = \dfrac{H_{11}}{h_2}(C_5 - C_6) \end{cases} \qquad \text{4-3.38}$$

From Equations 4-3.37 and 4-3.38, we can solve for C_5 and C_6;

$$\frac{C_5}{C_6} = -\frac{Q_{22}h_2}{Q_{11}h_1} \qquad \text{4-3.39}$$

Similarly,

$$\begin{cases} Q_{66}\left[\alpha_2^2 C_7 \sinh(\alpha_2 x)\right] = \dfrac{H_{22}}{h_1}(C_7 - C_8)\sinh(\alpha_2 x) \\ Q_{66}\alpha_2^2 C_7 = \dfrac{H_{22}}{h_1}(C_7 - C_8) \end{cases} \qquad \text{4-3.40}$$

$$\begin{cases} Q_{66}\left[\alpha_2^2 C_8 \sinh(\alpha_2 x)\right] = \dfrac{H_{22}}{h_2}(C_8 - C_7)\sinh(\alpha_2 x) \\ Q_{66}\alpha_2^2 C_8 = \dfrac{H_{22}}{h_2}(C_8 - C_7) \end{cases} \qquad 4\text{-}3.41$$

Again from the above two equations, C_7 and C_8 can be related as:

$$\frac{C_7}{C_8} = -\frac{h_2}{h_1} \qquad 4\text{-}3.42$$

To obtain α_1, use Equations 4-3.37, 4-3.38 and 4-3.39:

$$Q_{22}\alpha_1^2 C_6 - Q_{11}\alpha_1^2 C_5 = \frac{H_{11}}{h_2}(C_6 - C_5) - \frac{H_{11}}{h_1}(C_5 - C_6)$$

α_1 can be found to be:

$$\alpha_1^2 = H_{11}\left(\frac{1}{h_1 Q_{11}} + \frac{1}{h_2 Q_{22}}\right) \qquad 4\text{-}3.43$$

Similarly, use Equations 4-3.40, 4-3.41 and 4-3.42 to obtain α_2

$$\alpha_2^2 = \frac{H_{22}}{Q_{66}}\left(\frac{1}{h_1} + \frac{1}{h_2}\right) \qquad 4\text{-}3.44$$

Using the boundary conditions, $\bar{u}_1 = \bar{u}_2 = 0$ at $x = 0$, we have

$C_2 = 0$

when $x = \dfrac{l_x}{2}$, $\bar{u}_1 = \bar{u}^o$, where $\bar{u}^o$ is a contant and l_x is the crack spacing.

Defining $\dfrac{\bar{u}^o}{l_x/2} = \bar{\varepsilon}_x$, $\quad \therefore\ \bar{\varepsilon}_x = \dfrac{2\bar{u}^o}{l_x}$, where $\bar{\varepsilon}_x$ is the average strain in the x-direction.

$$\bar{u}_1 = \bar{u}^o = C_1\left(\frac{l_x}{2}\right) + C_5 \sinh\left(\alpha_1 \frac{l_x}{2}\right)$$

$$C_1 = \frac{\bar{u}^o}{l_x/2} - \frac{2C_5}{l_x}\sinh\left(\alpha_1 \frac{l_x}{2}\right) \qquad 4\text{-}3.45$$

but $\bar{\varepsilon}_x = \dfrac{\bar{u}^o}{l_x/2}$

$$C_1 = \bar{\varepsilon}_x - \frac{2C_5}{l_x}\sinh\left(\alpha_1 \frac{l_x}{2}\right) \qquad \text{4-3.46}$$

Therefore

$$\bar{u}_1 = \bar{\varepsilon}_x x + C_5\left[\sinh\left(\alpha_1 x\right) - \frac{2x}{l_x}\sinh\left(\alpha_1 \frac{l_x}{2}\right)\right] \qquad \text{4-3.47}$$

and

$$\bar{u}_2 = \bar{\varepsilon}_x x - C_5\left[\frac{h_1 Q_{11}}{h_2 Q_{22}}\sinh\left(\alpha_1 x\right) - \frac{2x}{l_x}\sinh\left(\alpha_1 \frac{l_x}{2}\right)\right] \qquad \text{4-3.48}$$

Since stress is free alone the crack (i.e. $x = \dfrac{l_x}{2}$),

$$\tau_{2xy} = \frac{N_{2xy}}{h_2} = 0$$

but $\dfrac{N_{2xy}}{h_2} = Q_{66}\left(\bar{u}_{2,y} + \bar{v}_{2,x}\right) = 0$

$\bar{u}_{2,y} = 0$. Since the constant $C_2 = 0$

therefore

$$\bar{v}_{2,x} = C_3 + \alpha_2 C_8 \cosh\left(\alpha_2 x\right) = 0$$

then

$$C_3 = -\alpha_2 C_8 \cosh\left(\alpha_2 x\right) \qquad \text{4-3.49}$$

In addition, $N_{xy} l_x = 2\int_{-l_x/2}^{l_x/2}\left(N_{1xy} + N_{2xy}\right)dx$ and $\bar{\tau}_{xy} = \dfrac{N_{xy}}{2\left(h_1 + h_2\right)}$

$$N_{xy}l_x = 2\int_{-l_x/2}^{l_x/2}\left[Q_{66}h_1\left\{C_3 + C_7\alpha_2\cosh\left(\alpha_2 x\right)\right\} + Q_{66}h_2\left\{C_3 + C_8\alpha_2\cosh\left(\alpha_2 x\right)\right\}\right]dx$$

$$N_{xy}l_x = 2\left[Q_{66}h_1\left\{C_3 x + C_7\sinh\left(\alpha_2 x\right)\right\} + Q_{66}h_2\left\{C_3 x + C_8\sinh\left(\alpha_2 x\right)\right\}\right]_{-l_x/2}^{l_x/2}$$

but $C_7 = -\dfrac{h_2}{h_1}C_8$

$$N_{xy}l_x = 2Q_{66}C_3 l_x\left(h_1 + h_2\right)$$

therefore

$$\overline{\tau}_{xy} = Q_{66}C_3 = -Q_{66}2\alpha_2 C_8\cosh\left(\alpha_2\frac{l_x}{2}\right) \qquad 4\text{-}3.50$$

From equilibrium, we can obtain $\sigma_{1x}, \sigma_{1y}, \sigma_{2x}, \sigma_{2y}, \tau_{1xy}$ and τ_{2xy} (see Figure 4-3.2).

$$\sigma_{1x} = \frac{N_{1x}}{h_1} = Q_{11}\overline{u}_{1,x} + Q_{12}\overline{v}_{1,y} + \sigma_{1x}^R \qquad 4\text{-}3.51$$

Define

$$\overline{v}_{1,y} = \overline{v}_{2,y} = \overline{\varepsilon}_y \qquad 4\text{-}3.52$$

where $\overline{\varepsilon}_y$ is the average strain in the y-direction.

Therefore

$$\sigma_{1x} = Q_{11}\left\{C_1 + C_5\alpha_1\cosh\left(\alpha_1 x\right)\right\} + Q_{12}\overline{\varepsilon}_y + \sigma_{1x}^R \qquad 4\text{-}3.53$$

Substituting C_1 in term of C_5 into Equation 4-3.53, and rearrange the equation, we obtain

$$\sigma_{1x} = Q_{11}\left\{\overline{\varepsilon}_x + C_5\left[\alpha_1\cosh\left(\alpha_1 x\right) - \frac{2}{l_x}\sinh\left(\alpha_1\frac{l_x}{2}\right)\right]\right\} + Q_{12}\overline{\varepsilon}_y + \sigma_{1x}^R$$

Let

$$\overline{C}_5 = C_5\sinh\left(\alpha_1 l_x/2\right) \qquad 4\text{-}3.54$$

$$\sigma_{1x} = Q_{11}\left\{\bar{\varepsilon}_x + \bar{C}_5\left[\frac{\alpha_1 \cosh(\alpha_1 x)}{\sinh(\alpha_1 l_x/2)} - \frac{2}{l_x}\right]\right\} + Q_{12}\bar{\varepsilon}_y + \sigma_{1x}^R \qquad \text{4-3.55}$$

Similarly for σ_{1y}

$$\sigma_{1y} = \frac{N_{1y}}{h_1} = Q_{12}\bar{u}_{1,x} + Q_{22}\bar{v}_{1,y} + \sigma_{1y}^R$$

Apply Equation 4-3.52, σ_{1y} can be written as

$$\sigma_{1y} = Q_{12}\left\{C_1 + C_5\alpha_1 \cosh(\alpha_1 x)\right\} + Q_{22}\bar{\varepsilon}_y + \sigma_{1y}^R \qquad \text{4-3.56}$$

Substitute C_1 in term of C_5 into Equation 4-3.56, and rearrange the equation, we obtain

$$\sigma_{1y} = Q_{12}\left\{\bar{\varepsilon}_x + C_5\left[\alpha_1 \cosh(\alpha_1 x) - \frac{2}{l_x}\sinh\left(\alpha_1 \frac{l_x}{2}\right)\right]\right\} + Q_{22}\bar{\varepsilon}_y + \sigma_{1y}^R$$

but $\bar{C}_5 = C_5 \sinh(\alpha_1 l_x/2)$

$$\sigma_{1y} = Q_{12}\left\{\bar{\varepsilon}_x + \bar{C}_5\left[\frac{\alpha_1 \cosh(\alpha_1 x)}{\sinh(\alpha_1 l_x/2)} - \frac{2}{l_x}\right]\right\} + Q_{22}\bar{\varepsilon}_y + \sigma_{1y}^R \qquad \text{4-3.57}$$

The same procedure is used to determine σ_{2x}

$$\sigma_{2x} = \frac{N_{2x}}{h_1} = Q_{22}\bar{u}_{2,x} + Q_{12}\bar{v}_{2,y} + \sigma_{2x}^R$$

but $\bar{v}_{1,y} = \bar{v}_{2,y} = \bar{\varepsilon}_y$

$$\sigma_{2x} = Q_{22}\left\{C_1 + C_6\alpha_1 \cosh(\alpha_1 x)\right\} + Q_{12}\bar{\varepsilon}_y + \sigma_{2x}^R \qquad \text{4-3.58}$$

Substitute C_1 and C_6 in term of C_5 into Equation 4-3.58, and rearrange the equation, we obtain

$$\sigma_{2x} = Q_{22}\left\{\bar{\varepsilon}_x - C_5\left[\frac{Q_{11}h_1}{Q_{22}h_2}\alpha_1 \cosh(\alpha_1 x) + \frac{2}{l_x}\sinh\left(\alpha_1 \frac{l_x}{2}\right)\right]\right\} + Q_{12}\bar{\varepsilon}_y + \sigma_{2x}^R$$

but $\overline{C}_5 = C_5 \sinh\left(\alpha_1 l_x/2\right)$

$$\sigma_{2x} = Q_{22}\left\{\overline{\varepsilon}_x + \overline{C}_5\left[\frac{Q_{11}h_1}{Q_{22}h_2}\frac{\alpha_1\cosh\left(\alpha_1 x\right)}{\sinh\left(\alpha_1 l_x/2\right)} - \frac{2}{l_x}\right]\right\} + Q_{12}\overline{\varepsilon}_y + \sigma_{2x}^R \qquad 4\text{-}3.59$$

Utilize Equations 4-3.52 and 4-3.54 together with the same approach to obtain σ_{2y}. Therefore the σ_{2y} can be expressed as

$$\sigma_{2y} = Q_{12}\left\{\overline{\varepsilon}_x + \overline{C}_5\left[\frac{Q_{11}h_1}{Q_{22}h_2}\frac{\alpha_1\cosh\left(\alpha_1 x\right)}{\sinh\left(\alpha_1 l_x/2\right)} - \frac{2}{l_x}\right]\right\} + Q_{11}\overline{\varepsilon}_y + \sigma_{2y}^R \qquad 4\text{-}3.60$$

As for τ_{1xy} and τ_{2xy}, from the equilibrium (see Figure 4-3.2).

$$\tau_{1xy} = \frac{N_{1xy}}{h_1} = Q_{66}\left(\overline{u}_{1,y} + \overline{v}_{1,x}\right) \qquad 4\text{-}3.61$$

Solve for $\overline{u}_{1,y}$and $\overline{v}_{1,x}$

$$\tau_{1xy} = Q_{66}\left[C_3 + C_7\alpha_2\cosh\left(\alpha_2 x\right)\right]$$

$$\tau_{1xy} = Q_{66}C_3\left[1 + \frac{C_7}{C_3}\alpha_2\cosh\left(\alpha_2 x\right)\right] \qquad 4\text{-}3.62$$

Use Equations 4-3.42, 4-3.50 and 4-3.62, τ_{1xy} can be expressed as following

$$\tau_{1xy} = \overline{\tau}_{xy}\left[1 + \frac{h_2}{h_1}\frac{\cosh\left(\alpha_2 x\right)}{\cosh\left(\alpha_2 l_x/2\right)}\right] \qquad 4\text{-}3.63$$

Similarly,

$$\tau_{2xy} = \frac{N_{2xy}}{h_2} = Q_{66}\left(\overline{u}_{2,y} + \overline{v}_{2,x}\right) \qquad 4\text{-}3.64$$

Solve for $\overline{u}_{1,y}$and $\overline{v}_{1,x}$

$$\tau_{2xy} = Q_{66}\left[C_3 + C_8\alpha_2\cosh\left(\alpha_2 x\right)\right]$$

$$\tau_{2xy} = Q_{66} C_3 \left[1 + \frac{C_8}{C_3} \alpha_2 \cosh(\alpha_2 x) \right] \tag{4-3.65}$$

Solve for Equations 4-3.50 and 4-3.65 in term of τ_{2xy}, we have

$$\tau_{2xy} = \overline{\tau}_{xy} \left[1 - \frac{\cosh(\alpha_2 x)}{\cosh(\alpha_2 l_x / 2)} \right] \tag{4-3.66}$$

The constant $\overline{C}_5$ is obtained from equilibrium conditions as:

$$\begin{aligned} \overline{C}_5 &= \left(\overline{\varepsilon}_x + \frac{Q_{12}}{Q_{22}} \overline{\varepsilon}_y + \frac{1}{Q_{22}} \sigma_{2x}^R \right) \Big/ W_x \\ W_x &= \frac{Q_{11} h_1}{Q_{22} h_2} \alpha_1 \coth\left(\frac{\alpha_1 l_x}{2} \right) + \frac{2}{l_x} \end{aligned} \tag{4-3.67}$$

The stress-strain relations can be shown as

$$\begin{bmatrix} \overline{\varepsilon}_x \\ \overline{\varepsilon}_y \\ \gamma_{xy} \end{bmatrix} = \begin{bmatrix} \frac{I_{22}(h_1+h_2)}{I_{11}I_{22} - I_{12}^2} & \frac{-I_{12}(h_1+h_2)}{I_{11}I_{22} - I_{12}^2} & 0 \\ \frac{-I_{12}(h_1+h_2)}{I_{11}I_{22} - I_{12}^2} & \frac{I_{11}(h_1+h_2)}{I_{11}I_{22} - I_{12}^2} & 0 \\ 0 & 0 & \frac{1}{\rho_G Q_{66}} \end{bmatrix} \left\{ \begin{bmatrix} \overline{\sigma}_x \\ \overline{\sigma}_y \\ \overline{\tau}_{xy} \end{bmatrix} + \begin{bmatrix} J_{11} \\ J_{21} \\ 0 \end{bmatrix} \sigma_{2x}^R \right\} \tag{4-3.68}$$

where

$$\begin{aligned} I_{11} &= Q_{11} h_1 + Q_{22} h_2 - (Q_{11} h_1 + Q_{22} h_2) \frac{2}{l_x W_x} \\ I_{12} &= Q_{12} h_1 + Q_{12} h_2 - (Q_{11} h_1 + Q_{22} h_2) \frac{Q_{12}}{Q_{22}} \frac{2}{l_x W_x} \\ I_{22} &= Q_{22} h_1 + Q_{11} h_2 - (Q_{11} h_1 + Q_{22} h_2) \frac{Q_{12}^2}{Q_{22}^2} \frac{2}{l_x W_x} \\ J_{11} &= \frac{(Q_{11} h_1 + Q_{22} h_2)}{(h_1 + h_2)} \frac{1}{Q_{22}} \frac{2}{l_x W_x} \\ J_{21} &= \frac{(Q_{11} h_1 + Q_{22} h_2)}{(h_1 + h_2)} \frac{Q_{12}}{Q_{22}^2} \frac{2}{l_x W_x} \end{aligned} \tag{4-3.69}$$

The shear modulus reduction ratio ρ_G is from Tsai and Daniel [196]

$$\rho_G = \left[1 + \frac{2h_2}{l_x \alpha_2 h_1} \tanh\left(\frac{l_x \alpha_2}{2}\right)\right]^{-1} \qquad 4\text{-}3.70$$

Thus, the theoretically predicted stress-strain curve is generated. The result is compared with the experimental stress-strain curves (Figure 4-3.3). The predicted curve matches very well with the experimental result up to about 0.6% of strain. It is believed that the dominant failure mode (i.e., transverse cracking in the 90° layers) was only valid up to this range. Beyond that, other failure modes (e.g., fiber breakage and fiber-matrix debonding in the 0° layers) occurred. This is evident from the photos shown in Figure 4-1.6, which were taken during the experiment. As seen in Figures 4-1.6(a) and (b), in the earlier phase of the experiment, where the dominant failure mode was transverse matrix cracking in the 90° layers, the number of transverse cracks increased as the strain increased. The crack numbers quickly saturated as early as 1.0% of strain, as shown in Figures 4-1.6(c) to (f). Thus, the proposed scheme for cross-ply composites is based on transverse cracks only in the 90° layers. As soon as the dominant failure mode changes, the model can no longer hold.

In order to evaluate the effect of crack density on the apparent modulus of elasticity of a composite, a number of experiments had been conducted for $[90°_3/0°_3]_{2S}$ specimens. That is, the 90° layer is the outer layer. Small modifications for the afore-mentioned equations needed to be made to accommodate the inverse of the inner and outer layers. Figure 4-3.4 compares the theoretical predictions of the apparent moduli of elasticity *vs* crack density for both $[0°_3/90°_3]_{2S}$ and $[90°_3/0°_3]_{2S}$ composites versus the experimental results of two $[90°_3/0°_3]_{2S}$ specimens.

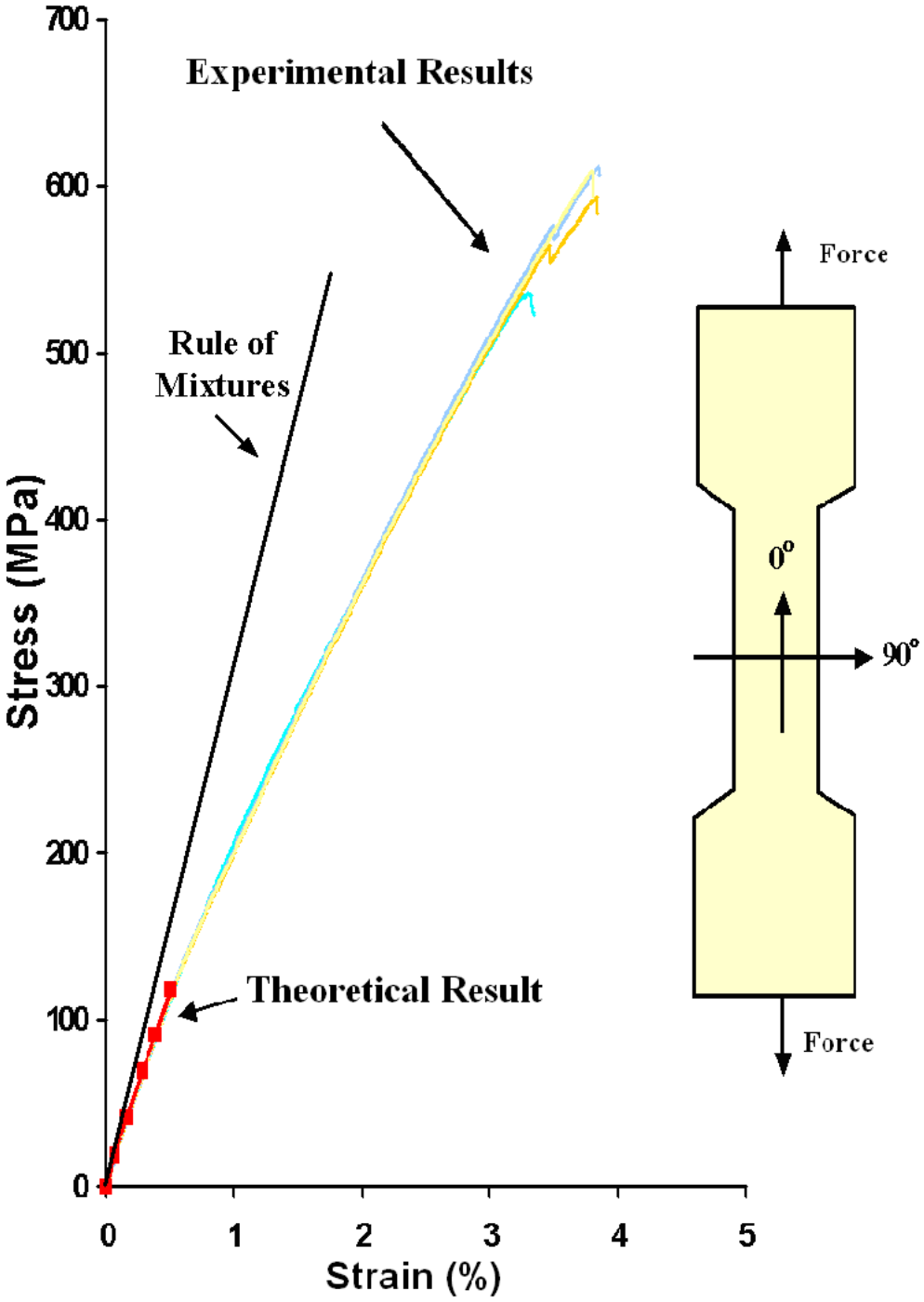

Figure 4-3.3 Comparison between theoretical prediction of room-temperature damaged stress-strain curve versus experimental results for a $[0°_3/90°_3]_{2S}$ cross-ply composite under uniaxial tension.

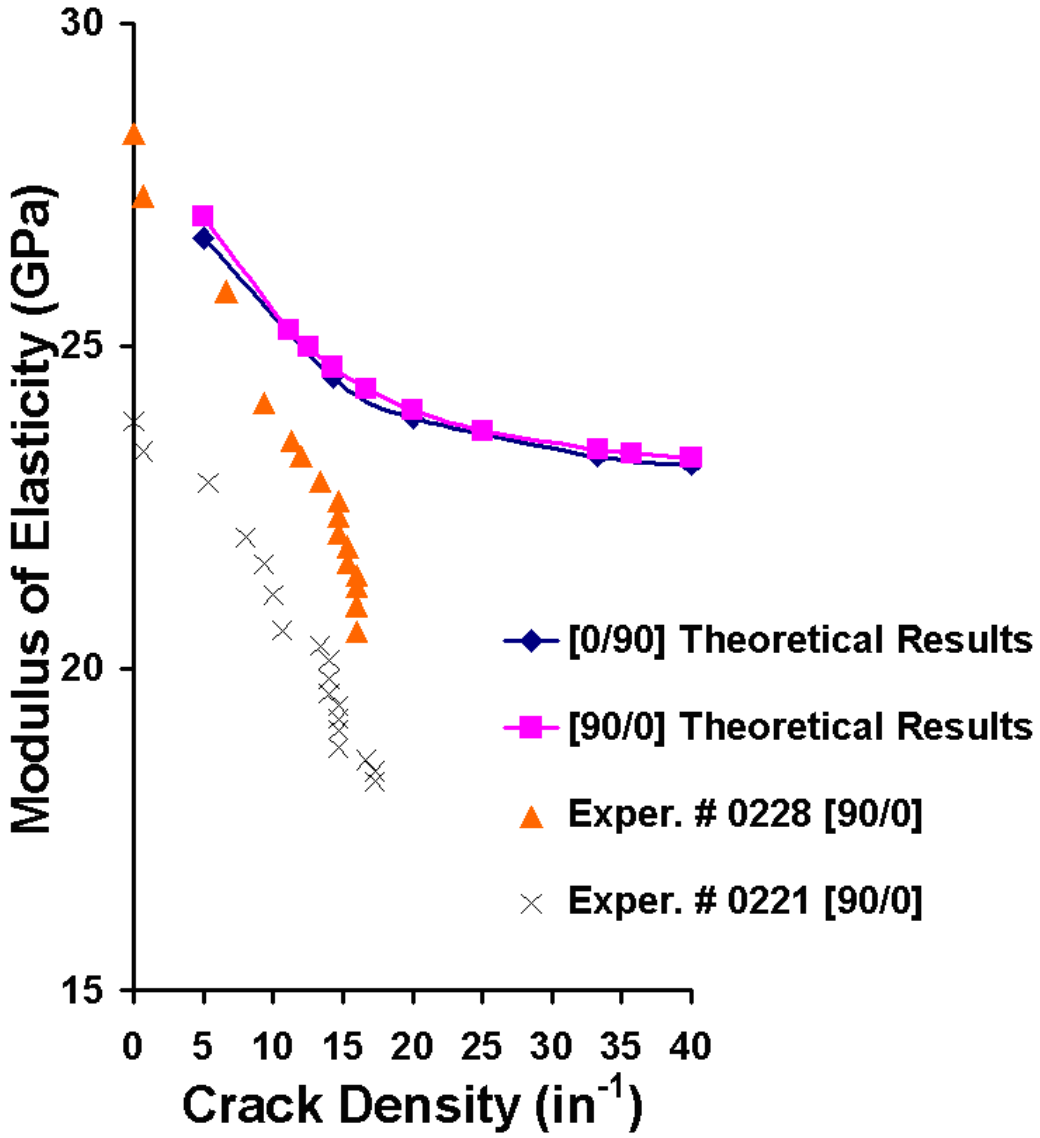

Figure 4-3.4 Comparison of theoretical prediction and experimental results of the room-temperature apparent modulus of elasticity *vs* crack density for $[0°_3/90°_3]_{2S}$ and $[90°_3/0°_3]_{2S}$ cross-ply composites under uniaxial tension.

For the experimental data, the crack density becomes saturated when approaching to about 15 in^{-1} (i.e., 15 cracks per inch), where the apparent modulus of elasticity dropped sharply. However, for the theoretical results, the apparent moduli of elasticity of both types of stacking sequences of the cross-ply composites remain constant when the crack density toward 15 in^{-1} and beyond. It is logical to assume that the dominant failure

mode changes once the crack density reach approximately 15 in^{-1} and other types of failure modes (e.g., fiber breakage and fiber-matrix debonding in 0° layers) will take over at that time.

4.3.2 The $[+45°_3/-45°_3]_{2S}$ specimens

For angle-ply composites under uniaxial tension, the initial failure behavior is shear cracking along the fiber direction, which is similar to the matrix transverse cracking in the above cross-ply composites. The theoretical model proposed in Section 4.3.1 can still be applied once the transformation from material coordinate to specimen coordinate is considered for obtaining proper engineering constants for the $[+45°_3/-45°_3]_{2S}$ (see Jones [6]). From Equation 4-3.68, the laminate compliance matrix can be written as:

$$\begin{bmatrix} S_{xx} & S_{xy} & 0 \\ S_{xy} & S_{yy} & 0 \\ 0 & 0 & S_{ss} \end{bmatrix} = \begin{bmatrix} \dfrac{I_{22}(h_1+h_2)}{I_{11}I_{22}-I_{12}^2} & \dfrac{-I_{12}(h_1+h_2)}{I_{11}I_{22}-I_{12}^2} & 0 \\ \dfrac{-I_{12}(h_1+h_2)}{I_{11}I_{22}-I_{12}^2} & \dfrac{I_{11}(h_1+h_2)}{I_{11}I_{22}-I_{12}^2} & 0 \\ 0 & 0 & \dfrac{1}{\rho_G Q_{66}} \end{bmatrix} \qquad \text{4-3.71}$$

The transformed laminate compliances are:

$$\begin{aligned}
\overline{S}_{xx} &= S_{xx}\cos^4\theta + 2\left(S_{xy}+2S_{ss}\right)\sin^2\theta\cos^2\theta + S_{yy}\sin^4\theta \\
\overline{S}_{xy} &= \left(S_{xx}+S_{yy}-4S_{ss}\right)\sin^2\theta\cos^2\theta + S_{xy}\left(\sin^4\theta+\cos^4\theta\right) \\
\overline{S}_{yy} &= S_{xx}\sin^4\theta + 2\left(S_{xy}+2S_{ss}\right)\sin^2\theta\cos^2\theta + S_{yy}\cos^4\theta \\
\overline{S}_{xs} &= \left(S_{xx}-S_{yy}-2S_{ss}\right)\sin\theta\cos^3\theta + \left(S_{xy}-S_{yy}+2S_{ss}\right)\sin^3\theta\cos\theta \\
\overline{S}_{ys} &= \left(S_{xx}-S_{yy}-2S_{ss}\right)\sin^3\theta\cos\theta + \left(S_{xy}-S_{yy}+2S_{ss}\right)\sin\theta\cos^3\theta \\
\overline{S}_{ss} &= \left(S_{xx}+S_{yy}-2S_{xy}-2S_{ss}\right)\sin^2\theta\cos^2\theta + S_{ss}\left(\sin^4\theta+\cos^4\theta\right)
\end{aligned} \qquad \text{4-3.72}$$

The engineering constants can be written as:

$$\bar{S}_{xx} = \frac{1}{\bar{E}_x},\ \bar{S}_{xy} = -\frac{\bar{\nu}_{xy}}{\bar{E}_x} = -\frac{\bar{\nu}_{yx}}{\bar{E}_y},\ \bar{S}_{yy} = \frac{1}{\bar{E}_y}$$
$$\bar{S}_{ss} = \frac{1}{\bar{G}_{xy}},\ \bar{S}_{xs} = \frac{\eta_{xs}}{\bar{E}_x} = \frac{\eta_{sx}}{\bar{G}_{xy}} \text{ and } \bar{S}_{ys} = \frac{\eta_{ys}}{\bar{E}_y} = \frac{\eta_{sy}}{\bar{G}_{xy}} \qquad \text{4-3.73}$$

The theoretically-predicted stress-strain curve for the $[+45°_3/–45°_3]_{2S}$ specimen is thus generated, as shown in Figure 4-3.5. When compared to the experimental data, the predicted curve matches very well up to 1.8% of strain. Beyond that value, it is believed that the shear failure on the –45° layers as well as delamination between the layers became dominant. As shown in Figure 4-1.7, this is evident from the photos of a $[+45°_3/–45°_3]_{2S}$ specimen taken at various strain levels. At the early stage of loading, the cracks began to propagate from the edge toward the center of the specimen. At the same time, the number of cracks increased. The dominant failure mode during that period was shear cracking along 45° direction. When the strain reached about 3.0%, the number of cracks became saturated, indicating other types of failure (e.g., shear failure along the –45° direction and delamination) play more dominant roles and the proposed theoretical model ceases to be valid at that point.

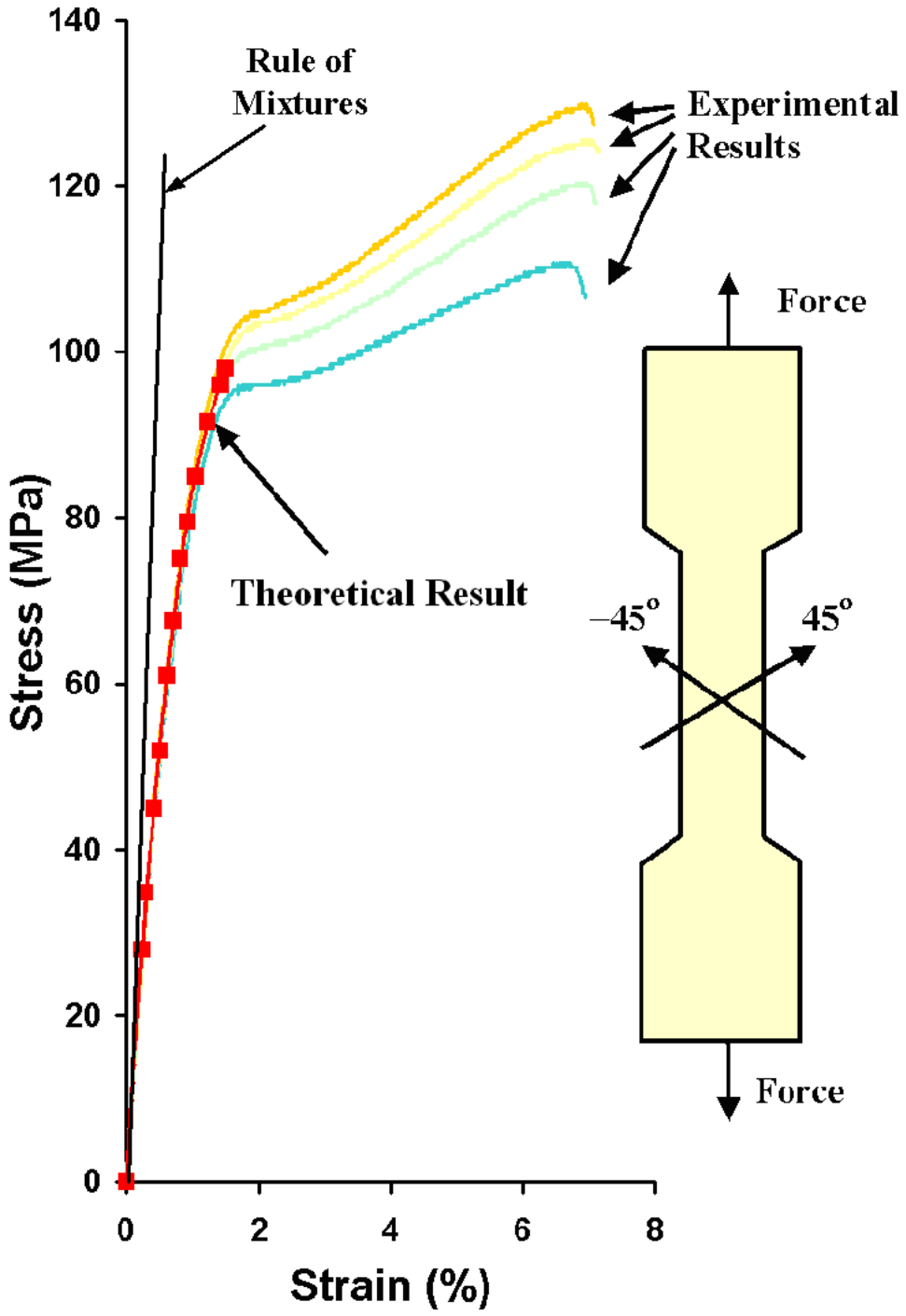

Figure 4-3.5 Comparison between theoretical prediction of room-temperature damaged stress-strain curve versus experimental results for a $[+45°_3/-45°_3]_{2S}$ angle-ply composite under uniaxial tension.

4.3.3 The $[0°_3/+45°_3/90°_3/–45°_3]_S$ specimens

The initial failure behavior of this quasi-isotropic composite can be considered as the combination of the cross-ply and angle-ply composites considered in Sections 4.3.1 and 4.3.2. The photos of failure progression shown in Figures 4-1.8 and 4-1.9 can validate this point. Thus, the technique developed in Sections 4.3.1 and 4.3.2 will be adopted here to analyze this type of composites.

For $[0°_3/+45°_3/90°_3/–45°_3]_S$ specimens, additional steps were needed to obtain the analytical solution. Since four different configurations in the specimens and the scheme was designed for only two, namely [0°] and [90°] or [+45°] and [–45°], the necessary input properties need to modify. Utilize the experimental moduli from $[0°_3/90°_3]_{2S}$ and $[+45°_3/–45°_3]_{2S}$ specimens as the longitudinal and transverse moduli for the $[0°_3/+45°_3/90°_3/–45°_3]_S$ specimens, respectively. The governing equation shown in Equation 4-3.34::

$$
\begin{aligned}
&Q_{22}\overline{u}_{2,xx}+Q_{12}\overline{v}_{2,xy}+Q_{66}\left(\overline{u}_{2,yy}+\overline{v}_{2,xy}\right)=\frac{H_{11}}{h_2}\left(\overline{u}_2-\overline{u}_1\right)\\
&Q_{11}\overline{u}_{1,xx}+Q_{12}\overline{v}_{1,xy}+Q_{66}\left(\overline{u}_{1,yy}+\overline{v}_{1,xy}\right)=\frac{H_{11}}{h_1}\left(\overline{u}_1-\overline{u}_2\right)\\
&Q_{11}\overline{v}_{1,yy}+Q_{12}\overline{u}_{2,xy}+Q_{66}\left(\overline{u}_{2,xy}+\overline{v}_{2,xx}\right)=\frac{H_{22}}{h_2}\left(\overline{v}_2-\overline{v}_1\right)\\
&Q_{22}\overline{v}_{1,yy}+Q_{12}\overline{u}_{1,xy}+Q_{66}\left(\overline{u}_{1,xy}+\overline{v}_{1,xx}\right)=\frac{H_{22}}{h_1}\left(\overline{v}_1-\overline{v}_2\right)
\end{aligned}
\qquad \text{4-3.74}
$$

and displacement field shown in Equation 4-3.35:

$$
\begin{aligned}
\overline{u}_1&=C_1x+C_2y+C_5\sinh\left(\alpha_1x\right)\\
\overline{u}_2&=C_1x+C_2y+C_6\sinh\left(\alpha_1x\right)\\
\overline{v}_1&=C_3x+C_4y+C_7\sinh\left(\alpha_2x\right)\\
\overline{v}_2&=C_3x+C_4y+C_8\sinh\left(\alpha_2x\right)
\end{aligned}
\qquad \text{4-3.75}
$$

can be applied to obtain the stress-strain relation. Here, the stiffnesses in the governing equations were obtained from experimental moduli of the $[0°_3/90°_3]_{2S}$ and $[+45°_3/–45°_3]_{2S}$ specimens. The same stress-strain relations, Equation 4-3.68, can also be used for this configuration.

$$\begin{bmatrix} \overline{\varepsilon}_x \\ \overline{\varepsilon}_y \\ \gamma_{xy} \end{bmatrix} = \begin{bmatrix} \dfrac{I_{22}(h_1+h_2)}{I_{11}I_{22}-I_{12}^2} & \dfrac{-I_{12}(h_1+h_2)}{I_{11}I_{22}-I_{12}^2} & 0 \\ \dfrac{-I_{12}(h_1+h_2)}{I_{11}I_{22}-I_{12}^2} & \dfrac{I_{11}(h_1+h_2)}{I_{11}I_{22}-I_{12}^2} & 0 \\ 0 & 0 & \dfrac{1}{\rho_G Q_{66}} \end{bmatrix} \left\{ \begin{bmatrix} \overline{\sigma}_x \\ \overline{\sigma}_y \\ \overline{\tau}_{xy} \end{bmatrix} + \begin{bmatrix} J_{11} \\ J_{21} \\ 0 \end{bmatrix} \sigma_{2x}^R \right\} \qquad \text{4-3.76}$$

The theoretically-predicted stress-strain curve for the $[0°_3/+45°_3/90°_3/–45°_3]_S$ specimen is thus generated, as shown in Figure 4-3.6. When compared to the experimental data, the analytically-predicted result matches very well up to 1.8% of strain. The experimental results presented in the photos of Figures 4-1.8 and 4-1.9 indicate that the initial phase of cracks (i.e., transverse cracks in the 90° layers and shear cracks in the 45° layers) were initiated at the beginning of loading and became saturated when the strain was about 2.0%. Beyond that range, other types of failure modes (e.g., delamination and fiber breakage in 0° layers) become dominant and the proposed theoretical model can no longer work.

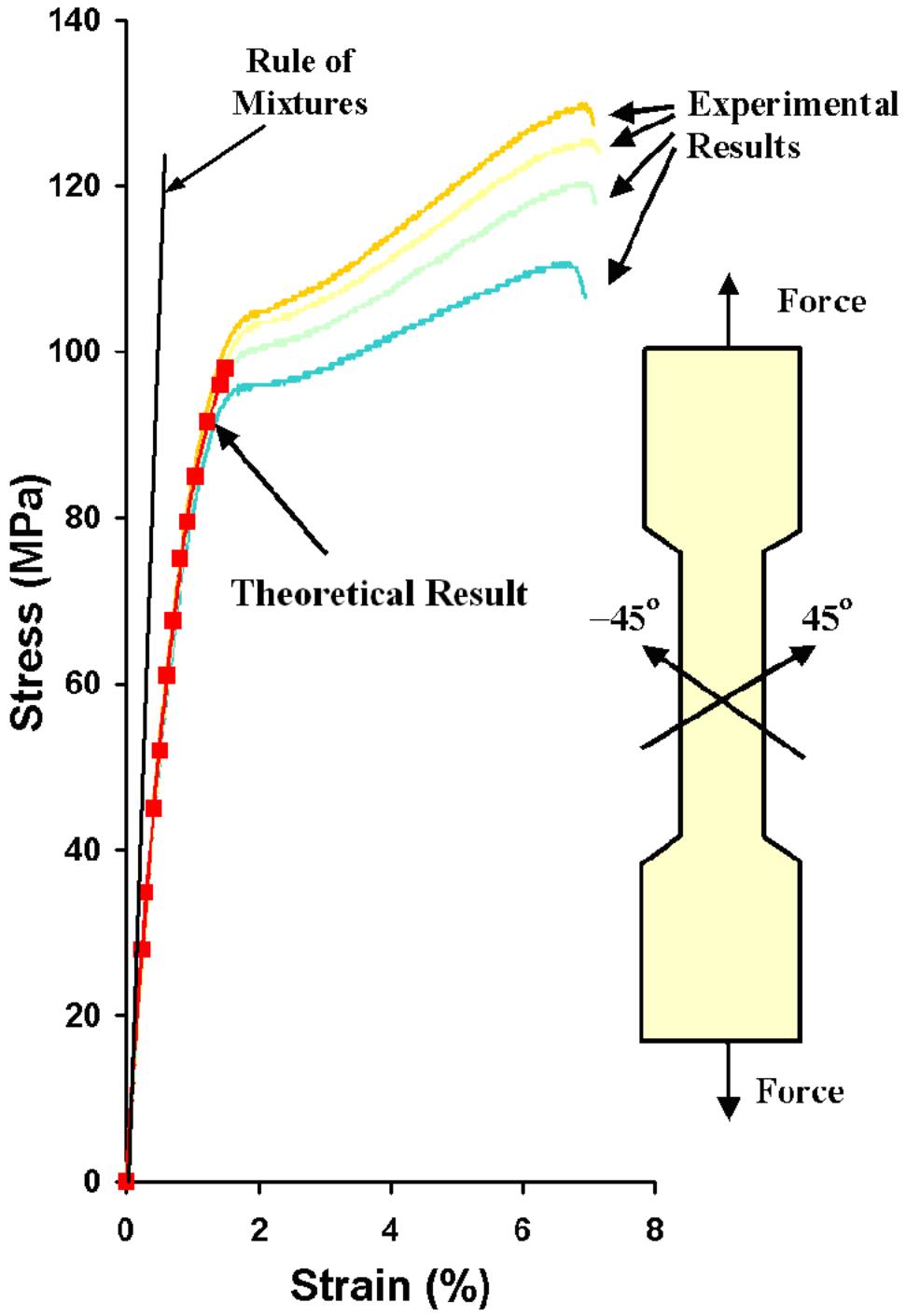

Figure 4-3.6 Comparison between theoretical prediction of room-temperature damaged stress-strain curve versus experimental results for a $[0°_3/+45°_3/90°_3/-45°_3]_S$ quasi-isotropic under uniaxial tension.

CHAPTER 5

COMPOSITE STRIPS WITH A CENTER HOLE OR A PIN-JOINT

5.1 The Material and the specimens

The S2-glass/toughened-epoxy composite with 44% fiber volume fraction, which was investigated in Chapter 4 for dog-bone shaped specimens under uniaxial tension, is studied in this Chapter for the effect of stress concentration; namely, a composite strip with a center hole or a pin-joint under tension. Figure 5-1.1(a) shows a 10"×1.5" composite strip with a center hole size of 1/2", 3/8", 1/4" and 1/8" whereas Figure 5-1.1(b) shows a 5"×1.5" pin-joint composite strip with a pin size of 1/2" and 1/4". For the joint specimens, the distance from the center of the hole to the edge, H, was either 0.75" or 1.5".

The lay-up configurations investigated here for both types of composite strips with stress concentration were the same as the ones studies in the previous MTS tensile tests (Chapter 4). That is, the unidirectional $[0°]_{24\text{-ply}}$, the cross-ply $[0^{o}_{3}/90^{o}_{3}]_{2S}$, the angle-ply $[+45^{o}_{3}/-45^{o}_{3}]_{2S}$ and the quasi-isotropic $[0^{o}_{3}/+45^{o}_{3}/90^{o}_{3}/-45^{o}_{3}]_{S}$.

5.1.1 Tensile testing of composite strips with a center hole

5.1.1.1 Description of experiments: Composite strips with a center hole under tension was tested at low, room and high temperatures in the afore-mentioned MTS testing machine equipped with an environmental chamber. To determine the local strains at locations around the hole, strain gages were mounted on the specimen, which was then gripped in the MTS testing machine and loaded until failure. The tests were conducted at room temperature, 75ºC, 125ºC, –20ºC or –60ºC. For the high and low temperatures the environmental chamber was used. Each test was repeated for 3 or 4 specimens. The

average strain was calculated by dividing the motion of the crosshead with the length of the specimens. The average stress was determined by dividing the applied force with the cross-sectional area of the strip. The stress-strain curve for each specimen was thus constructed. In addition, a digital camera was used to capture the progressive failure of the specimens at different stages of strain level.

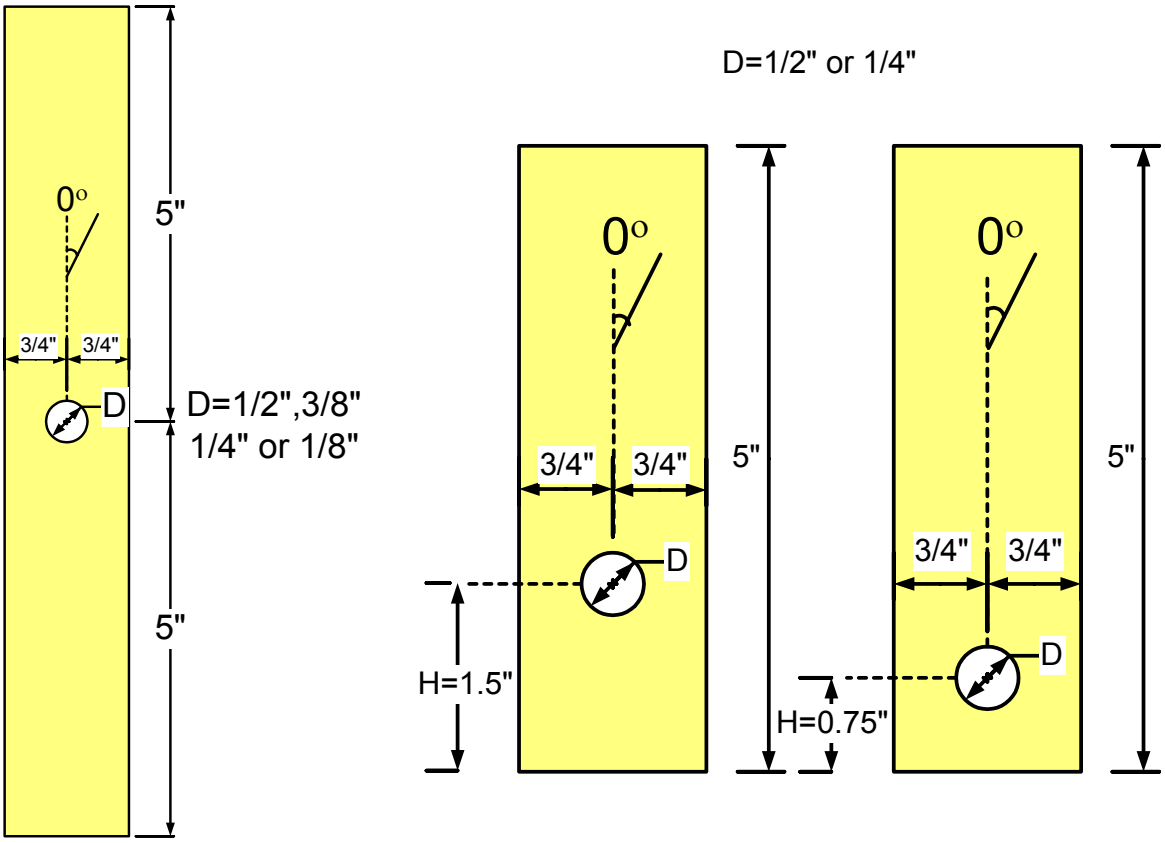

(a) center-hole specimen (b) pin-joint specimens

Figure 5-1.1 Composite strips with (a) a center hole and (b) a pin-joint with two different H values.

5.1.1.2 Results: Since many parameters (e.g., temperature, hole size, stacking sequence, etc.) were varied for this study, a vast amount of data was generated. Figure 5-1.2(a) shows the stress-strain curves of three $[0^o]_{24\text{-ply}}$ unidirectional composite strips with a 1/2" center hole tested at room temperature. The specimens did not break

completely because of the occurrence of slippage at the MTS hydraulic grips. Figure 5-1.3 shows a sequence of fractographs taken during testing. At 0.5% of strain, two pairs of small cracks along the fiber direction were found from the two extreme vertical tangents of the hole due to high stress concentration. The cracks propagated further along the fiber direction as the strain increased and eventually rendered the specimen disintegrated completely at about 4.0% of strain. Post-mortem inspection indicated that fiber breakage and its resultant shear-out along fiber-matrix interfaces were the dominant failure modes of this type of specimens.

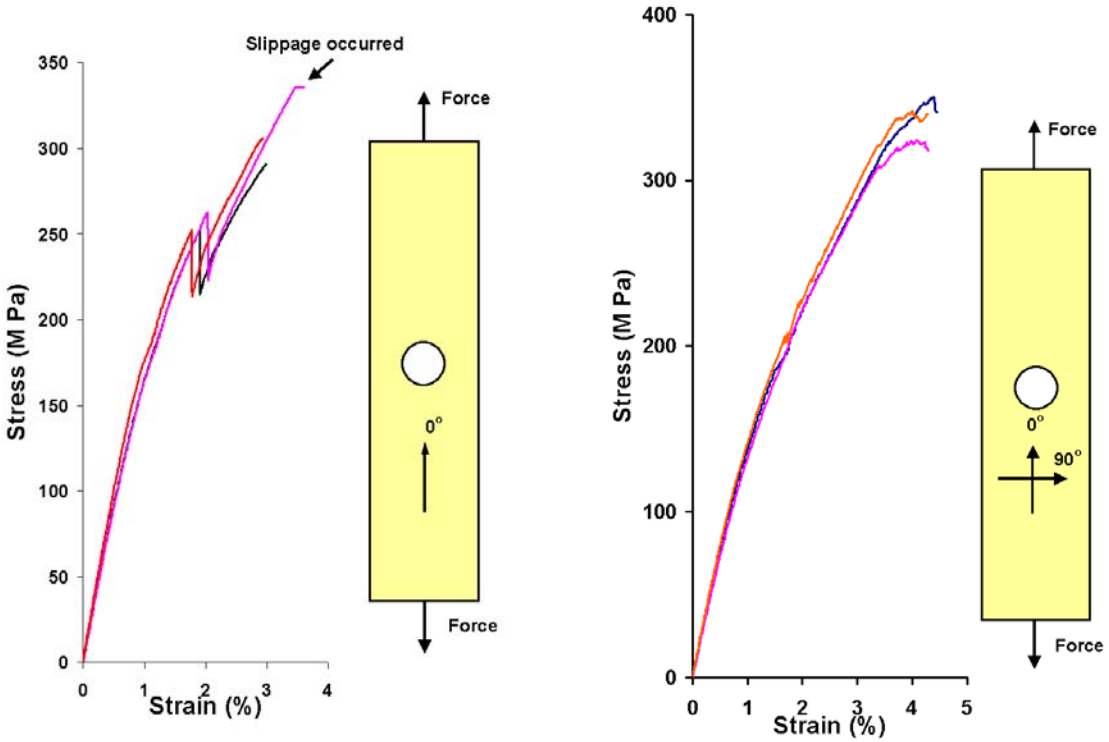

(a) $[0^o]_{24\text{-ply}}$ (b) $[0^o_3/90^o_3]_{2S}$

Figure 5-1.2 Stress-strain curves for unidirectional $[0^o]_{24\text{-ply}}$ and cross-ply $[0^o_3/90^o_3]_{2S}$ composite strips with a center hole of 1/2" diameter tested under tensile loading at room temperature.

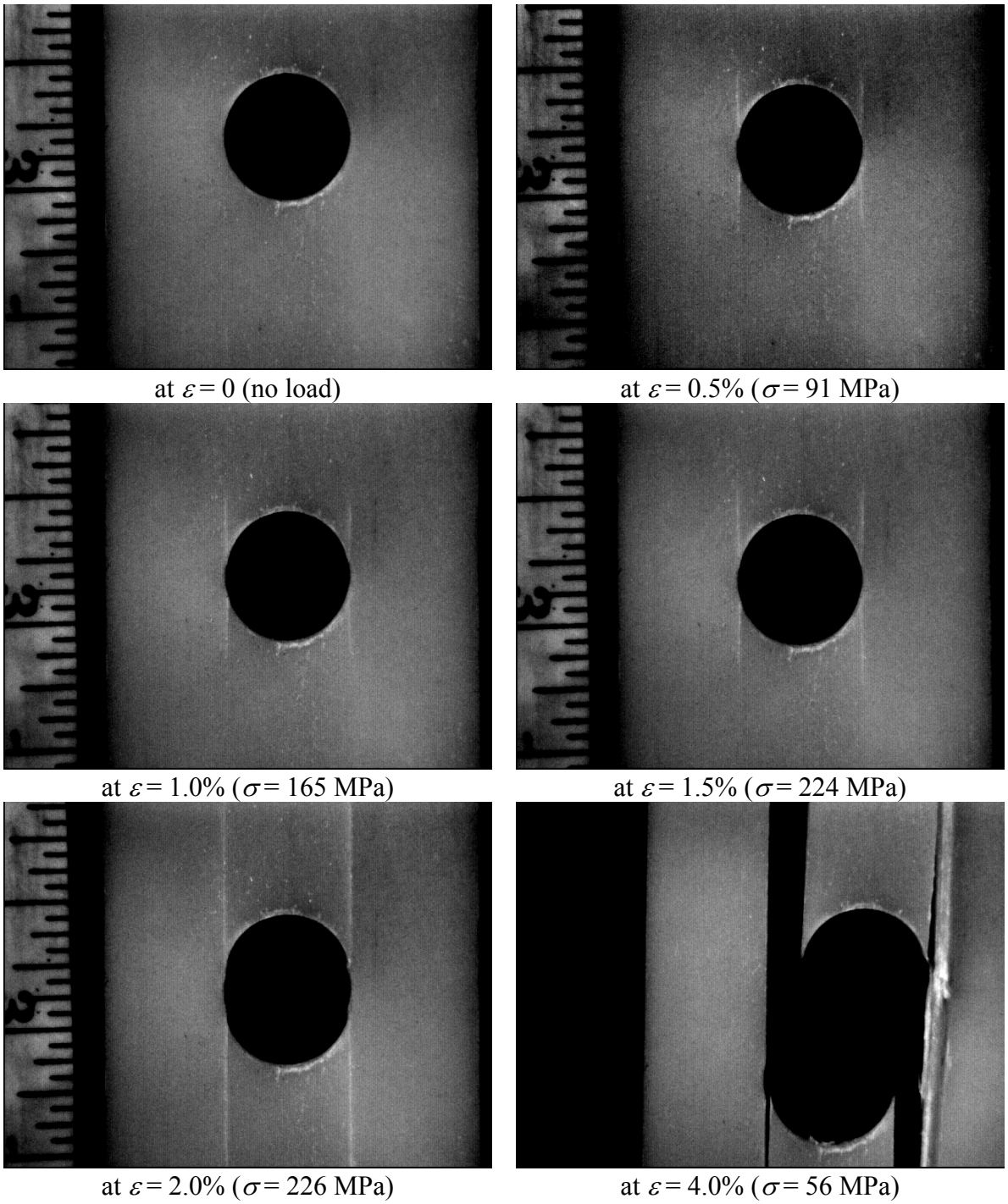

Figure 5-1.3 Tensile-induced progressive failure of a $[0^o]_{24\text{-ply}}$ unidirectional composite strip specimen with a center hole (D = 0.5") at room temperature.

Figure 5-1.2(b) shows the stress-strain curves of three $[0^o_3/90^o_3]_{2S}$ cross-ply composite strips with a 1/2" center hole tested at room temperature. The specimens failed at a stress level of 325 MPa with a failure strain of 4.5%. The corresponding fractographs

of this type of specimens are shown in Figure 5-1.4. Again, the pair of cracks formed at the two extreme vertical tangents of the hole and propagated along the fiber direction. As the strain increased, these cracks continued to propagate until the specimen failed at about 4% of strain. It is believed the [90º] layers failed much earlier than the [0º] layers. Post-mortem observation depicts that again fiber breakage accompanied by shear-out along fiber-matrix interfaces was the dominant failure mode in the 0º layers. On the other hand, transverse matrix cracking was the dominant failure mode in the 90º layers. As in the dog-bone shaped specimens discussed in Chapter 4, even though a [90º] layer might have failed, it could still transfer load to adjacent [0º] layers through interlaminar shear transfer; resulting the ultimate failure load in a $[0^{\circ}_3/90^{\circ}_3]_{2S}$ cross-ply composite much higher than half of the ultimate failure load in a $[0^{\circ}]_{24\text{-ply}}$ unidirectional composite.

Figure 5-1.5 shows the stress-strain curves for angle-ply $[+45^{\circ}_3/-45^{\circ}_3]_{2S}$ and quasi-isotropic $[0^{\circ}_3/+45^{\circ}_3/90^{\circ}_3/-45^{\circ}_3]_S$ composite strips with a center hole of varying hole sizes under tensile loading at room temperature. As shown in the figure, stiffness, failure strength and strain at failure of these two types of lay-up configurations all increase with a decreasing hole size. For example, the failure strength and strain increase from approximately 60 MPa and 1% to 95 MPa and 2% as the hole diameter is decreased from 0.5” to 0.125”.

From the fractographs shown in Figure 5-1.6, for the $[+45^{\circ}_3/-45^{\circ}_3]_{2S}$ angle-ply case, a pair of cracks emanated diagonally from the edges of the hole at a strain level of 0.25%. More slanted cracks in parallel with the original cracks were formed as the strain level was increased. The specimen completely botched at about 3.0% of strain. During

this process, the dominant failure is believed to be shear failure along fiber-matrix interfaces.

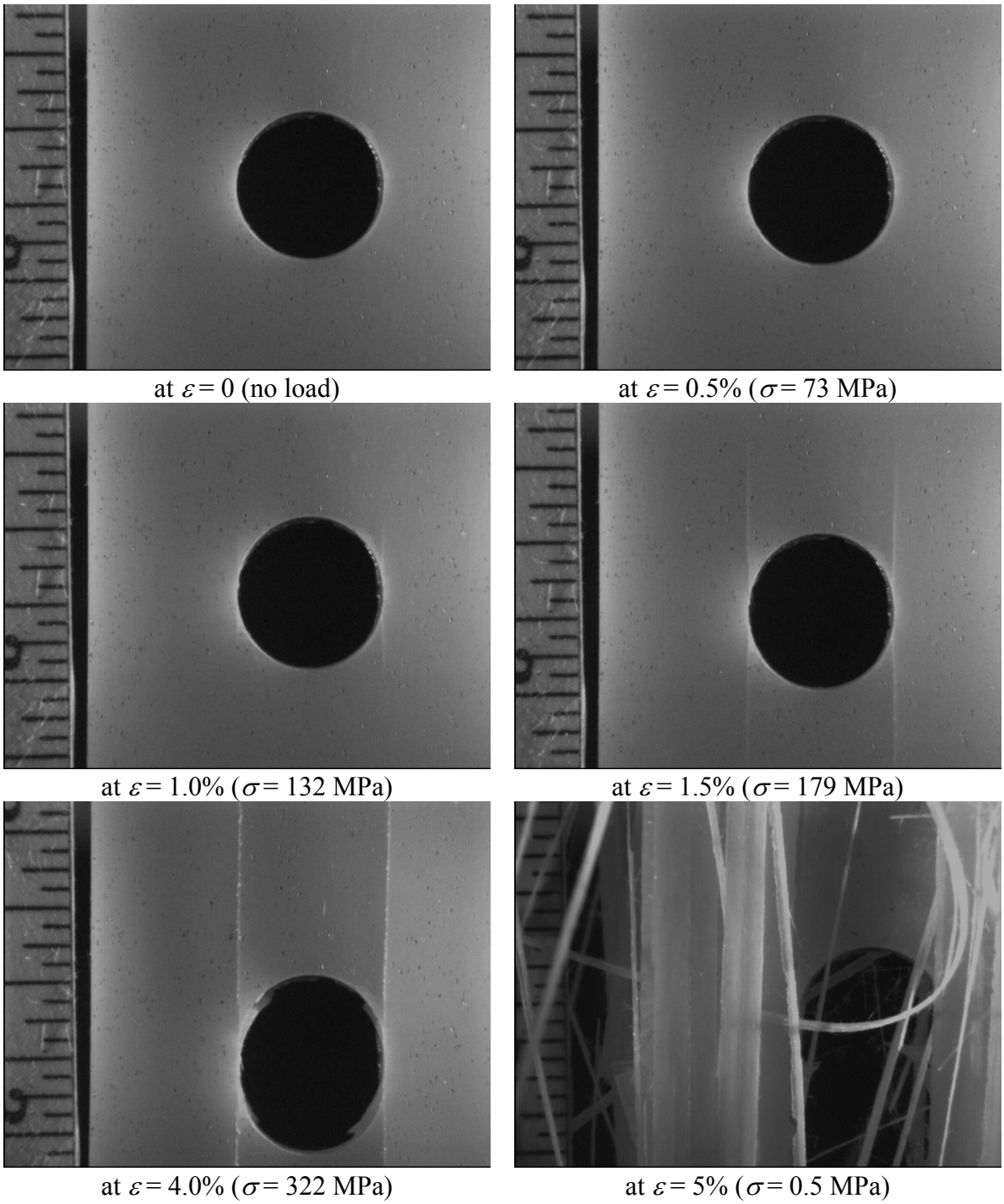

at $\varepsilon = 0$ (no load) at $\varepsilon = 0.5\%$ ($\sigma = 73$ MPa)

at $\varepsilon = 1.0\%$ ($\sigma = 132$ MPa) at $\varepsilon = 1.5\%$ ($\sigma = 179$ MPa)

at $\varepsilon = 4.0\%$ ($\sigma = 322$ MPa) at $\varepsilon = 5\%$ ($\sigma = 0.5$ MPa)

Figure 5-1.4 Tensile-induced progressive failure of a $[0^o_3/90^o_3]_{2S}$ cross-ply composite strip specimen with a center hole (D = 0.5") at room temperature.

Finally without surprise, for the $[0^{o}_{3}/+45^{o}_{3}/90^{o}_{3}/-45^{o}_{3}]_{S}$ quasi-isotropic case, the above-mentioned failure modes dominant their respective layers; i.e., shear-out along fiber-matrix interfaces with fiber breakage for the 0º layers; transverse matrix cracking for the 90º layers, and shear failure along fiber-matrix interfaces for the 45º layers. As shown in the fractographs (Figure 5-1.7), at about a strain level of 1%, cracks were formed at the tangential to the hole along the fiber direction in the 0º layers. The [90º] and [±45º] layers were believed to have failed before this strain level; causing the 0º layers, though damaged also, to carry the load. With the increasing strain level, cracks in the 0º layers propagated in the similar manner as the [0º] layers in the other lay-up configurations. At a strain level around 1.5%, broken fibers of the surface [0º] layer detached from the specimen to reveal the inner layers. Finally the specimen failed at about 2.5% of strain.

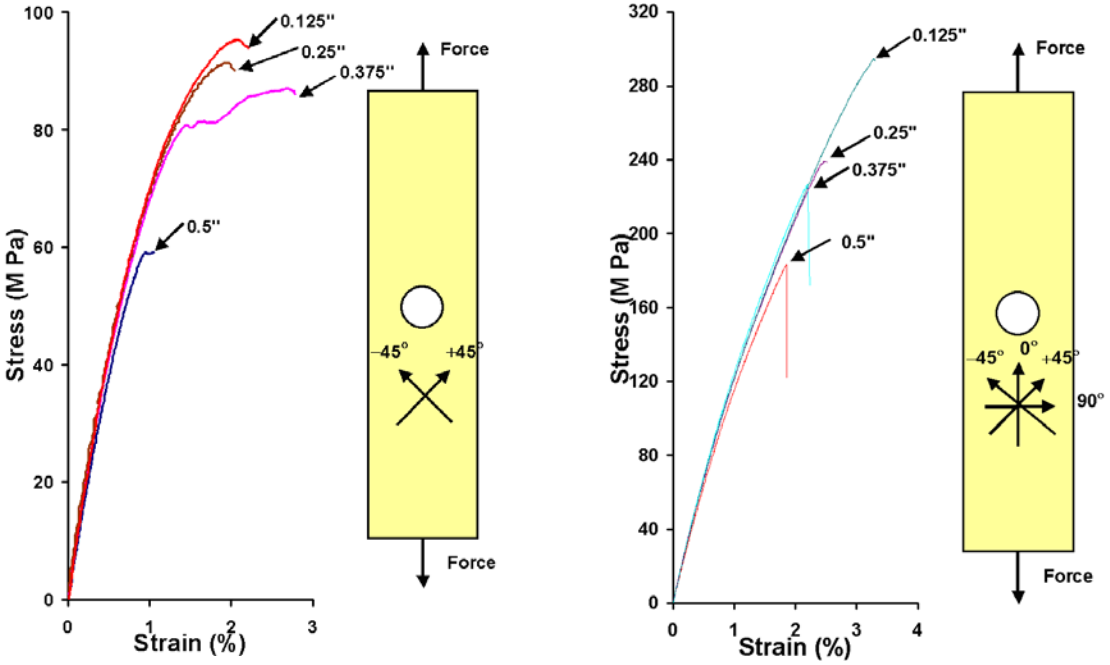

(a) $[+45^{o}_{3}/-45^{o}_{3}]_{2S}$ (b) $[0^{o}_{3}/+45^{o}_{3}/90^{o}_{3}/-45^{o}_{3}]_{S}$

Figure 5-1.5 Stress-strain curves for angle-ply $[+45^{o}_{3}/-45^{o}_{3}]_{2S}$ and quasi-isotropic $[0^{o}_{3}/+45^{o}_{3}/90^{o}_{3}/-45^{o}_{3}]_{S}$ composite strips with a center hole of varying hole sizes under tensile loading at room temperature.

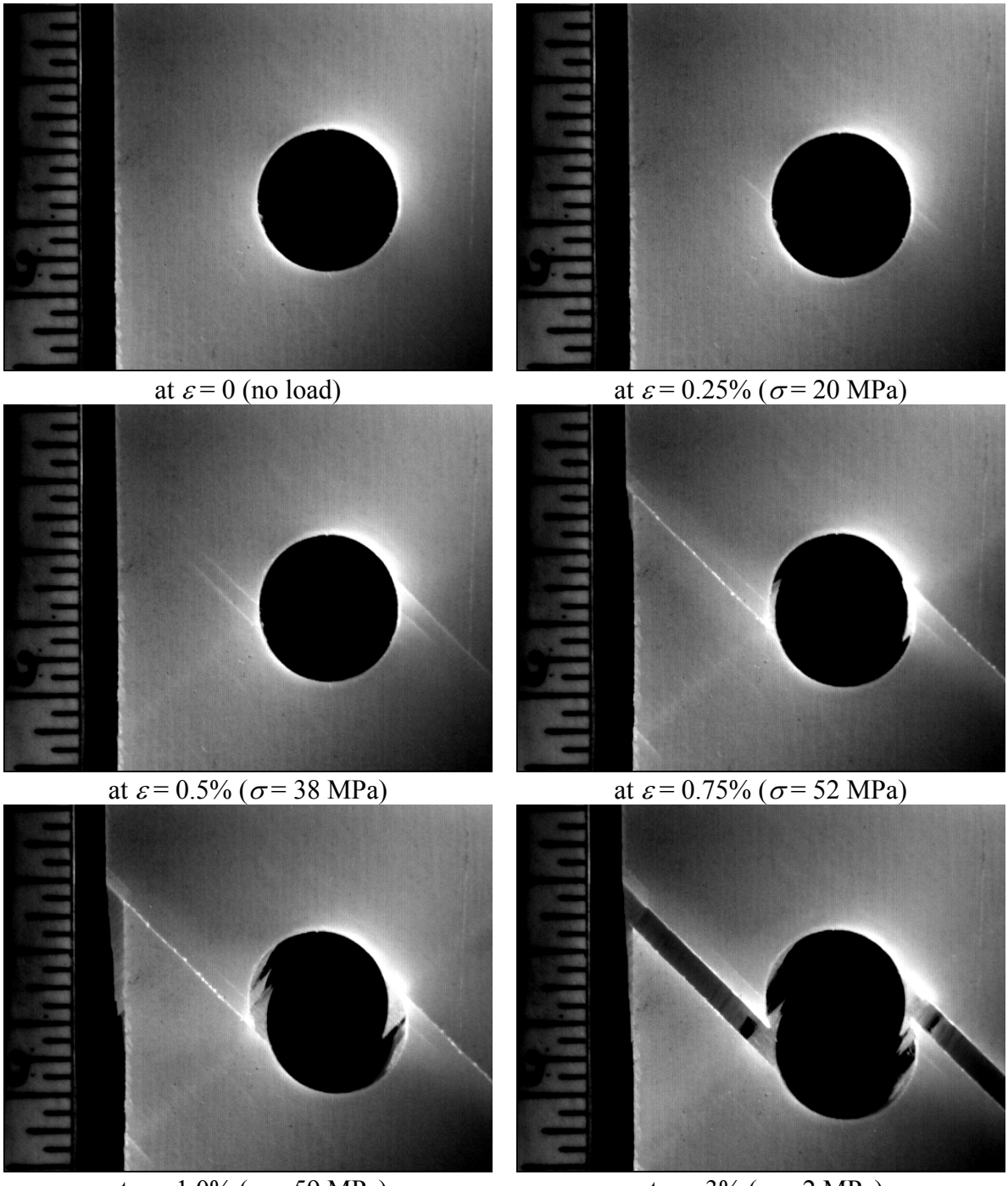

Figure 5-1.6 Tensile-induced progressive failure of a $[+45^{o}_{3}/-45^{o}_{3}]_{2S}$ angle-ply composite strip specimen with a center hole (D = 0.5") at room temperature.

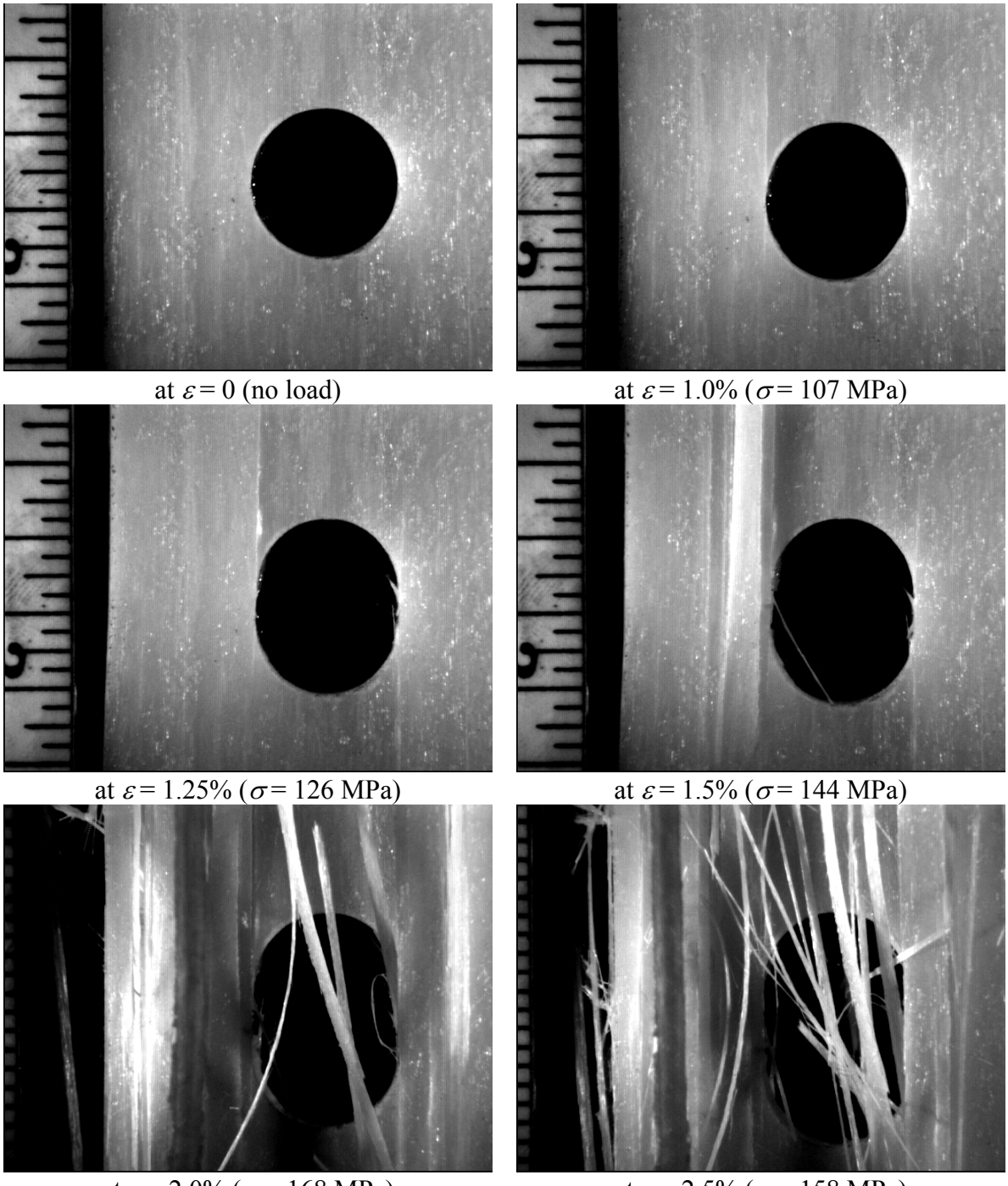

at $\varepsilon = 0$ (no load) at $\varepsilon = 1.0\%$ ($\sigma = 107$ MPa)

at $\varepsilon = 1.25\%$ ($\sigma = 126$ MPa) at $\varepsilon = 1.5\%$ ($\sigma = 144$ MPa)

at $\varepsilon = 2.0\%$ ($\sigma = 168$ MPa) at $\varepsilon = 2.5\%$ ($\sigma = 158$ MPa)

Figure 5-1.7 Tensile-induced progressive failure of a $[0^{o}_{3}/+45^{o}_{3}/90^{o}_{3}/-45^{o}_{3}]_{S}$ quasi-isotropic composite strip specimen with a center hole (D = 0.5") at room temperature.

Figure 5-1.8 compares the effect of stacking sequence on the stress-strain curves of composite strips of a 1/2" center hole under uniaxial tension at room temperature. As expected, the stiffness, strength and strain at failure decreases in the order of the four configurations: $[0^o_3]_{24\text{-ply}}$, $[0^o_3/90^o_3]_{2S}$, $[+45^o_3/-45^o_3]_{2S}$ and $[0^o_3/+45^o_3/90^o_3/-45^o_3]_S$. Figures 5-1.9 and 5-1.10 show the effect of temperature on $[+45^o_3/-45^o_3]_{2S}$ and $[0^o_3/+45^o_3/90^o_3/-45^o_3]_S$ laminates with various hole sizes. The results indicate that as expected temperature has significant effects on stiffness, failure strength and failure strain of the composite strips. In general, as temperature is lower, the stiffness and failure strength increase whereas the strain at failure decreases. With the exception of the $[0^o_3/+45^o_3/90^o_3/-45^o_3]_S$ laminates at low temperature tests, where slippage occurred.

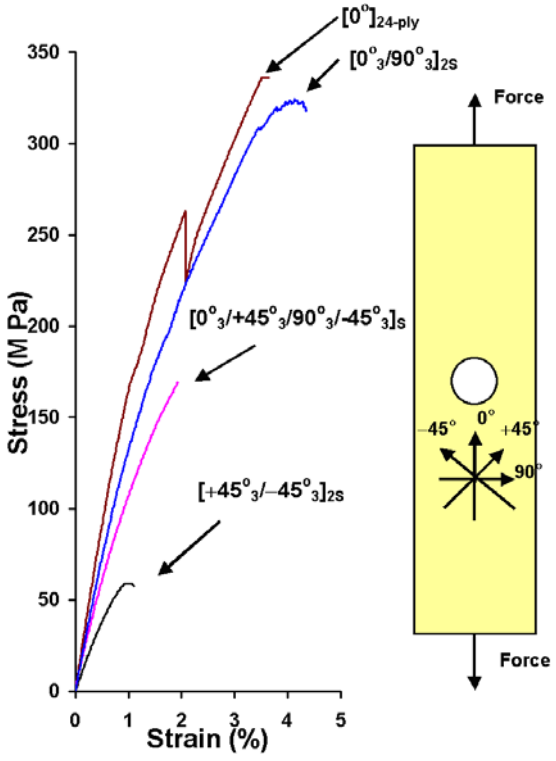

Figure 5-1.8 Comparison of stress-strain curves for various stacking sequences of S2 glass/toughened epoxy composite strips with a center hole of 0.5" diameter under tensile loading at room temperature.

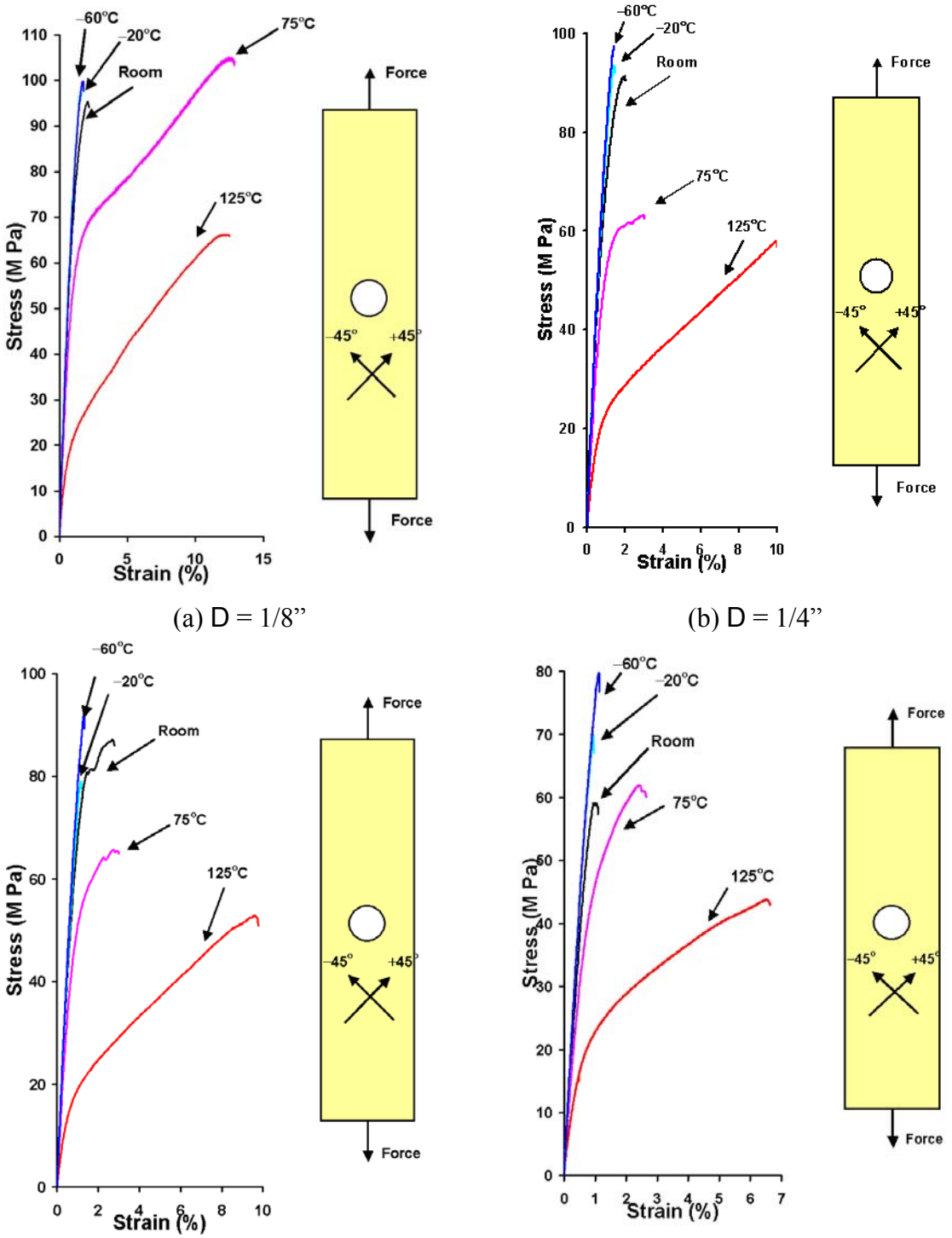

Figure 5-1.9 Stress-strain curves for angle-ply $[+45^{o}_{3}/-45^{o}_{3}]_{2S}$ composite strips with a center hole of various hole sizes under tensile loading at varying temperatures.

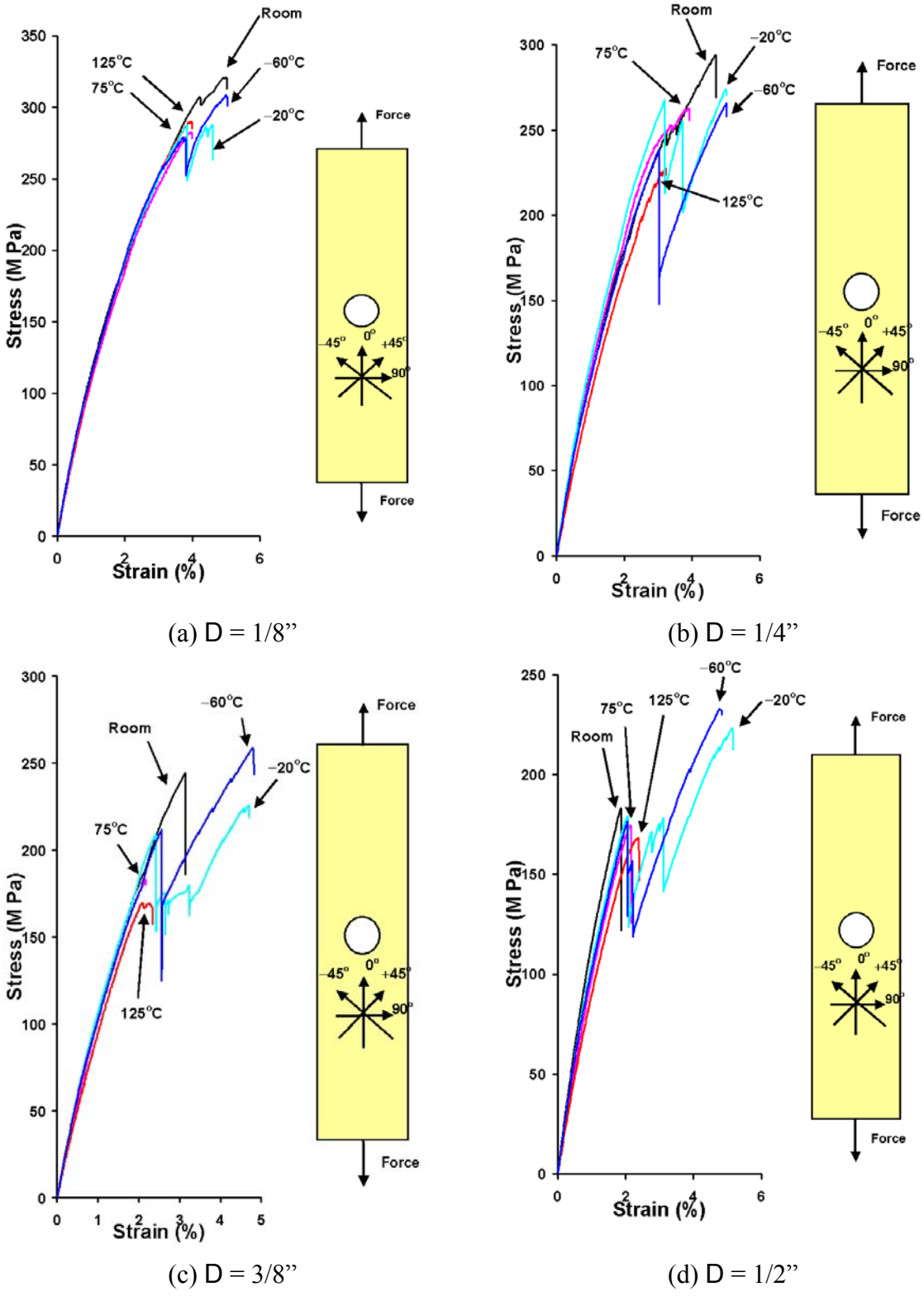

Figure 5-1.10 Stress-strain curves for quasi-isotropic $[0^{o}_{3}/+45^{o}_{3}/90^{o}_{3}/-45^{o}_{3}]_{S}$ composite strips with a center hole various hole sizes under tensile loading at varying temperatures.

5.1.2 Tensile testing of composite joints

5.1.2.1 Description of experiments: Again the same composite material was tested in this experiment. The dimensions of the composite pin-joint specimens were shown in Figure 5-1.1(b) in the beginning of this chapter. Figure 5-1.15(a) shows a picture of a pin-joint composite strip specimen under tensile loading in MTS. As shown in Figures 5-1.11(b) and (c), the joint was made of a high-strength steel double-lap with an upper plate also made of high-strength steel to save the cost of composite and to prevent failure and permanent deformation of the steel plates. The front and side views of the pin-joint set-up with a composite specimen are shown in Figure 5-1.12. Two 1/2"-13 coarse-thread grade 8 hex cap screws with two 1/2"-13 coarse thread grade 8 zinc-finished full hex nuts and four 1/2" USS Rockalloy flat washers were used to hold the steel plates. The steel assembly was then fastened to the composite specimen by a dowel pin through the tight fitting holes in the composite strip and the double-lap plates. The whole joint set up was then placed into the environmental chamber for testing.

The tests were conducted at room, 75ºC, 125ºC –20ºC and –60ºC. For the high and low temperature experiments, the environmental chamber was set first at the design temperature for at least 20 minutes. The composite-steel pin-joint assembly was then mounted to the upper gripper of the MTS in the environmental chamber. Once the specimen was secured in the environmental chamber, additional 20 minutes were waited before closing the lower grip and starting the test. These procedures were taken to avoid thermal mismatching. During the test, the time histories of the applied load and end elongation were recorded through MTS and NI-DAQ systems.

5.1.2.2 Results: As before, the composite joint strips have four different lay-up configurations: $[0^o]_{24\text{-ply}}$, $[0^o_3/90^o_3]_{2S}$, $[+45^o_3/-45^o_3]_{2S}$ and $[0^o_3/+45^o_3/90^o_3/-45^o_3]_S$ with two hole sizes D equal to 1/4" and 1/2". Two sizes of the distance H from the hole center to the edge of the plate were used: 0.75" and 1.5". The recorded applied load *vs* end elongation curves for four different geometries: (a) D = 1/2", H = 0.75", (b) D = 1/2", H = 1.5", (c) D = 1/4", H = 0.75" and (d) D = 1/4", H = 1.5" are shown in Figures 5-1.13 to 5-1.16 for the unidirectional $[0^o]_{24\text{-ply}}$, the cross-ply $[0^o_3/90^o_3]_{2S}$, the angle-ply $[+45^o_3/-45^o_3]_{2S}$ and the quasi-isotropic $[0^o_3/+45^o_3/90^o_3/-45^o_3]_S$ composite pin-joint specimens under tensile loading at various temperatures (room, 75ºC, 125ºC –20ºC and –60ºC, respectively). Although the results are not all consistent, one can observe the general trend that the S2 glass/toughened epoxy composite becomes more "ductile" at high temperature and tends to be more "brittle" at low temperature. As the temperature increases the applied load-end elongation curve becomes more non-linear. Furthermore, the stiffness and applied load at failure decrease while the end elongation at failure increases as the temperature increases. As expected, composite with smaller pin-size has higher stiffness and can endure higher applied load. However, the strain at failure is about the same for same type of composites with different hole sizes. On the other hand, the apparent strength, stiffness and failure strain all increase with increasing H, the distance from the pin hole to the edge of the strip.

Figure 5-1.17 shows two damaged unidirectional $[0^o]_{24\text{-ply}}$ pin-joint specimens with a pin diameter of 0.5" and (a) H =1.5", and (b) H = 0.5". Both specimens have fiber-matrix interfacial cracks along the fiber direction. The failure mode was typical fiber shear out downward from the two extremes of the horizontal diameter of the

pin-hole and upward from the pin-hole contact region. The cross-ply $[0^{o}_{3}/90^{o}_{3}]_{2S}$ pin-joint specimens with a pin diameter of 0.5" and different H values (1.5" and 0.5") are shown in Figure 5-1.18. Figure 5-1.18(a) shows a mixture of failure modes occurred, where fiber shear out, net-tension and bearing failure characteristic were present when the larger H value was used. On the other hand, as shown in Figure 5-1.18(b) only fiber shear out upward from the two extremes of the horizontal diameter of the pin-hole was observed when the smaller H value was chosen.

The damaged angle-ply $[+45^{o}_{3}/-45^{o}_{3}]_{2S}$ pin-joint specimens, the specimens are shown in Figure 5-1.19, where again (a) and (b) are denoted for H = 1.5" and 0.5", respectively. The failure mode for the angle-ply $[+45^{o}_{3}/-45^{o}_{3}]_{2S}$ pin-joint specimens was the due to net-tension induced shear failure, which occurred along the fiber direction. Finally, Figure 5-1.20 shows the damaged quasi-isotropic $[0^{o}_{3}/+45^{o}_{3}/90^{o}_{3}/-45^{o}_{3}]_{S}$ composite pin-joint specimens. Mixed failure mode took place when H =1.5", where fiber shear out, net-tension and bearing were found in Figure 5-1.20(a). When H =0.5", the mixed failure mode was also found in Figure 5-1.20(b) except that bearing failure was absent. Since the bearing effect is also missing in Figure 5-1.18(b), it is believed that the distance from the pin hole to the edge of the strip: H = 0.5" was not long enough for the bearing failure to take place before the catastrophic failure occurred.

(a)

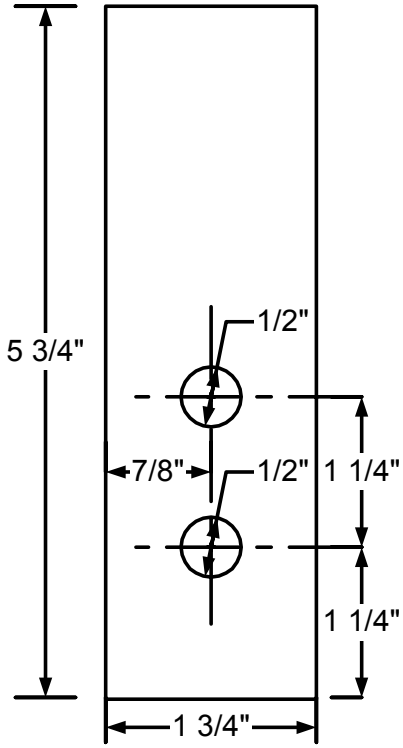

(b)

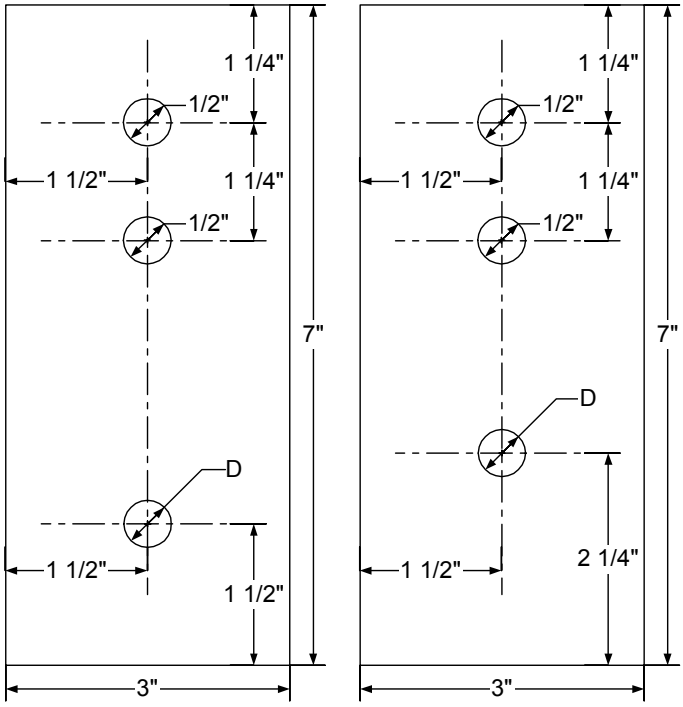

(c)

Figure 5-1.11 (a) A pin-joint composite strip specimen under tensile testing in MTS. (b) The upper steel plate and (c) Two sizes of the double-lap steel plates.

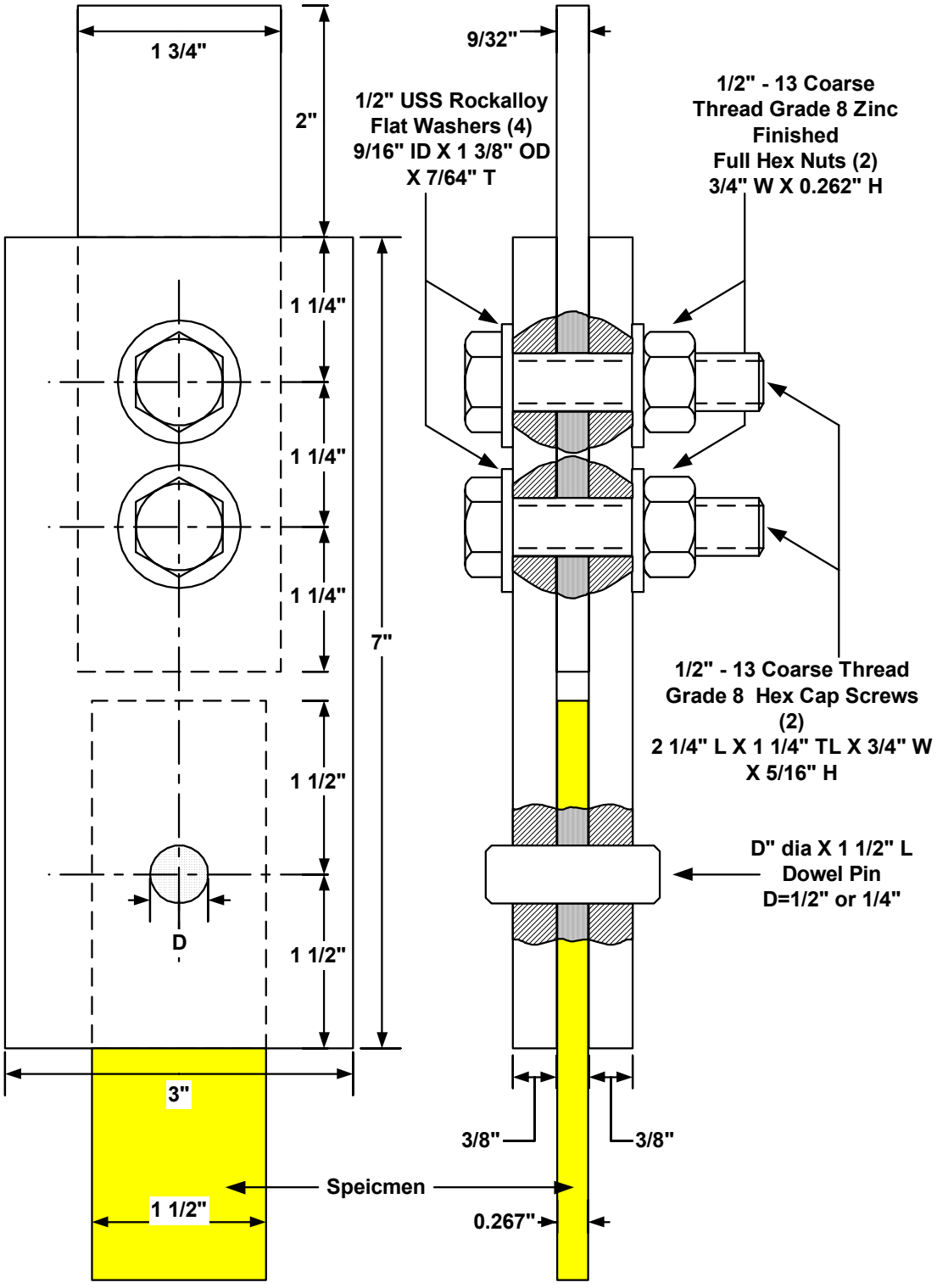

Figure 5-1.12 The front and side views of the pin-joint set-up with a composite strip specimen.

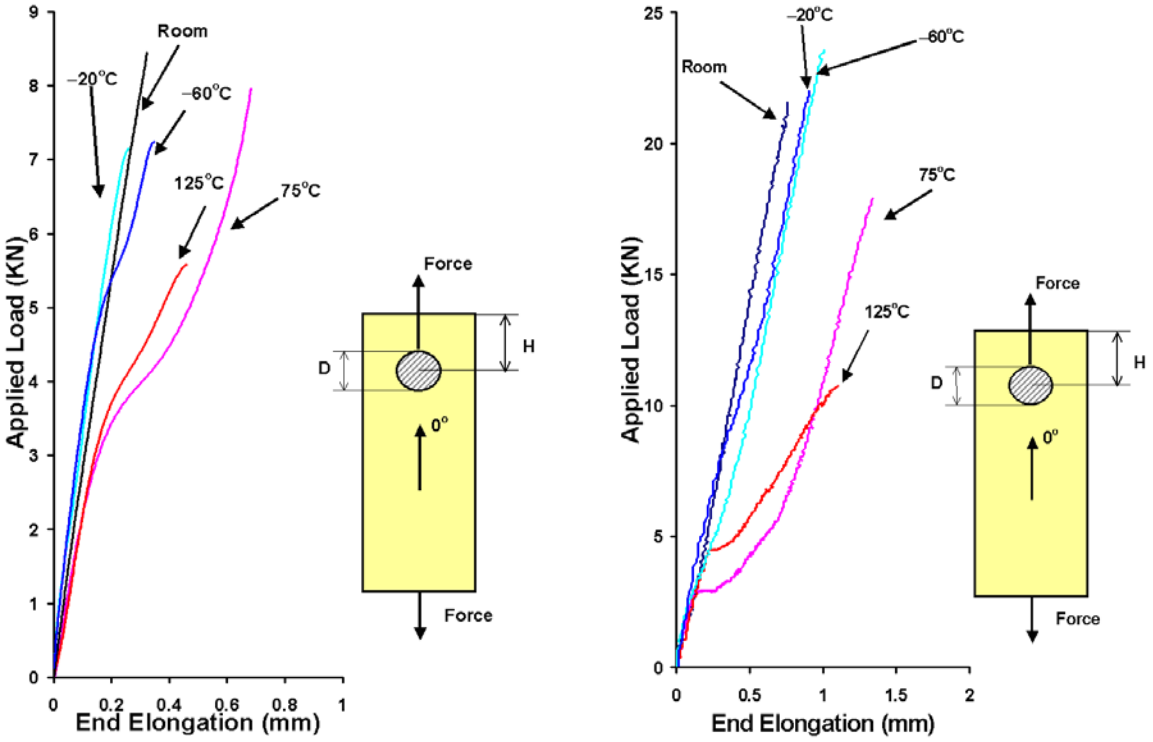

(a) D = 1/2", H = 0.75"

(b) D = 1/2", H = 1.5"

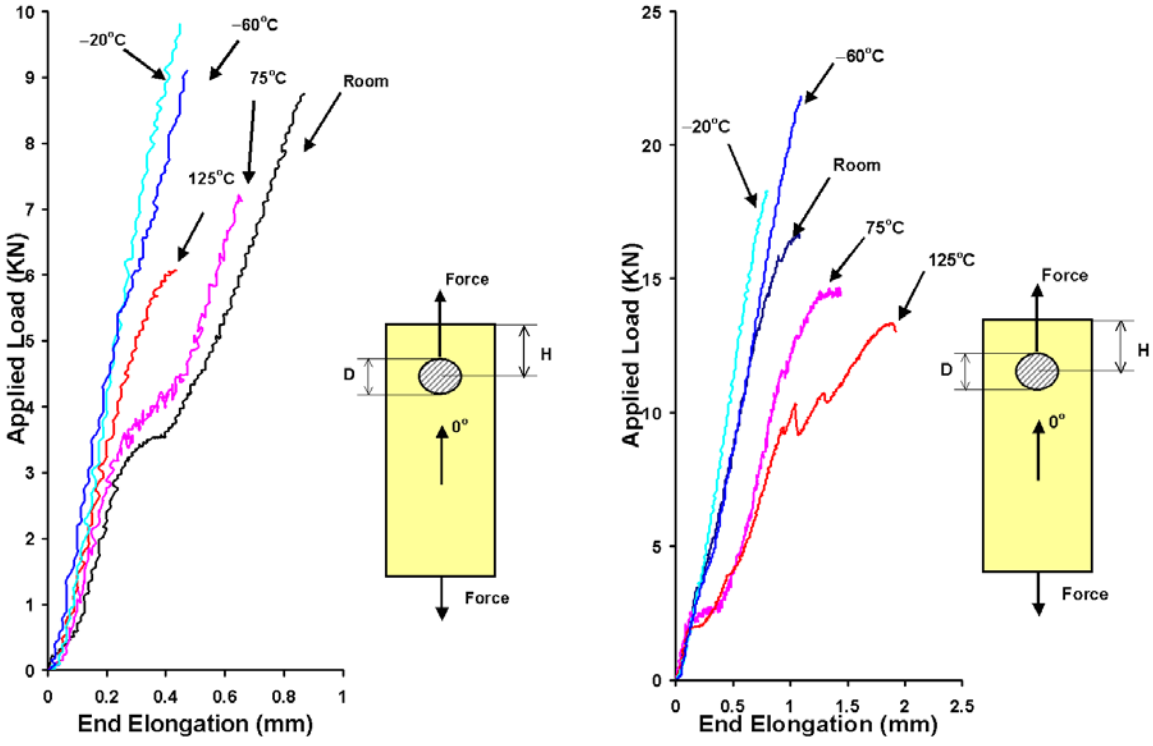

(c) D = 1/4", H = 0.75"

(d) D = 1/4", H = 1.5"

Figure 5-1.13 Applied load *vs* end elongation curves for unidirectional $[0^o]_{24\text{-ply}}$ composite joint specimens under tensile loading at vary temperatures.

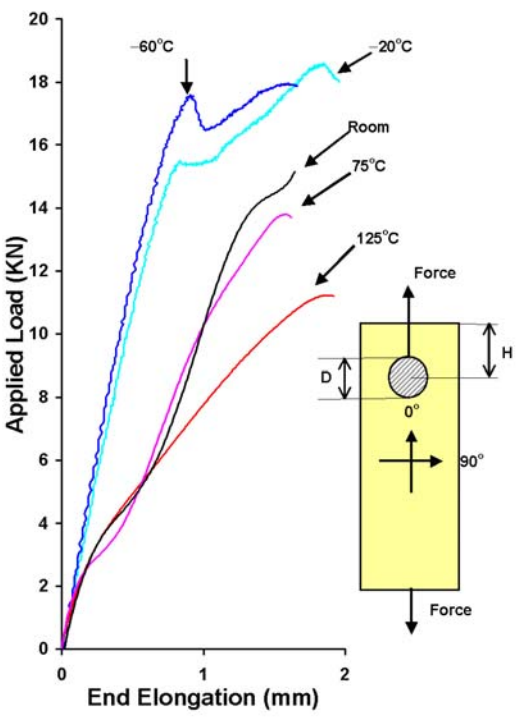

(a) D = 1/2”, H = 0.75”

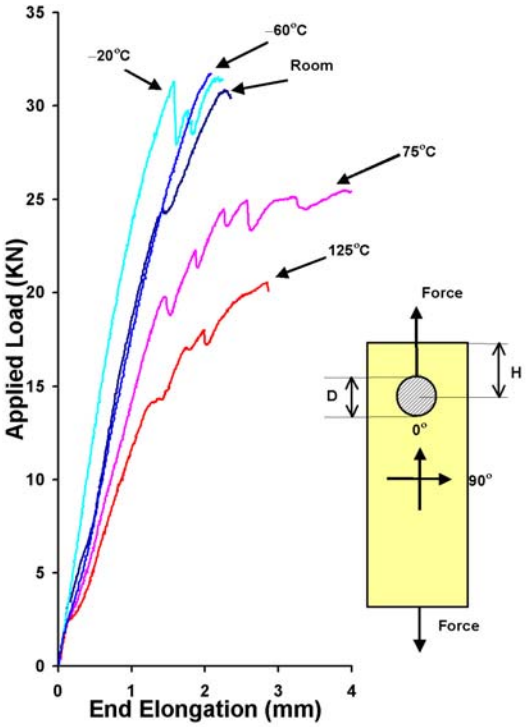

(b) D = 1/2”, H = 1.5”

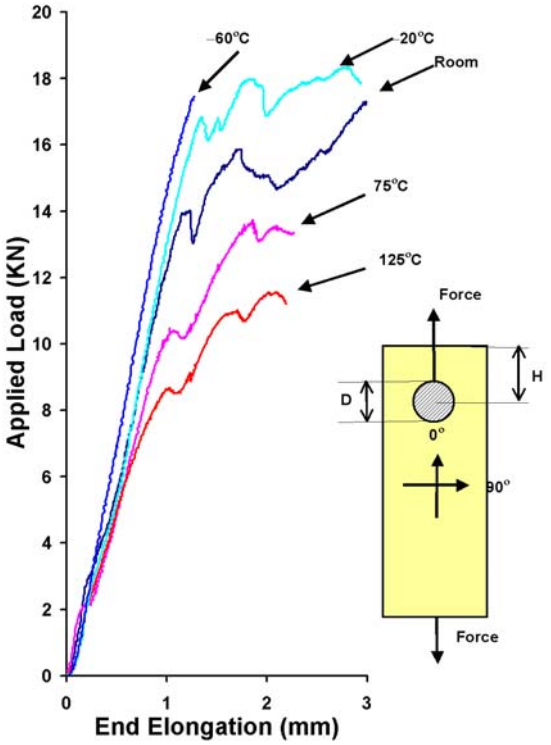

(c) D = 1/4”, H = 0.75”

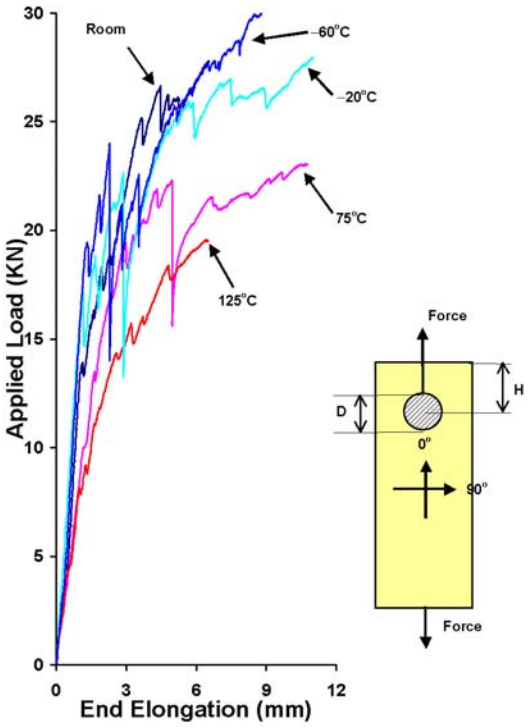

(d) D = 1/4”, H = 1.5”

Figure 5-1.14 Applied load *vs* end elongation curves for cross-ply $[0^{o}_{3}/90^{o}_{3}]_{2S}$ composite joint specimens under tensile loading at vary temperatures.

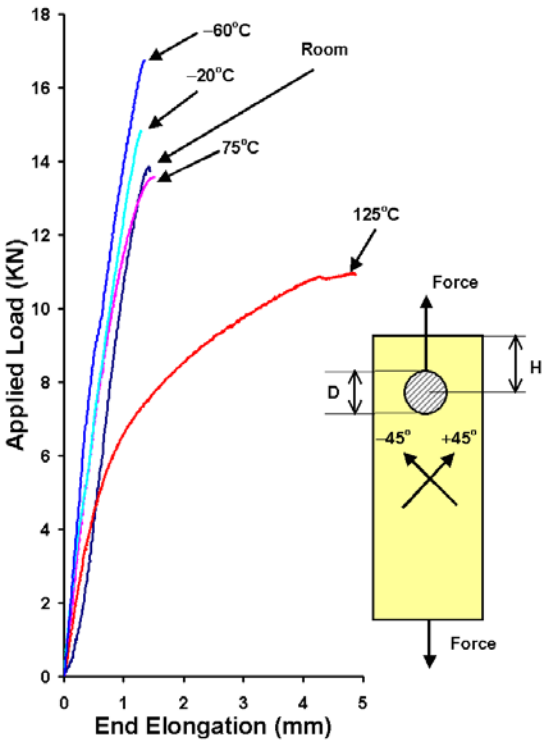

(a) D = 1/2”, H = 0.75”

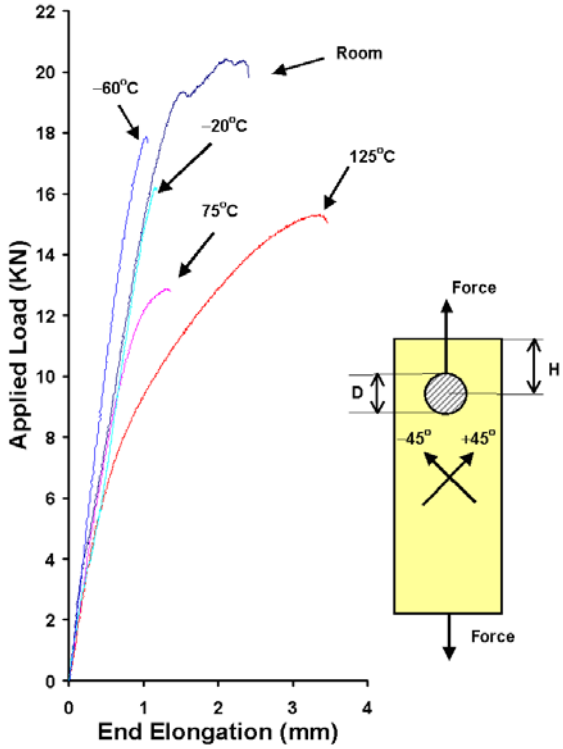

(b) D = 1/2”, H = 1.5”

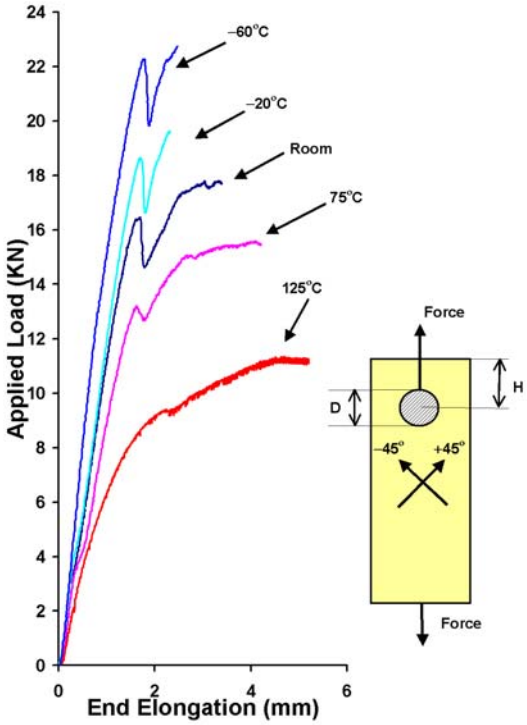

(c) D = 1/4”, H = 0.75”

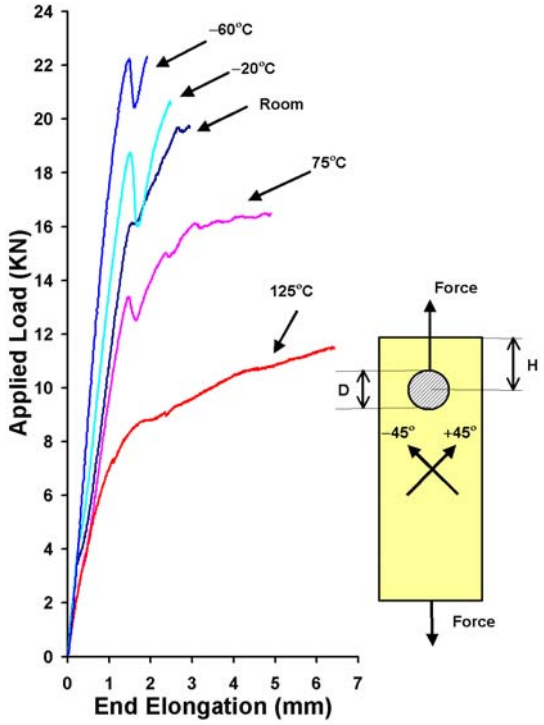

(d) D = 1/4”, H = 1.5”

Figure 5-1.15 Applied load *vs* end elongation curves for angle-ply $[+45°_3/–45°_3]_{2S}$ composite joint specimens under tensile loading at vary temperatures.

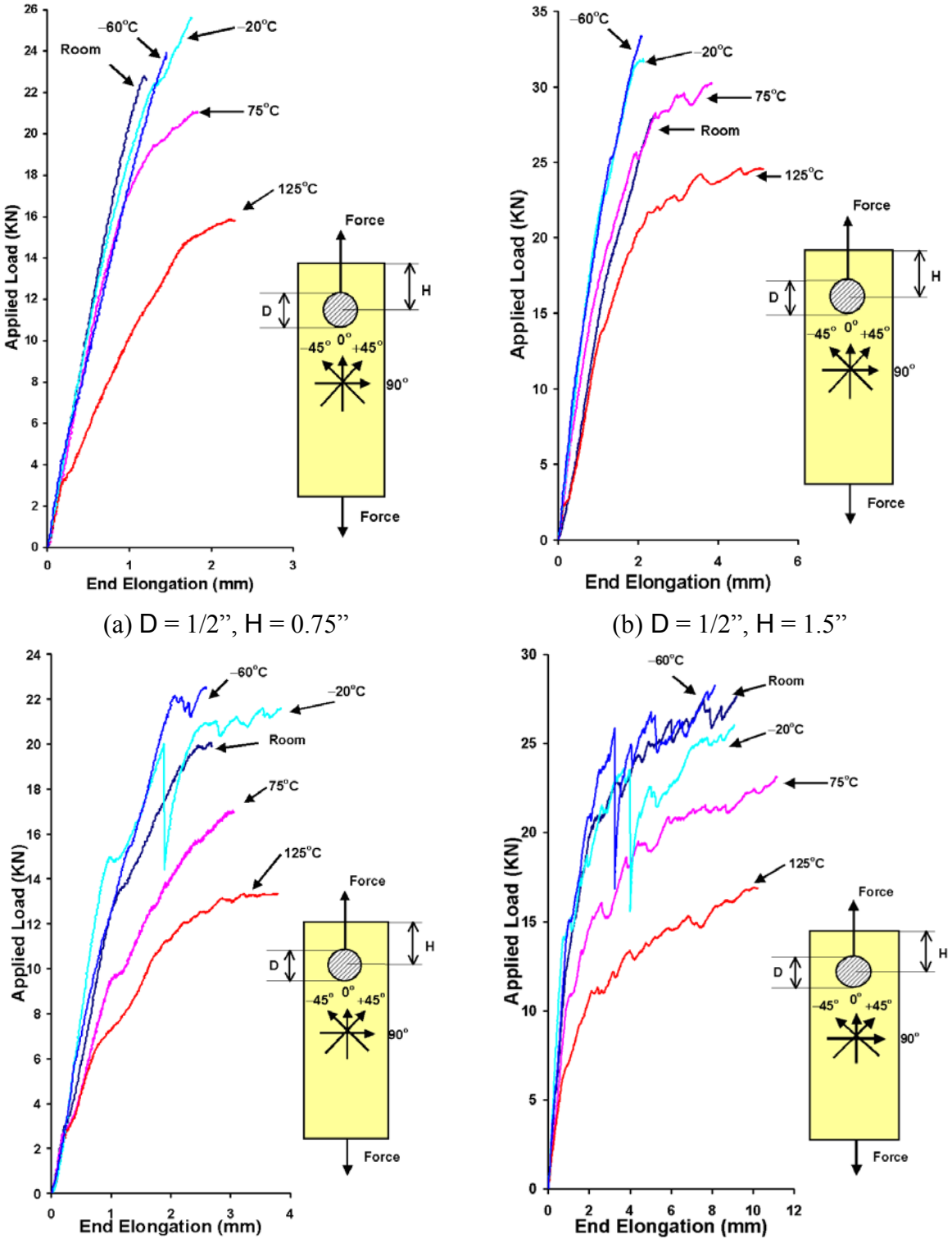

(a) D = 1/2”, H = 0.75”

(b) D = 1/2”, H = 1.5”

(c) D = 1/4”, H = 0.75”

(d) D = 1/4”, H = 1.5”

Figure 5-1.16 Applied load *vs* end elongation curves for quasi-isotropic $[0°_3/+45°_3/90°_3/-45°_3]_S$ composite joint specimens under tensile loading at vary temperatures.

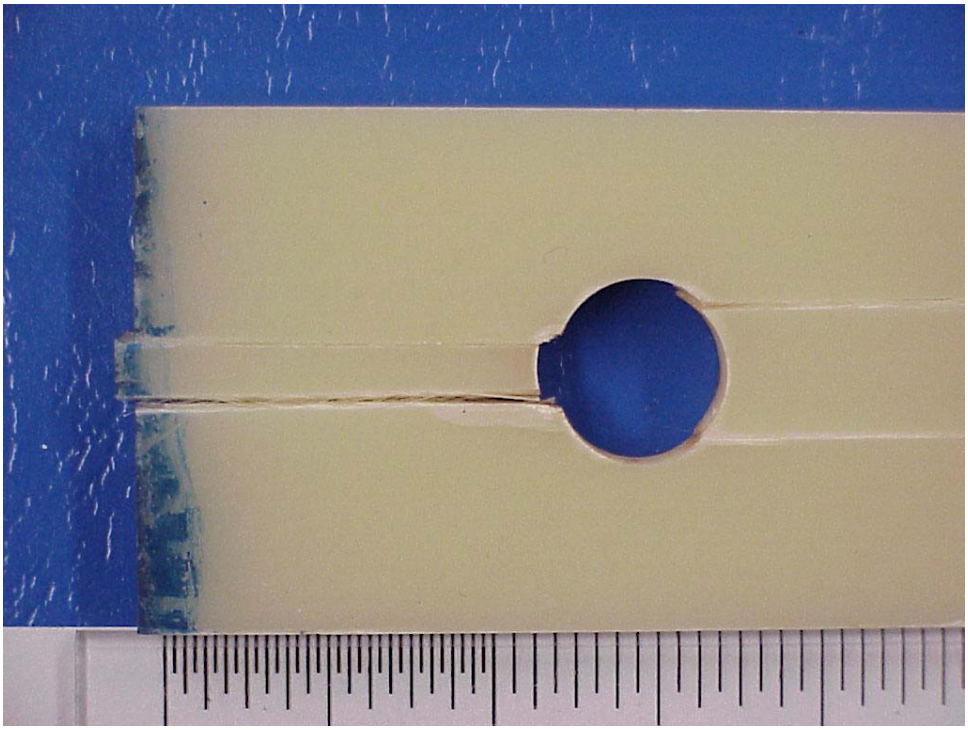

(a)

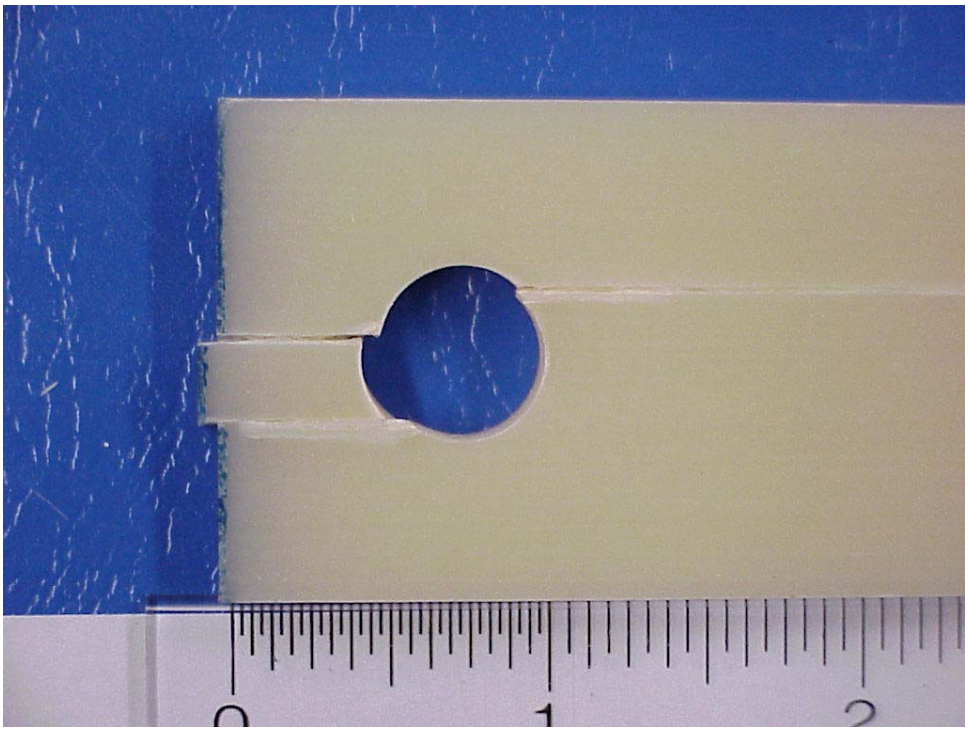

(b)

Figure 5-1.17 Damaged unidirectional $[0^o]_{24\text{-ply}}$ pin-joint specimens with a pin diameter of 0.5": (a) H =1.5" and (b) H = 0.75".

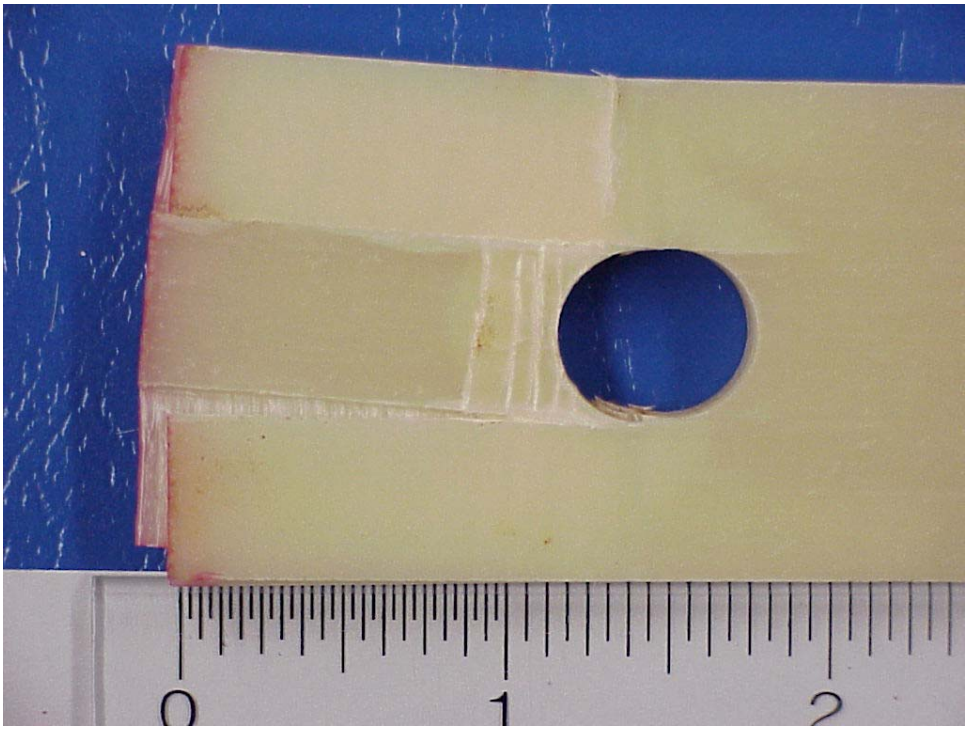

(a)

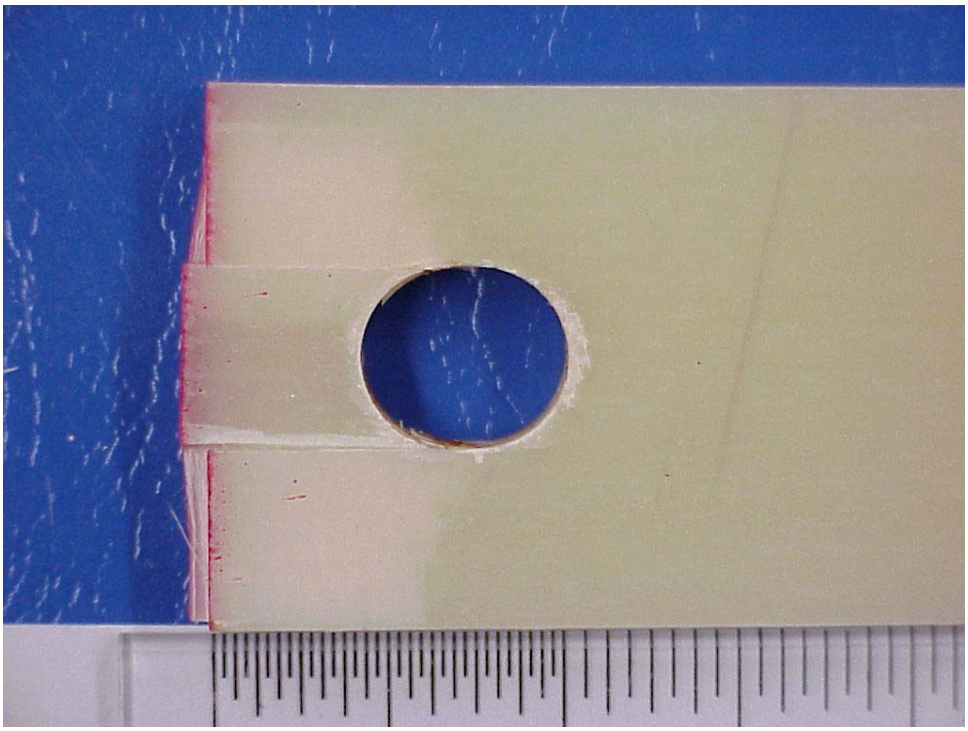

(b)

Figure 5-1.18 Damaged cross-ply $[0^{o}_{3}/90^{o}_{3}]_{2S}$ pin-joint specimens with a pin diameter of 0.5": (a) H =1.5" and (b) H = 0.75".

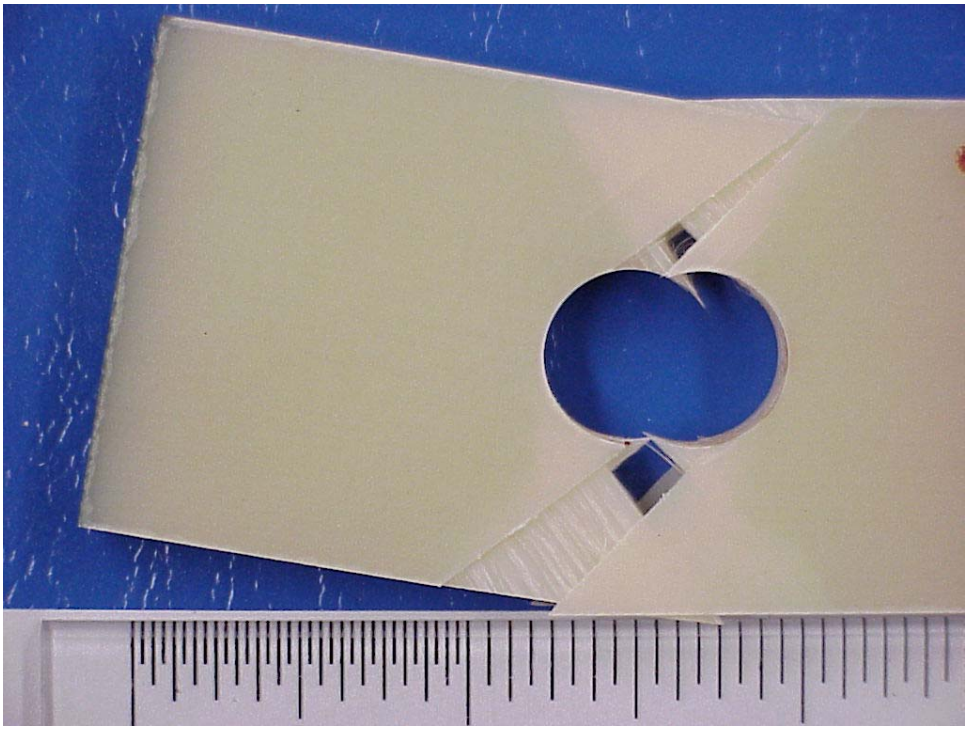

(a)

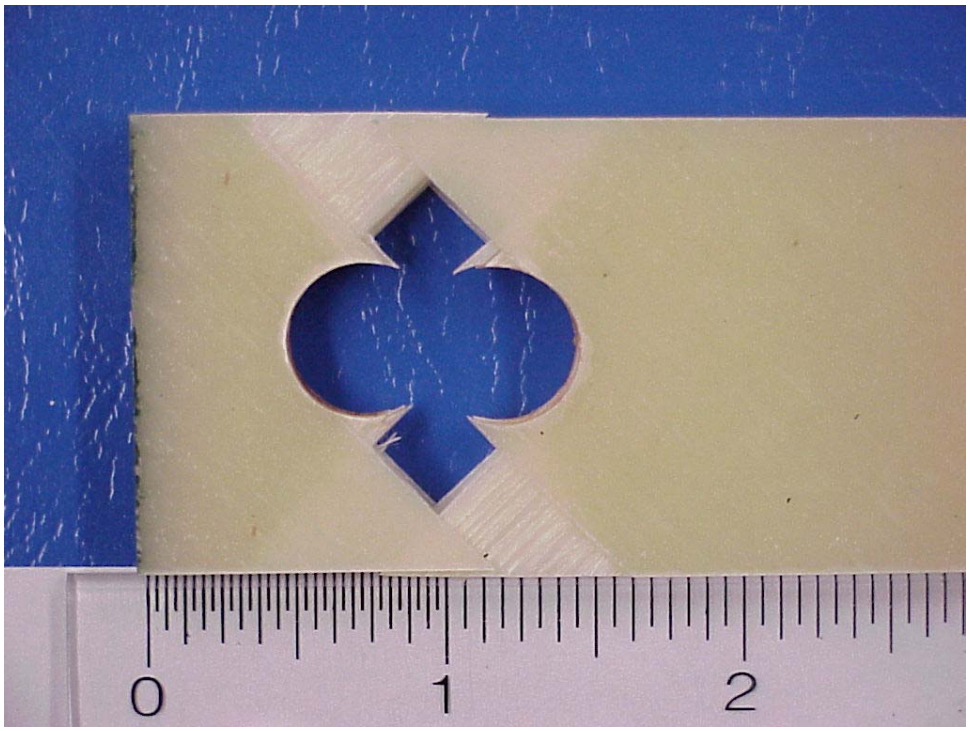

(b)

Figure 5-1.19 Damaged angle-ply $[+45^{o}_{3}/-45^{o}_{3}]_{2S}$ pin-joint specimens with a pin diameter of 0.5": (a) H =1.5" and (b) H = 0.75".

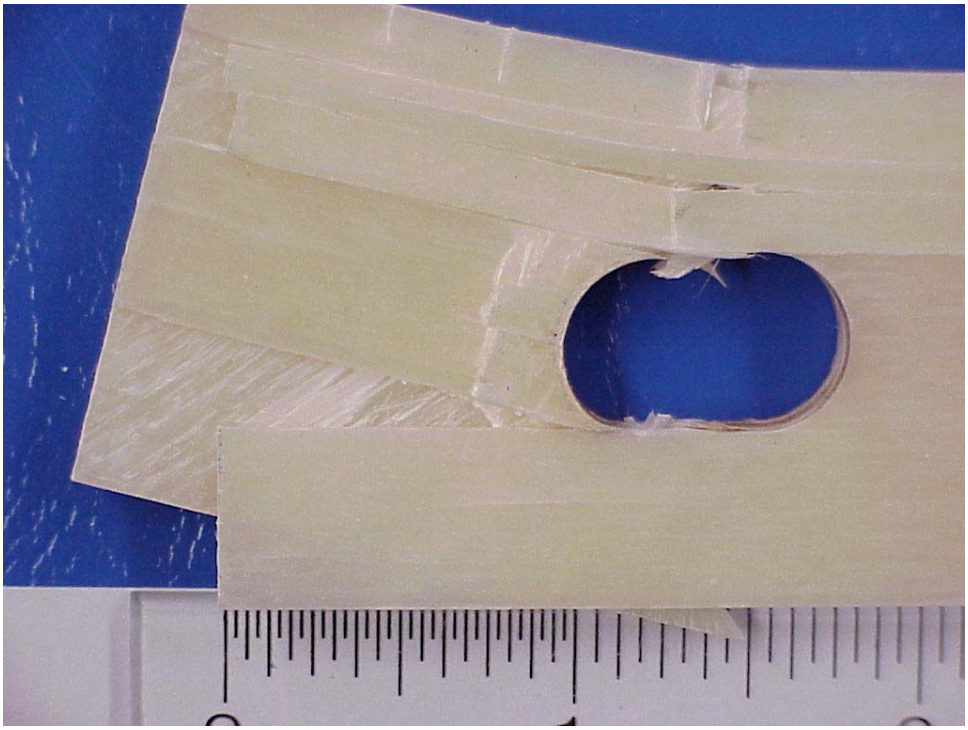

(a)

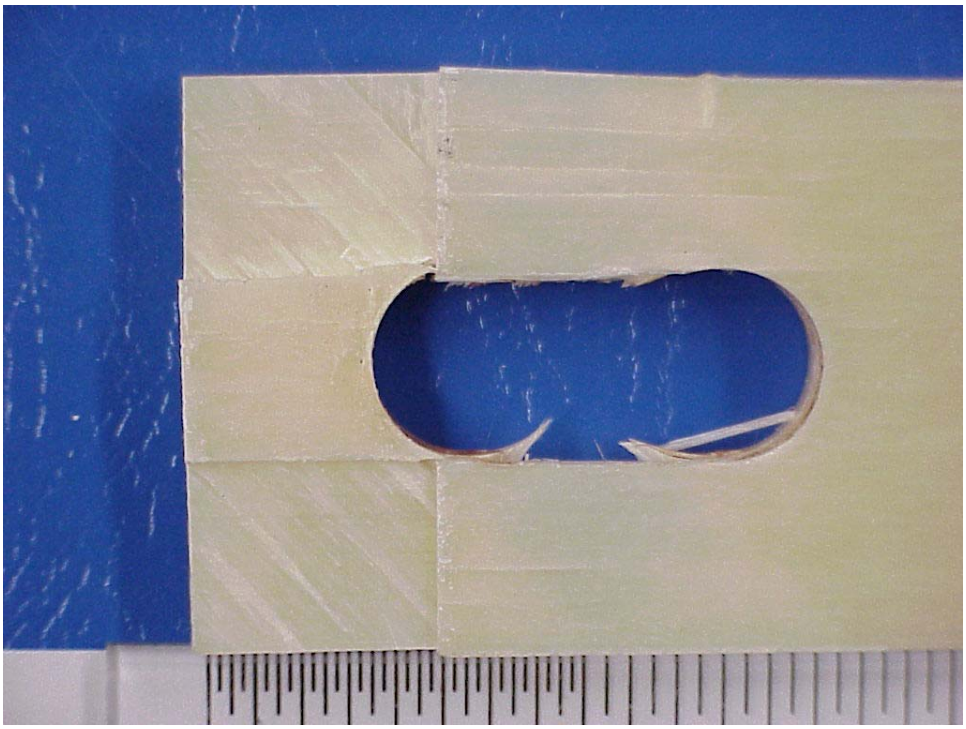

(b)

Figure 5-1.20 Damaged quasi-isotropic $[0^{o}_{3}/+45^{o}_{3}/90^{o}_{3}/-45^{o}_{3}]_{S}$ pin-joint specimens with a pin diameter of 0.5": (a) H =1.5" and (b) H = 0.75".

5.2 Finite Element Studies of Composite Strips with a Center Hole

In order to explain the observed progressive failure of S2 glass/toughened epoxy composite strips with a center hole, a finite element model with a nonlinear elastic orthotropic material with finite failure strains embedded in the commercially available finite element code ANSYS was adopted (Linear Orthotropic with Multilinear Kinematic). Figure 5-2.1 shows the layered-composite finite element mesh (Element Type 1, Solid Layered 191) used in this study for the angle-ply $[+45^{\circ}_3/-45^{\circ}_3]_{2S}$ and quasi-isotropic $[0^{\circ}_3/+45^{\circ}_3/90^{\circ}_3/-45^{\circ}_3]_S$ specimens. Here the composite lay-up configuration was specified along the out-of-plane direction. Due to the anti-symmetric nature of fiber orientations in these two configurations, a full finite element model, as shown in Figure 5-2.1, is needed. On the other hand, only a quarter model was needed for the unidirectional $[0^{\circ}]_{24\text{-ply}}$ and the cross-ply $[0^{\circ}_3/90^{\circ}_3]_{2S}$ due to the symmetric nature of their fiber orientations.

The tensile-induced damaged stress-strain curves for dog-bone specimens tested in Chapter 4 were used as the sources of the proposed constitutive laws. Four consistent tests were first conducted for three lay-up configurations: the longitudinal $[0^{\circ}]_{24\text{-ply}}$, the transverse $[90^{\circ}]_{24\text{-ply}}$ and the angle-ply $[+45^{\circ}_3/-45^{\circ}_3]_{2S}$ since their characteristic failure modes are fiber breakage, transverse matrix cracking and shear failure, respectively. Three average curves were then abstracted from the test results to form the bases of the nonlinear elastic orthotropic material model with finite failure strains. For instance, Figure 5-2.2(a) shows the nonlinear stress-strain curve with a failure strain of 4% for the longitudinal $[0^{\circ}]_{24\text{-ply}}$ composite, whose dominant failure mode is fiber breakage. On the other hand, the almost linear stress-strain curve with a failure strain of 0.35%, as shown

in Figure 5-2.2(b), is for the transverse $[90°]_{24\text{-ply}}$ composite, which always fails in transverse matrix cracking. Finally, shear failure is the main failure mode in $[+45°_3/-45°_3]_{2S}$ composites and results in the very ductile-like stress-strain curve with a failure strain at 7%, as shown in Figure 5-2.2(c).

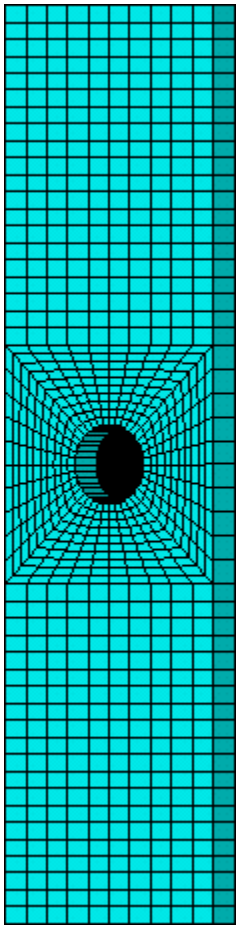

Figure 5-2.1 Layered-composite finite element mesh for the quasi-isotropic and angle-ply composites.

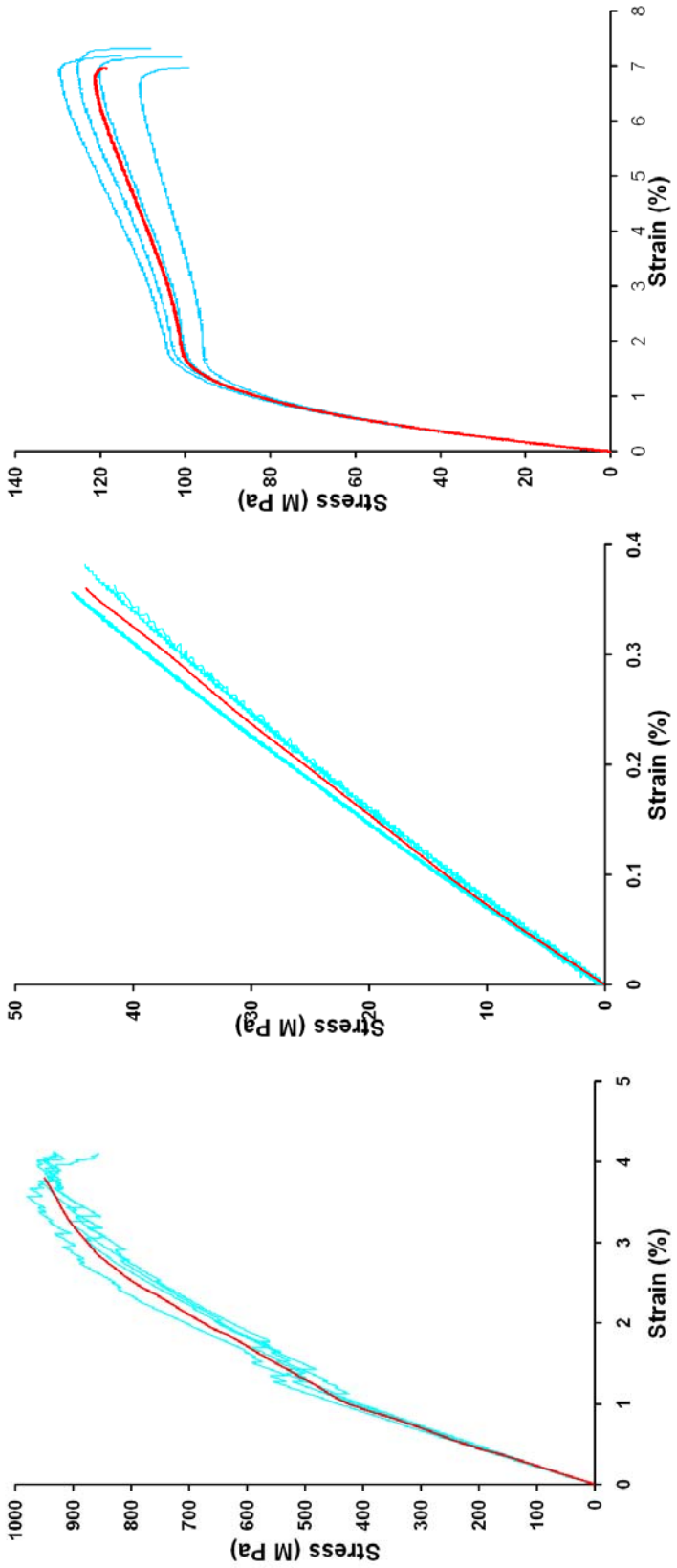

Figure 5-2.2 Stress-strain curves for the bog-bone specimens under tension for (a) $[0^\circ]_{24\text{-ply}}$: fiber breakage, (b) $[90^\circ]_{24\text{-ply}}$: transverse matrix cracking and (c) $[+45^\circ 3/-45^\circ 3]_{2S}$: shear failure.

For each simulation, linear elastic orthotropic finite element analysis with a constant displacement input along the upper edge of the finite element mesh, shown in Figure 5-2.1 was first conducted. The ratios $\frac{\varepsilon_1}{\varepsilon_{1,\text{init}}}$, $\frac{\varepsilon_2}{\varepsilon_{2,\text{init}}}$ and $\frac{\gamma_{12}}{\gamma_{12,\text{init}}}$ at each layer within an element were computed. Here ε_1, ε_2 and γ_{12} are strains along the fiber direction, transverse to the fiber direction, and of the in-plane shear, respectively; while $\varepsilon_{1,\text{init}}$ (0.5%), $\varepsilon_{2,\ \text{init}}$ (0.01%) and $\gamma_{12,\text{init}}$ (0.125%) are the initial failure strains along those directions, respectively, which were determined from the tensile tests of dog-bone specimens. That is, if the strain along a direction at a layer in an element is larger than the initial failure strain, the corresponding damage (e.g., fiber breakage, transverse matrix cracking or shear failure) occurs and the stress-strain curve governing that direction becomes nonlinear, as depicted in Figure 5-2.2.

In short, the linear analysis will allow us to determine the minimum level of the applied strain to cause the initial damage and the corresponding failure mode. The applied displacement was then scaled to cause this initial failure and a nonlinear finite element analysis based on the proposed nonlinear elastic orthotropic material model was executed. It should be pointed out that because of the limitation by ANSYS, each layer in an element could only fail in one mode. That is, mixed-mode failure, though possible physically, could not be simulated by this approach. For instance, when the predicted longitudinal strain ε_1 in a layer of an element exceeded the experimentally-determined initial failure longitudinal strain $\varepsilon_{1,\text{init}}$, that layer in that element was considered to have failed in fiber breakage and the corresponding nonlinear curve, Figure 5-2.2(a), was applied whereas the material properties along the transverse and shear directions were

assumed to be linear at that location since mixed-mode failure was not allowed in this model. Thus, the failure mode of a layer in an element could was independent from other layers in the same element as well as from the same layer in neighboring elements.

The applied displacement was increased incrementally until the finite element analysis was aborted by ANSYS due to numerical instability, which was caused by excessive softening in tangential stiffness resulting from severe damage of the specimen. During this process, damage pattern in each layer was recorded; the resultant force along the upper edge was computed. Together with the applied displacement, they were converted into stress-stain curve.

Figure 5-2.3 shows the comparison between the theoretical results and experimental data for four different configurations of a composite strip with a 0.5" diameter center hole tested under uniaxial tension at room temperature. The predicted stress-strain curve for $[0°]_{24\text{-ply}}$ configuration in Figure 5-2.3(a) matches very well up to about 1% of strain out of a total strain of 3.5%. As for the $[0°_3/90°_3]_{2S}$ case in Figure 5-2.3(b), the theoretical result predicts the experimental data very well up to about 1.5% of strain out of a total strain of 4.5%. As for $[+45º_3/–45º_3]_{2S}$ specimens, Figure 5-2.3(c) shows excellent agreement of the theoretical finding over almost the entire experimental results. The ANSYS simulated stress-strain curve for $[0°_3/+45º_3/90°_3/–45º_3]_S$ case matches the experimental results up to more than 50% of the experimental range. Overall, the finite element results indicate that the proposed failure model matches the experimental data quite well. It should be noted that in general, the finite element curves are stiffer than experimental data. This can be explained easily since the model does not allow mixed-mode failure and delamination even though both failure mechanisms had

been detected in experiment; especially more toward the end of a test when the proposed finite element model did not match the experimental data well.

The same scheme to predict the progress failure was also applied for $[+45^{o}_{3}/-45^{o}_{3}]_{2S}$ angle-ply composite strips with center holes of different sizes (1/2", 3/8", 1/4" and 1/8") tested at various temperatures (room, 75°C and 125°C). As shown in Figures 5-2.4 to 5-2.6, regardless the hole size, finite element simulations predict the experimental results quite well for the angle-ply composite tested at room temperature, 75°C and 125°C so long as numerical instability does not occur during ANSYS calculations. It seems that the larger the center hole size, the better the agreement with the experimental data.

To illustrate the progressive damage of the composite strips with a center hole under uniaxial loading, the damage patterns predicted by finite element simulations are plotted Figures 5-2.7 to 5-2.10. Because of symmetry, only a quarter of the element meshes was shown for the unidirectional, the cross-ply and the angle-ply strip. On the other hand, a completed element mesh was used for the quasi-isotropic strips due to its non-symmetric nature. Figure 5-2.7 shows the predicted progressive damage of a $[0°]_{24\text{-ply}}$ specimen with a center hole of D =1/2" under different uniaxial strain levels: 0.34%, 0.41%, 0.48%, 0.55%, 0.62% and 0.68% tested at room temperature. A series of damage elements mark with X, which represents shear failure, were shown. As expected, the initial damage took place on the hole boundary due to stress concentration. Shear failure occurred first due to the high strength nature of the fibers. Such an initial damage was captured photographically in Figure 5-1.3. As the applied strain was increased, more

shear failure occurred to form a series of parallel lines along the fiber (also loading) direction, similar to the fashion shown in the fractographs of Figure 5-1.3.

Figure 5-2.8 shows the predicted progressive damage of a $[0°_3/90°_3]_{2S}$ specimen with a center hole of D =1/2" under different strain levels tested at room temperature. Here the symbols for various failure modes are ● = fiber breakage, □ = transverse matrix cracking and X = shear failure. A quarter of the specimens were showed for both the 0° and the 90° layer. At strain equal to 0.07%, 90° layers had already been damaged by transverse matrix cracking near the edge of the hole. On the other hand, 0° layers remained intact until the strain was increased to 0.27%, where shear failure occurred at the edge of the hole. At this moment, almost all the elements in the 90° layers had already failed. However, the specimen remained attached with the 0° layers carried all the loads. As the applied strain was increased, more shear failure in the 0° layers along the fiber direction. Finally, at the strain equal to 0.68%, all 0° layers failed. In comparison to the fractographs in Figure 5-1.4, the simulated progressive damage patterns match the experimental record quite well.

As for the angle-ply strips with a center hole, the progressive failure is shown in Figure 5-2.9, which indicates that the initial damage of both transverse matrix cracking and shear failure appeared near the edge of the hole at a strain level of 0.21%. As the strain level increased, both types of damage emanated from the hole at about 45°. The damage eventually spread throughout the layers and caused catastrophic failure a strain level of 0.68%. The predicted damage evolution is quite consistent with the fractographs shown in Figure 5-1.6.

Finally, Figure 5-2.10 shows the predicted room-temperature progressive damage in a $[0°_3/+45°_3/90°_3/–45°_3]_S$ strip specimen with a center hole of D =1/2" under different strain levels. At the strain level equal to 0.14%, both the 90° and 45° layers failed at the edge of the hole. As shown in the figure, the damage mode in the 90° layers is transverse matrix cracking whereas the damage in 45° layers is shear failure. When the strain was increased to 0.27%, the 90° layers had already been damaged severely with transverse matrix cracking. At that strain level, the 45° layers had developed both transverse matrix cracking and shear failure. On the other hand, the 0° layers was not damaged until the strain level reached 0.41%, when a single element at the edge of the hole in that layer failed in shear. At that strain level, the 45° layers also had failed completely; leaving the 0° layers to carry the load. Finally, at the strain equal to 0.96%, all the layers failed. When compared to the fractographs shown in Figure 5-1.7, the simulated progressive damage predicts the experimental result reasonably well.

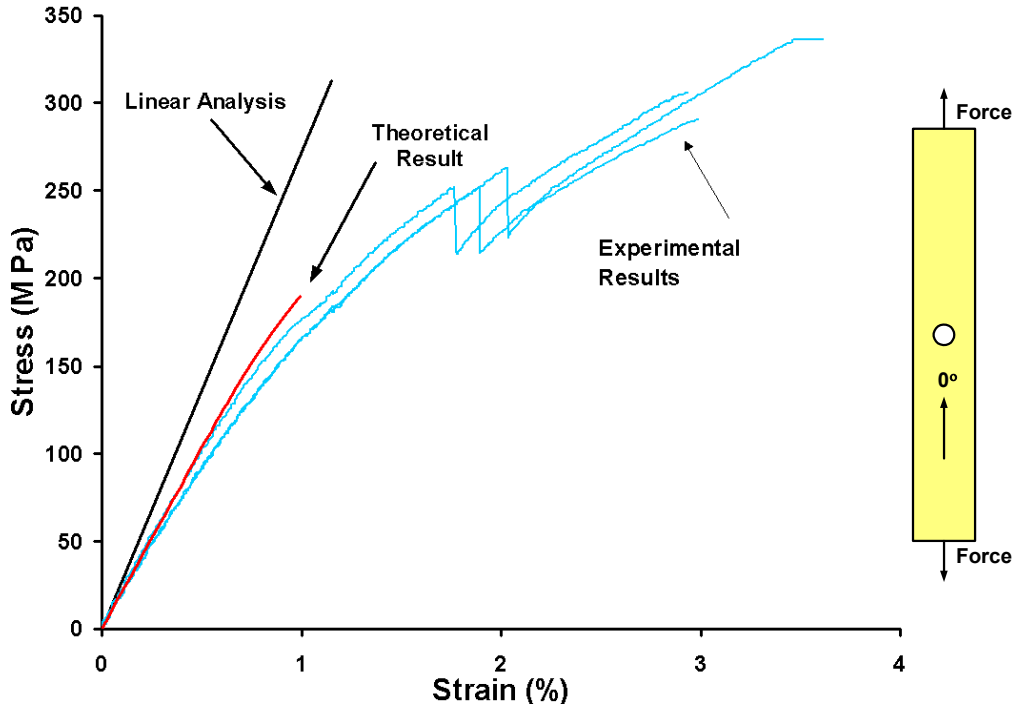

(a) $[0°]_{24\text{-ply}}$

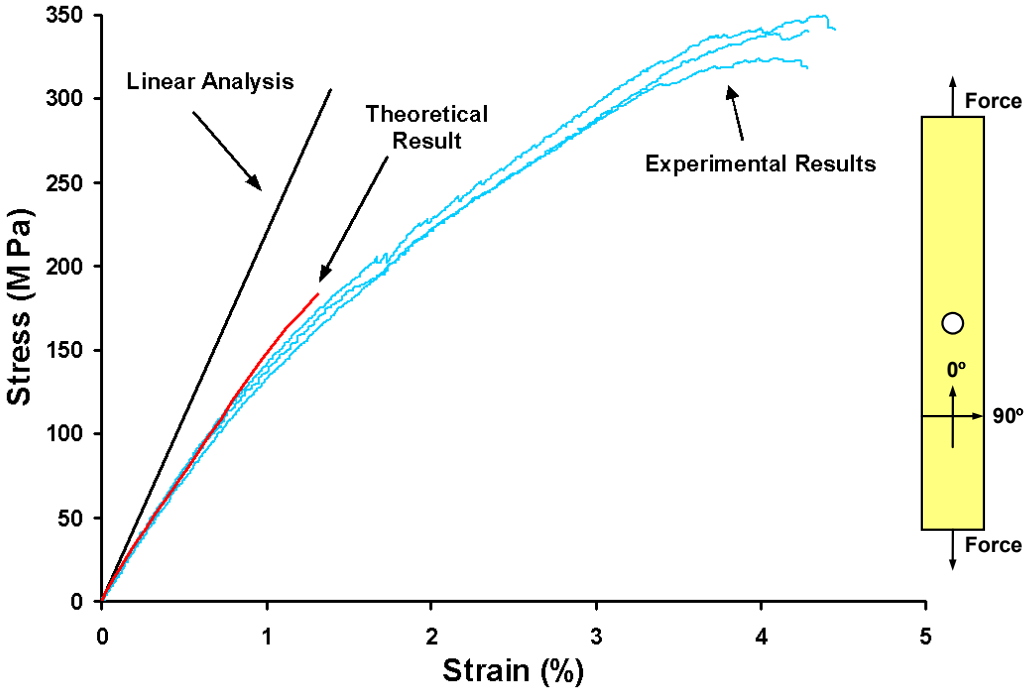

(b) $[0°_3/90°_3]_{2S}$

Figure 5-2.3 Comparison between the theoretical predictions and experimental data for (a) $[0°]_{24\text{-ply}}$, (b) $[0°_3/90°_3]_{2S}$, (c) $[+45°_3/–45°_3]_{2S}$ and (d) $[0°_3/+45°_3/90°_3/–45°_3]_S$ composite strips with a center hole (D=0.5") tested at room temperature.

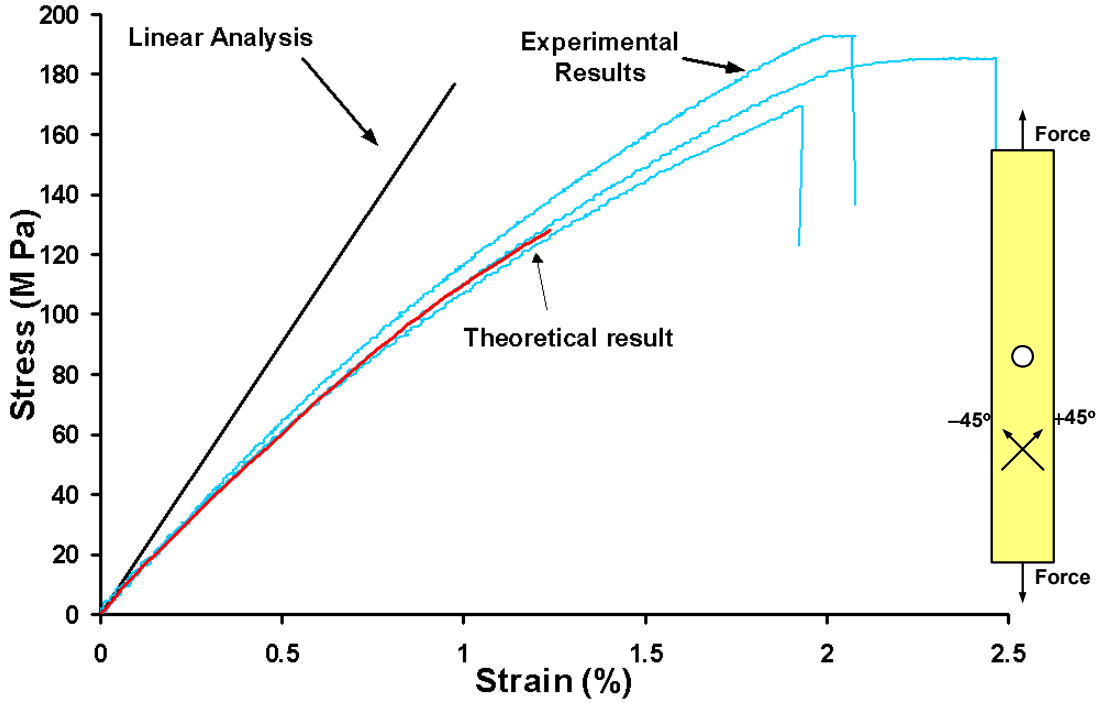

(c) $[+45°_3/-45°_3]_{2S}$

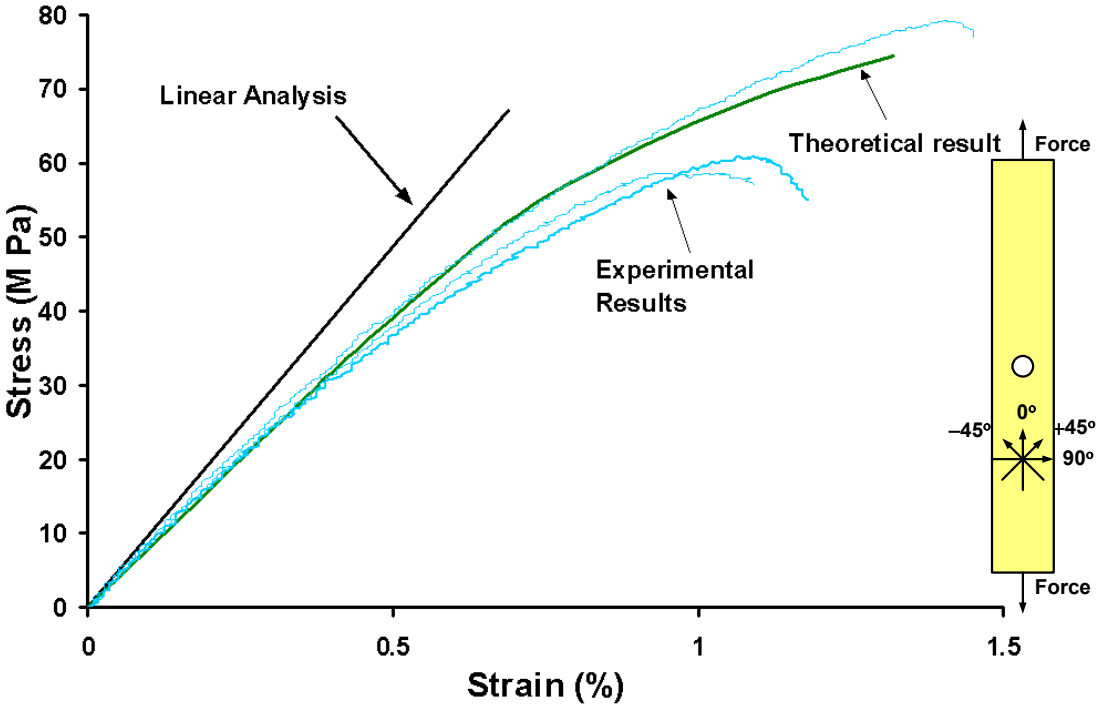

(d) $[0°_3/+45°_3/90°_3/-45°_3]_S$

Figure 5-2.3 (continued)

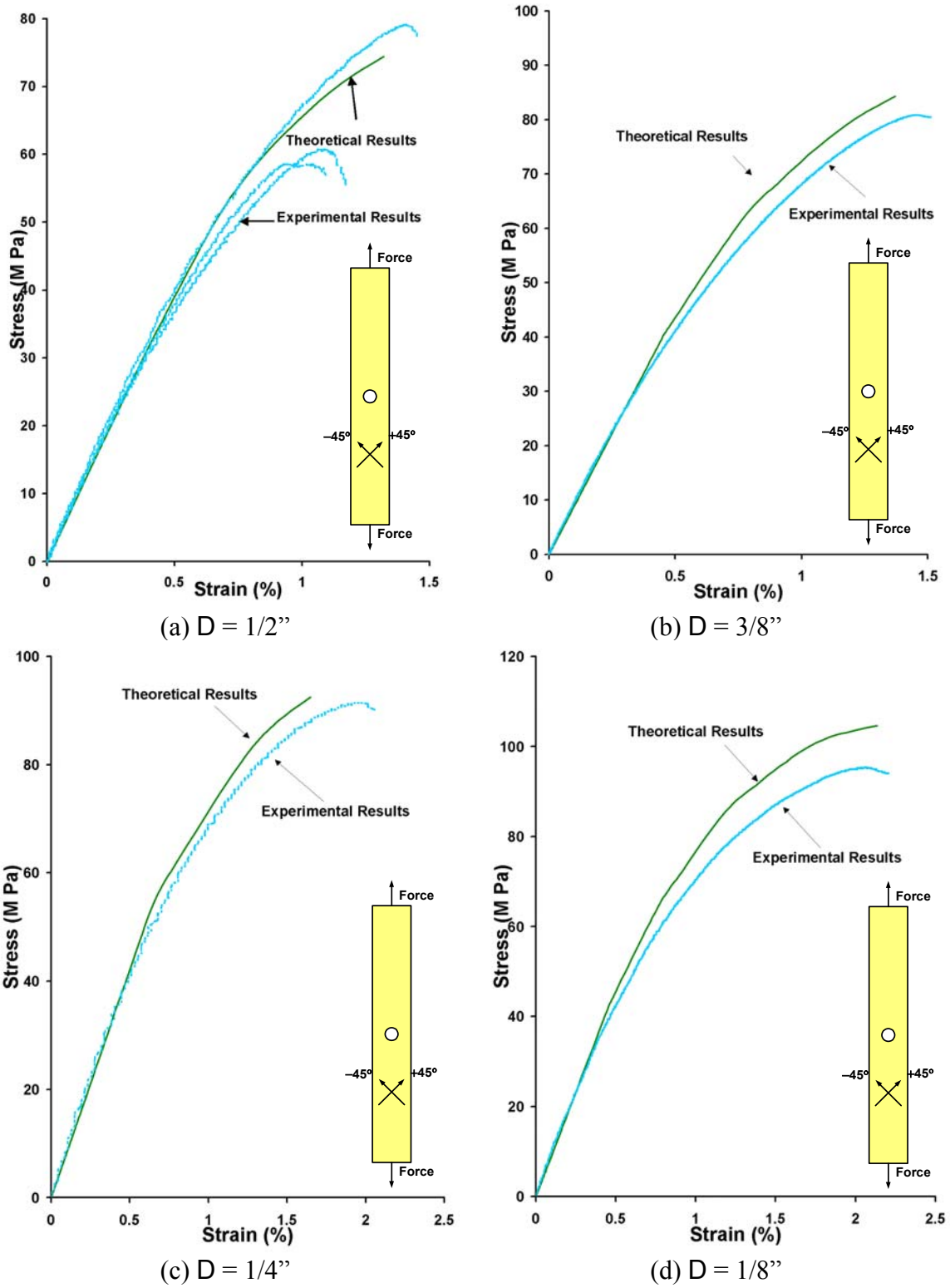

(a) D = 1/2”

(b) D = 3/8”

(c) D = 1/4”

(d) D = 1/8”

Figure 5-2.4 Comparisons between theoretical predictions and experimental results for $[+45^{\circ}_3/-45^{\circ}_3]_{2S}$ angle-ply composite strips with different center-hole sizes tested at room temperature.

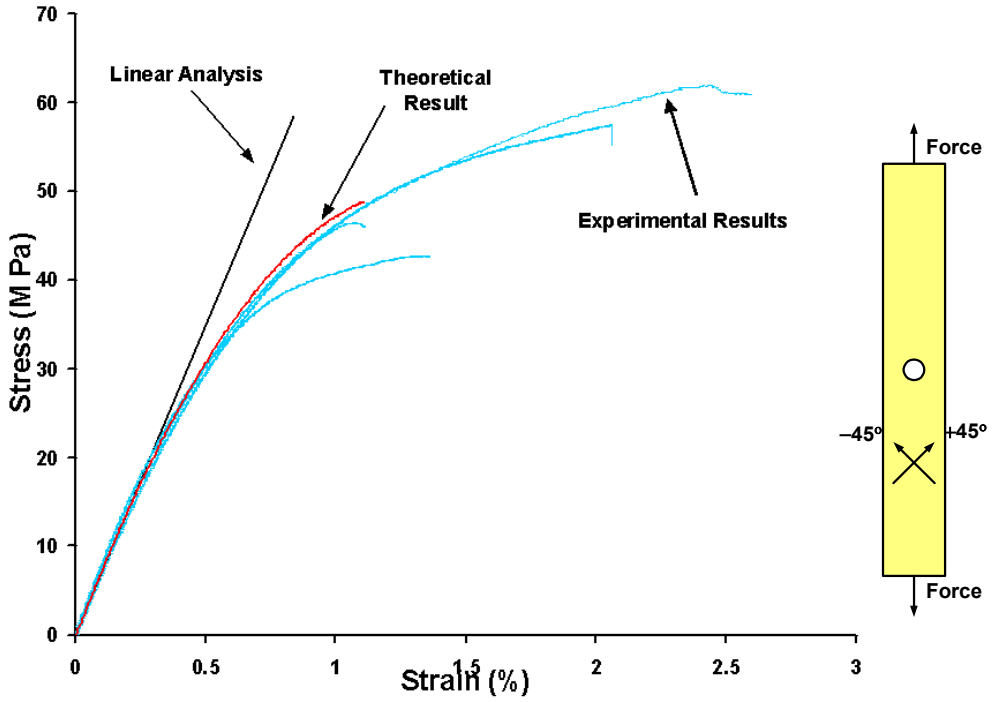

(a) D = 1/2"

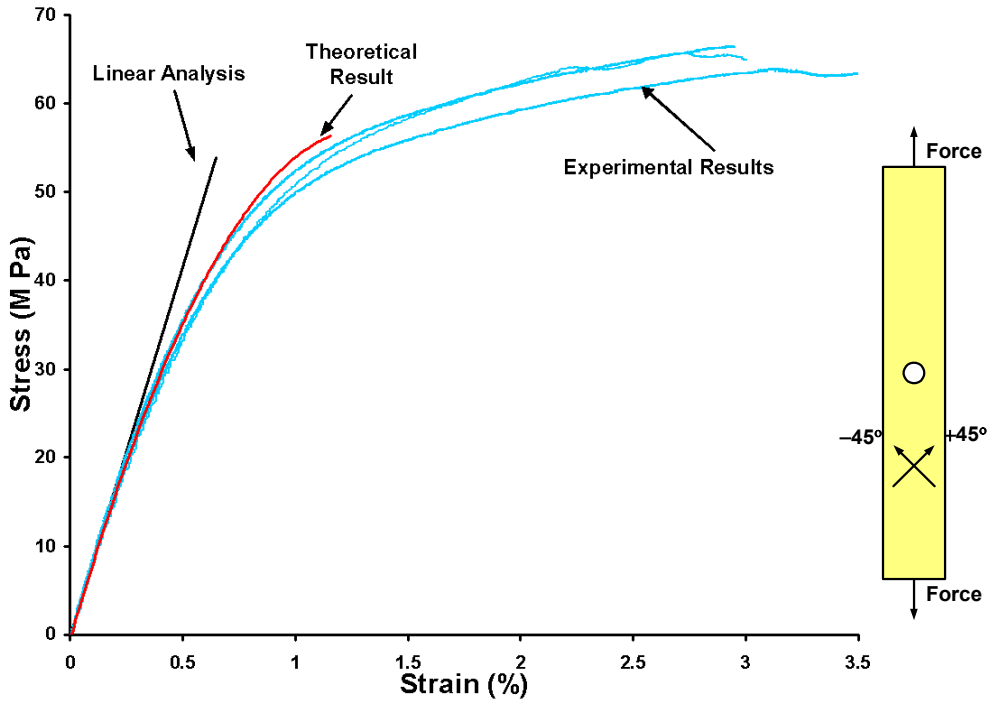

(b) D = 3/8”

Figure 5-2.5 Comparisons between theoretical predictions and experimental results for $[+45^{\circ}_3/-45^{\circ}_3]_{2S}$ angle-ply composite strips with different center-hole sizes tested at 75°C.

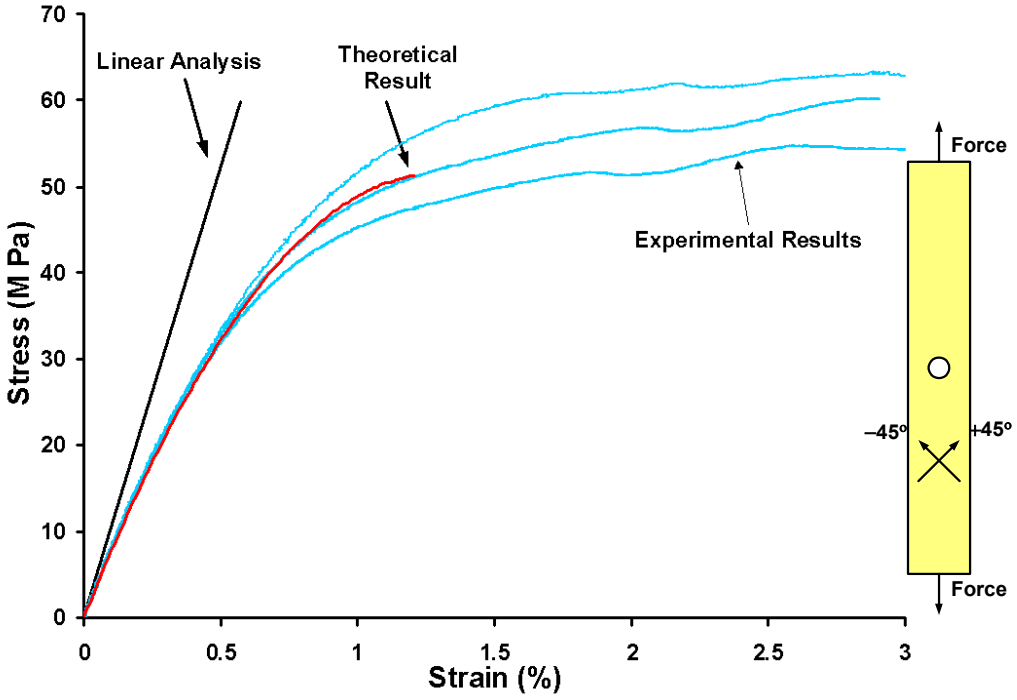

(c) D = 1/4"

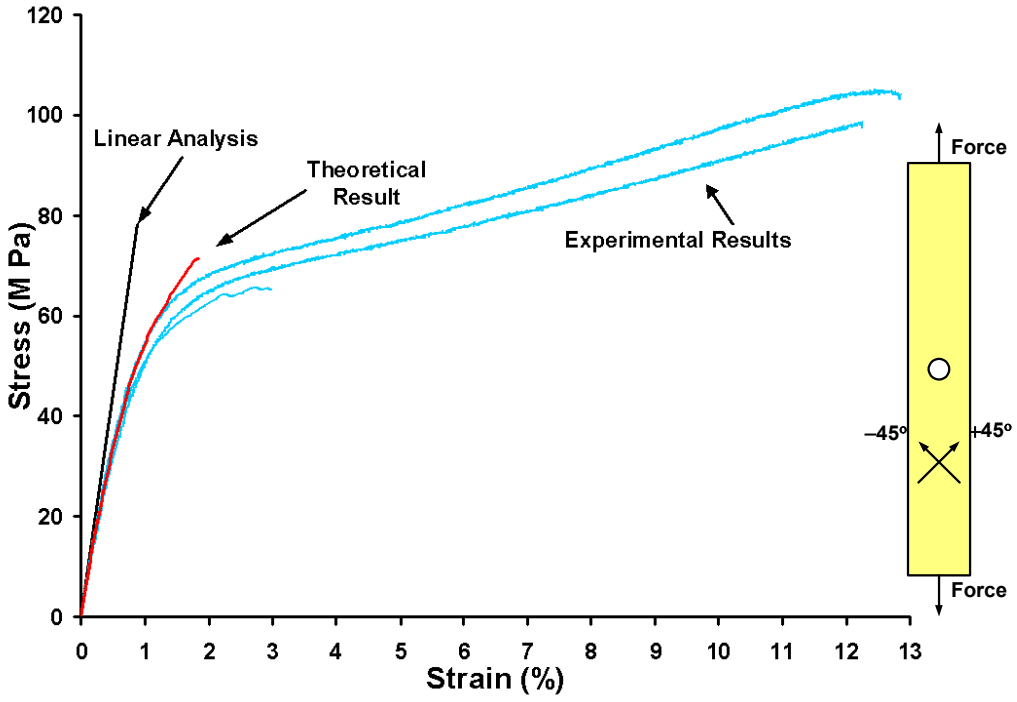

(d) D = 1/8”

Figure 5-2.5 (continued)

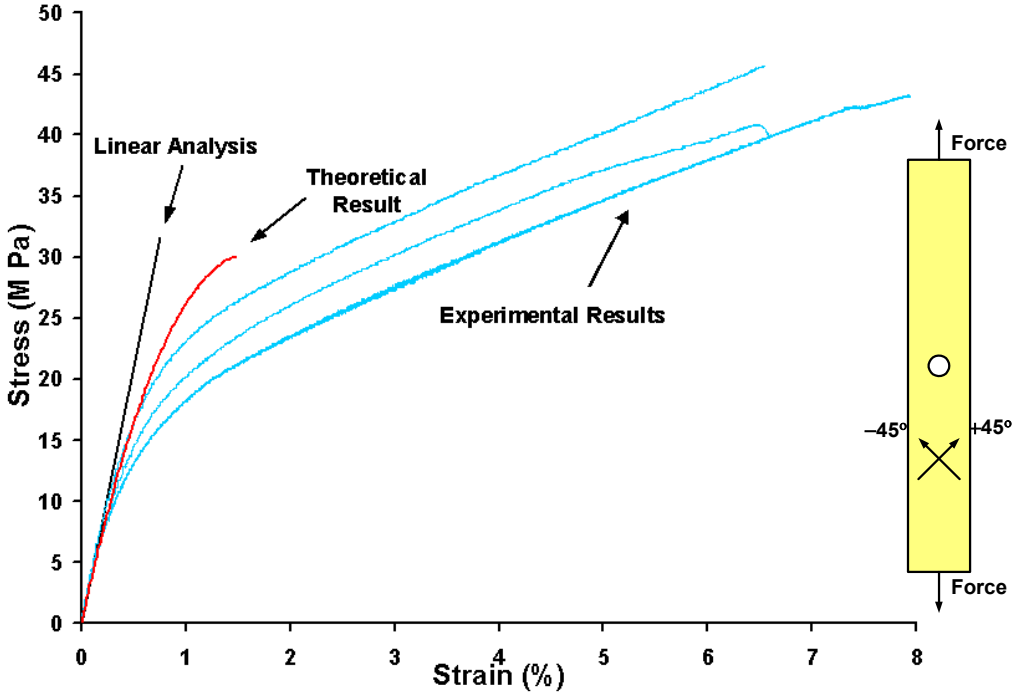

(a) D = 1/2"

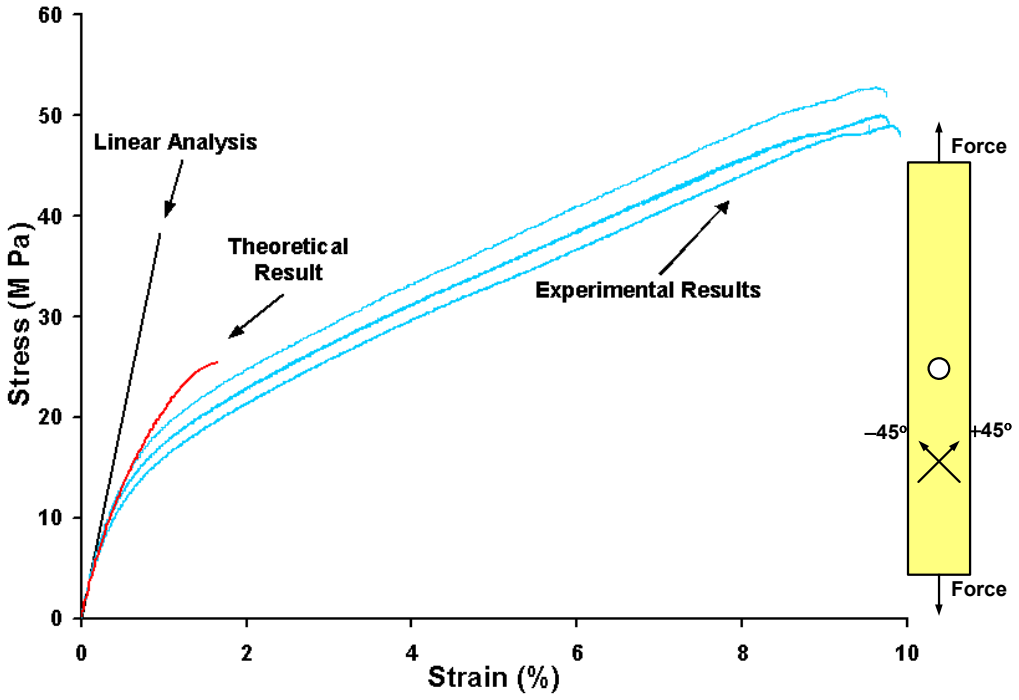

(b) D = 3/8"

Figure 5-2.6 Comparisons between theoretical predictions and experimental results for $[+45^{o}_{3}/-45^{o}_{3}]_{2S}$ angle-ply composite strips with different center-hole sizes tested at 125°C.

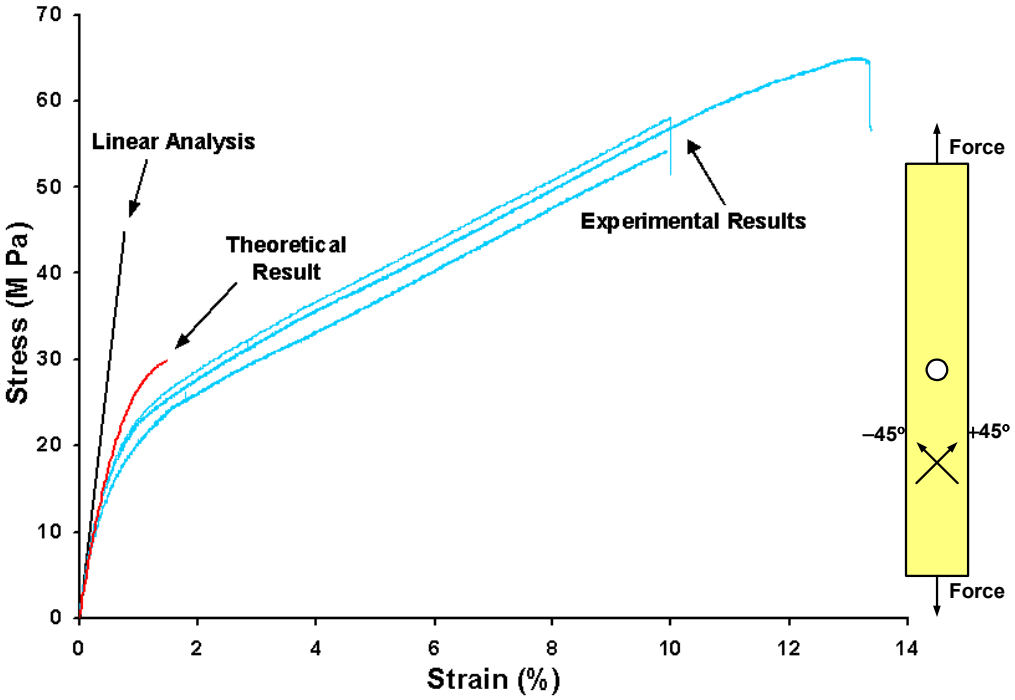

(c) D = 1/4"

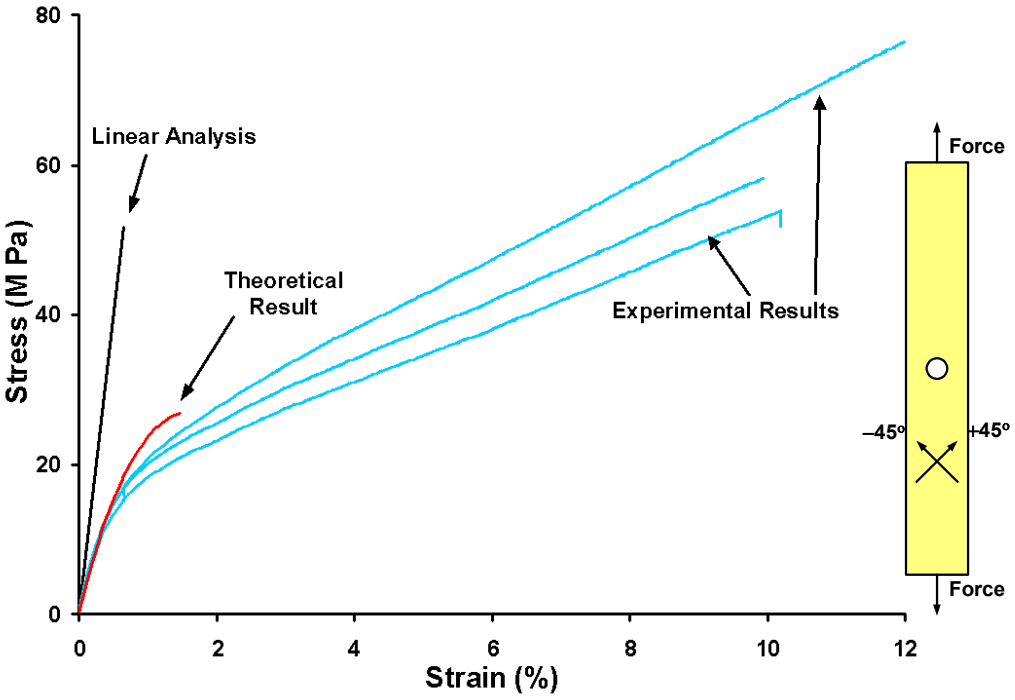

(d) D = 1/8”

Figure 5-2.6 (continued)

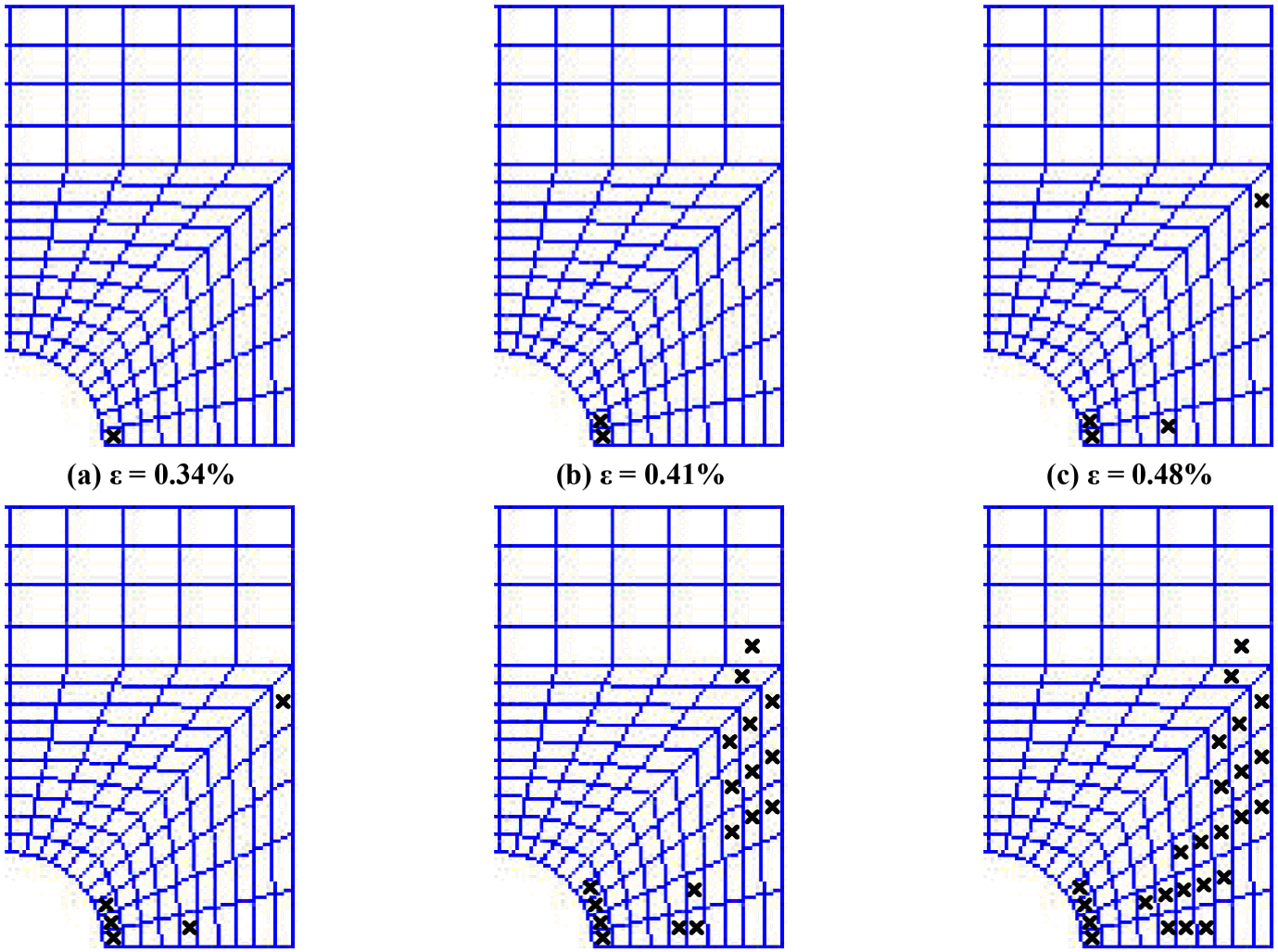

Figure 5-2.7 Predicted progressive damage of a $[0°]_{24\text{-ply}}$ center-hole strip with D =1/2" under different strain levels tested at room temperature (X = shear failure).

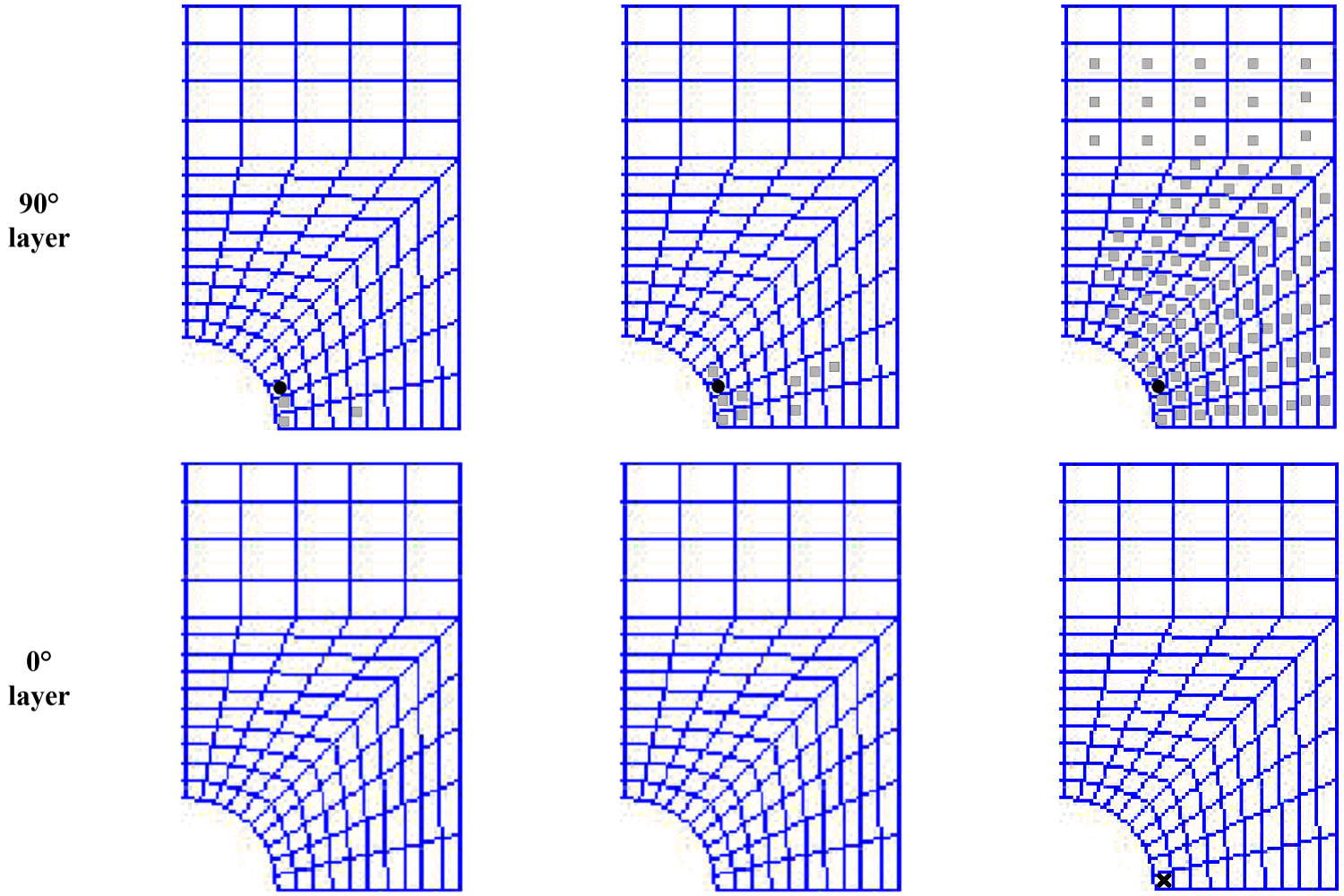

Figure 5-2.8 Predicted progressive damage of a $[0°_3/90°_3]_{2S}$ center-hole strip with D =1/2" under different strain levels tested at room temperature (● = fiber breakage, ▢ = transverse matrix failure and X = shear failure).

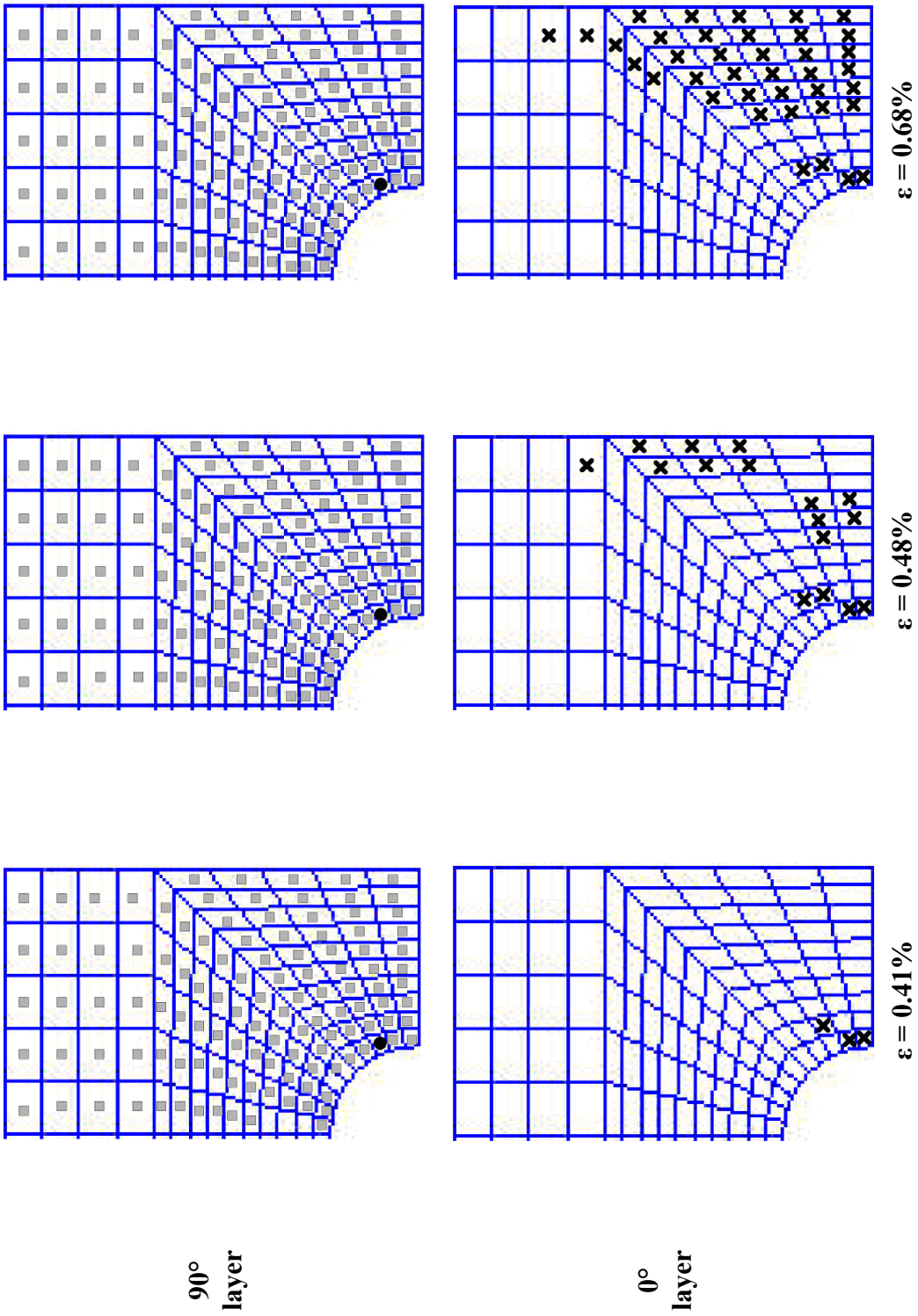

Figure 5-2.8 (continued)

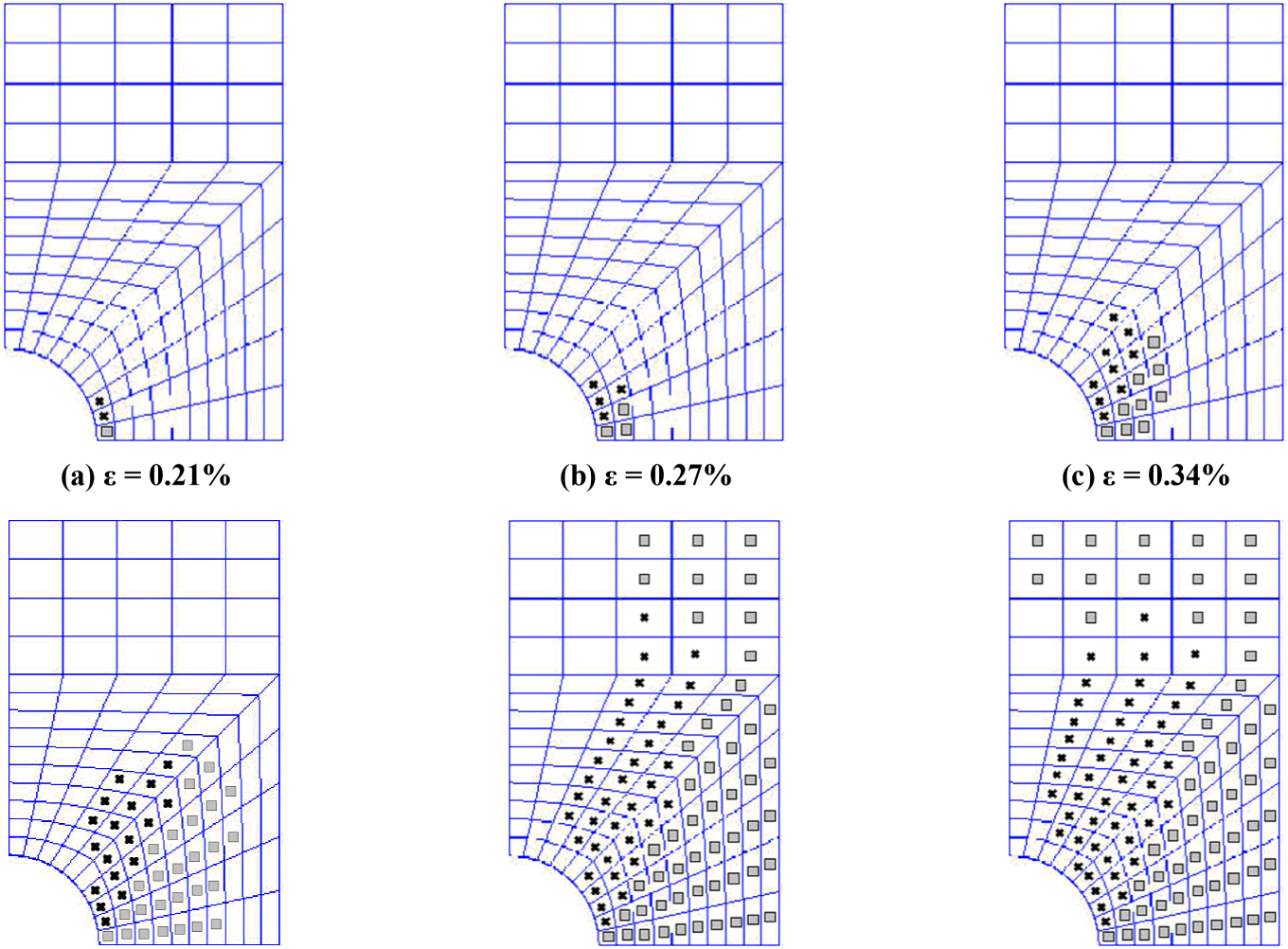

(a) ε = 0.21%　(b) ε = 0.27%　(c) ε = 0.34%

(d) ε = 0.41%　(e) ε = 0.55%　(f) ε = 0.68%

Figure 5-2.9 Predicted progressive damage of a $[+45^{o}_{3}/-45^{o}_{3}]_{2S}$ center-hole strip with D =1/2" under different strain levels tested at room temperature (□ = transverse matrix failure and X = shear failure).

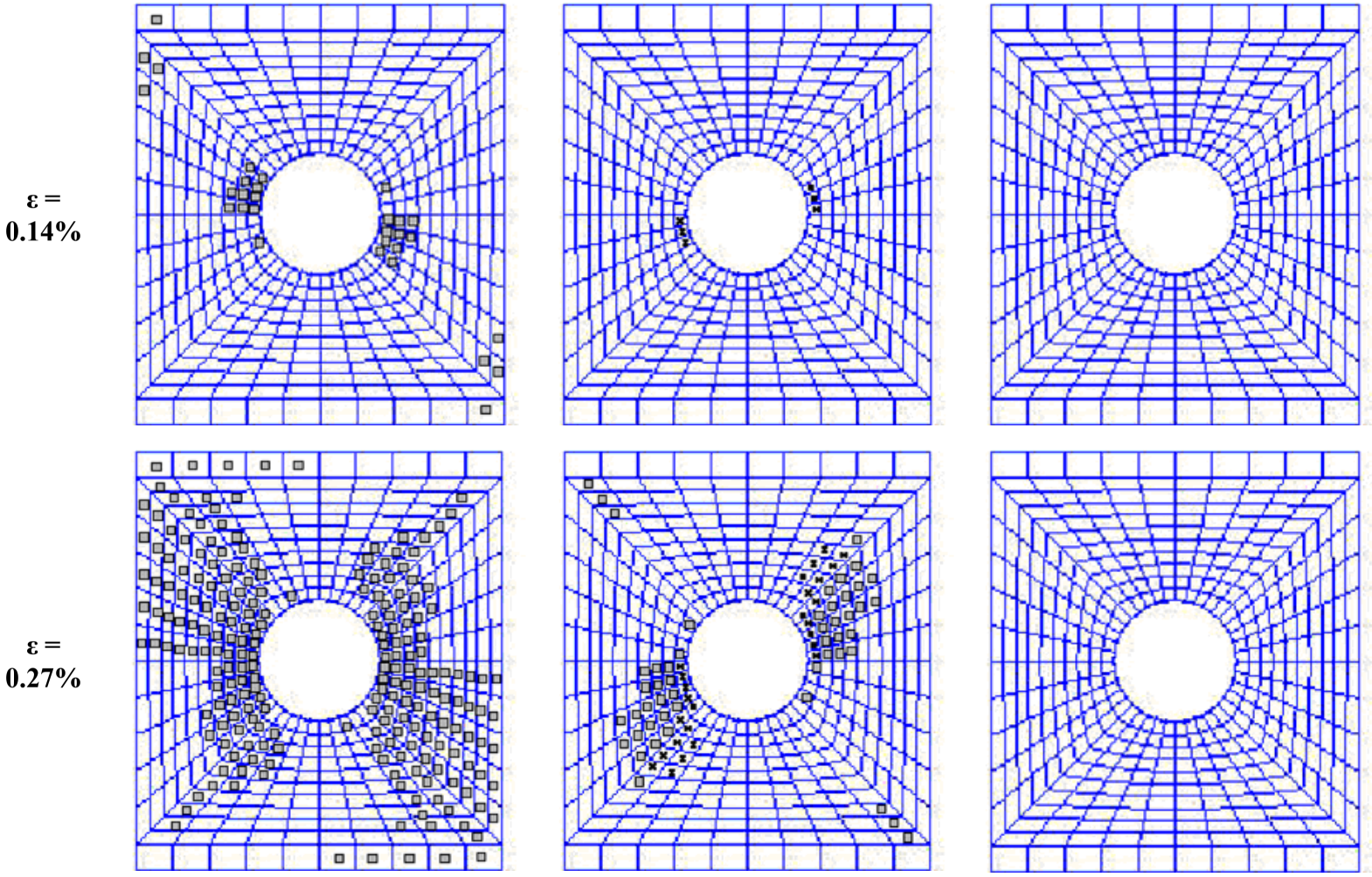

Figure 5-2.10 Predicted progressive damage of a $[0°_3/+45°_3/90°_3/-45°_3]_S$ center-hole strip with D =1/2" under different strain levels tested at room temperature (● = fiber breakage, ▢ = transverse matrix failure and X = shear failure).

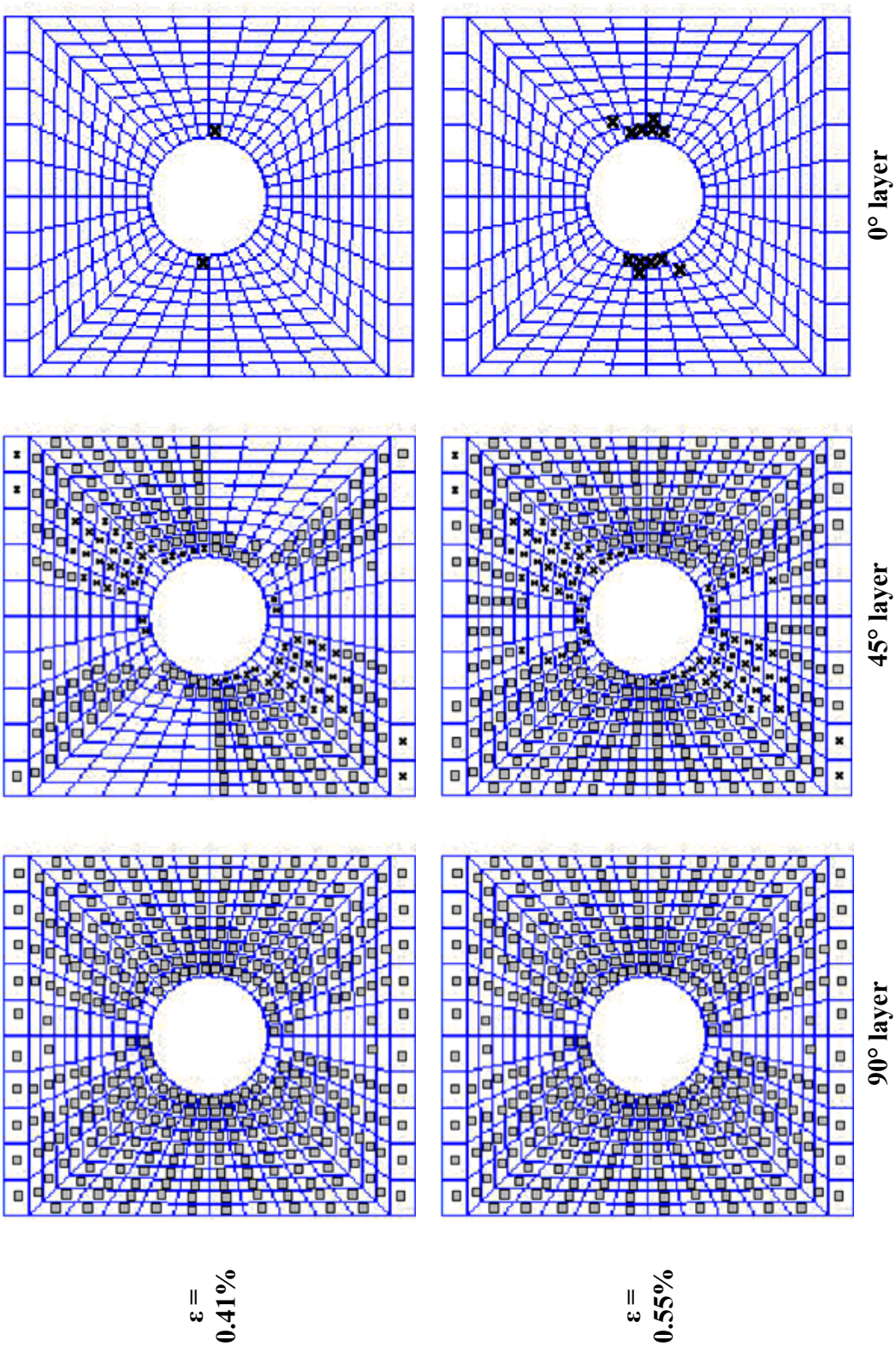

Figure 5-2.10 (continued)

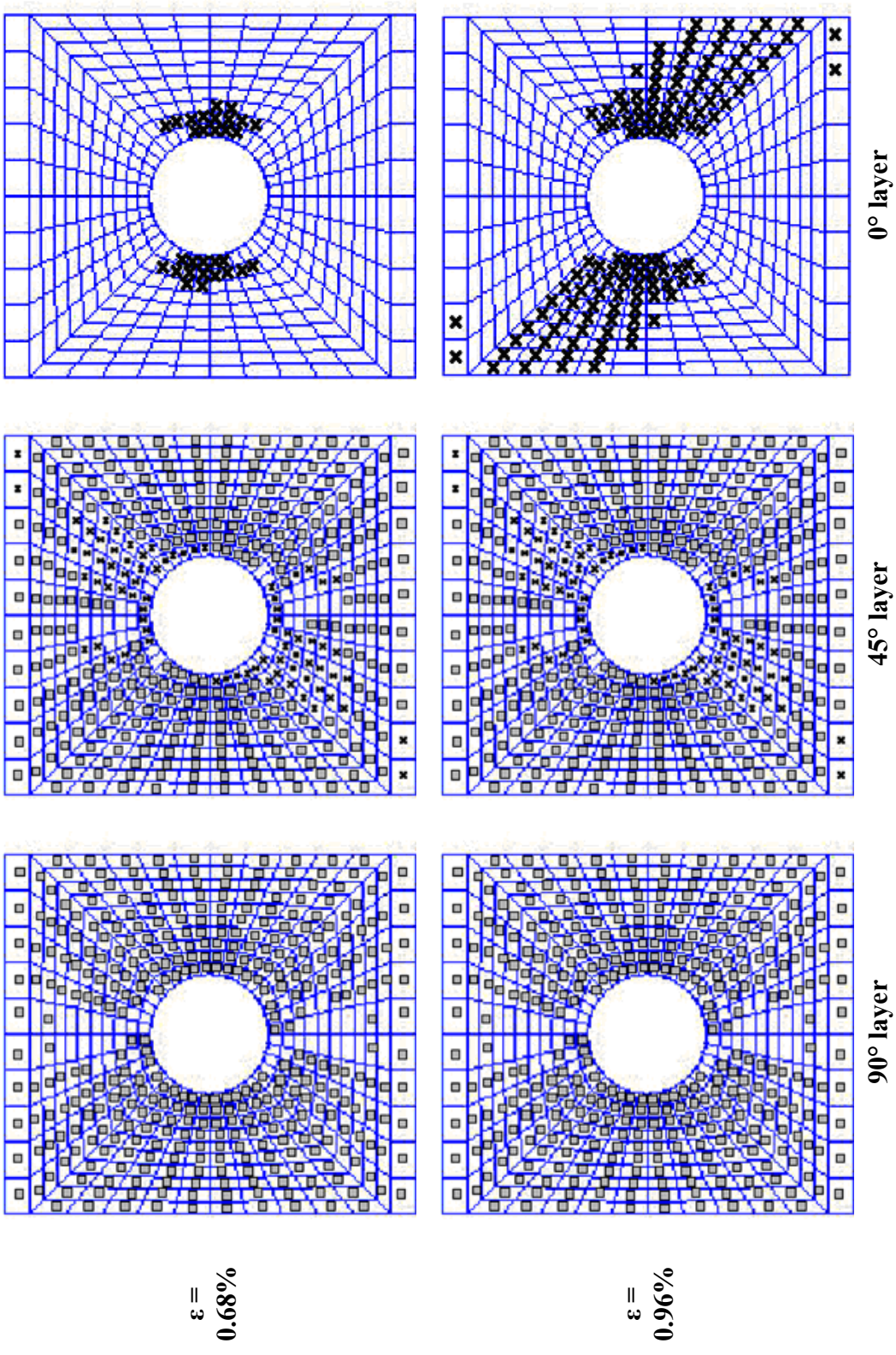

Figure 5-2.10 (continued)

CHAPTER 6

CONCLUSIONS

So far, extensive studies of micromechanical progressive failure of S2 glass/toughened epoxy composites and composite joints have been presented. A number of progressive failure models for this composite have been developed. One of the characteristics of this composite is that the matrix had been toughened. Because of this fact, the failure mode in the 0° direction was found to be fiber breakage when the specimen was under tensile loading as depicted in the microfractographs taken during experiments. This is quite different from other traditional composites, in which matrix cracking is the main failure mode. Based on testing results and photographic records, several progressive failure models have also been proposed to account for different dominant damage modes in S2 glass/toughened epoxy composites with various lay-up configurations. These models were developed based on:

- Simple Mechanics of Materials with the rule of mixtures for dog-bone composite specimens with unidirectional configuration, in which the dominant failure mode is fiber breakage.
- Comprehensive 3-D Elasticity solutions for dog-bone composite specimens with (1) cross-ply configuration, whose dominant failure mode is transverse matrix cracking, (2) angle-ply configuration, whose dominant failure mode is shear failure, and (3) quasi-isotropic configuration, which is dominant by mixed modes of failure.
- Nonlinear elastic orthotropic constitutive laws with damages for composites with stress concentration. The material model can be determined by simple

experiments and implemented easily in commercially available finite element codes.

In addition, more conclusions can be drawn as follows:

- In general the stress-strain curves for all configurations are first linear, then later non-linear due to fiber breaking, transverse matrix cracking, shear cracking, interfacial debonding and/or delamination. As expected the unidirectional configuration has the highest strength followed by the cross-ply, the quasi-isotropic, and finally the angle-ply configuration.
- The layer stacking sequence of specimens (e.g., $[0°_3/90°_3]_{2S}$ *vs.* $[90°_3/0°_3]_{2S}$) has little effect on failure progression.
- Studies of composite strips with a center hole or a pin-joint were also presented. Apparent stress-strain curves were determined for the composite strips with a center hole while applied force *vs*. end elongation curves were obtained for composite joint specimens.
- It was observed that hole/pin size, lay-up configuration, temperature, and the distance between the hole center and the specimen edge greatly affect the strength and stiffness of these composites (with the exception of those tests when slippage occurred.)
- The stiffness, strength and the strain at failure of composite strips increase with a decreasing hole/pin size (again except for those lower temperatures experiments, where slippage occurred.)

- As in dog-bone specimens under uniaxial tension, effect of lay-up configuration on the stiffness, strength and strain at failure obeys the following descending order: $[0^{o}_{3}]_{24\text{-ply}}$, $[0^{o}_{3}/90^{o}_{3}]_{2S}$, $[+45^{o}_{3}/-45^{o}_{3}]_{2S}$, then $[0^{o}_{3}/+45^{o}_{3}/90^{o}_{3}/-45^{o}_{3}]_{S}$.
- In general, as temperature is lower, the stiffness and failure strength increase whereas the strain at failure decreases (excluding the tests during the lower temperatures, where slippage occurred.)
- The apparent strength, stiffness and failure strain all increase with increasing H, the distance from the pin-hole center to the edge of the strip.

In summary, the main contributions of this study are:

- Conducted extensive tests for uniaxial-tension-induced failure progression of S2 glass/toughened epoxy composites and composite strips with a center hole or a pin-joint with various lay-up configurations tested from low to elevated temperatures.
- Developed a simple scheme based on Mechanics of Materials with the rule of mixtures to model the damage progression in unidirectional S2 glass/toughened epoxy composites due to sequential fiber breakage.
- Modified the existent 3-D Elasticity solutions proposed to predict progressive failure processes in S2 glass/toughened epoxy composites of cross-ply, angle-ply or quasi-isotropic configurations, which were dominated by transverse matrix cracking and shear failure.
- Proposed an experimentally-determinable nonlinear elastic orthotropic constitutive law with strain-controlled damage criteria for incorporated into

commercially available finite element codes to predict progressive failure in layered composite structures.

- Verified the afore-mentioned proposed theoretical-numerical models with extensive experimental results in good agreement.

As for the future research plan, the author would like to explore the areas as follows:

- To improve/modify the current theories to cover the entire range of progressive failure of this type of composites under uniaxial tension and with central hole.
- To study numerical models for progressive failure of pin-joint specimens.

CHAPTER 7

REFERENCES

Books

1. *Delaware Composites Design Encyclopedia, Vol. 1-6.* Lancaster, PA: Technomic Publishing Co., Inc. 1989.

2. *The Composite Materials Handbook-MIL 17, Vol. 1, 2 & 3*. Lancaster, PA: Technomic Publishing Co., Inc.

3. Boresi, A. P., Sidebottom, O. M., Seely, F. B. and Smith, J. O. *Advanced Mechanics of Materials*. 3rd Ed. New York: John Wily & Sons, Inc., 1978.

4. Daniel, I. M., and Ishai, O. *Engineering Mechanics of Composite Materials*. New York: Oxford University Press, Inc., 1994.

5. Hyer, M. W. *Stress Analysis of Fiber-Reinforced Composites Materials*. New York: WCB/McGraw-Hill, A Division of The McGraw-Hill Companies, Inc., 1998.

6. Jones, R. M. *Mechanics of Composite Materials*. Washington, D. C.: Scripta Book Company, McGraw-Hill Book Company, 1975.

7. Manual on Experimental Methods for Mechanical Testing of Composites, SEM, Society of Experimental Mechanics, Inc. 1989, Section VB, pp. 105-113.

8. *Nondestructive Evaluation and Flaw Criticality for Composite Materials*, ASTM STP 696, American Society for Testing and Materials, 1978, pp. 97.

9. Tan, S. C. *Stress Concentrations on Laminated Composites*. Lancaster, PA: Technomic Publishing Co., Inc., 1994.

Journals and Papers

10. Aktaş, A., "Bearing strength of carbon epoxy laminates under static and dynamic loading," Composite Structures, 67 (2005) pp. 485-489.

11. Aktaş, A. and Dirikolu, M.H., "An experimental and numerical investigation of strength characteristics of carbon-epoxy pinned-plates" Composite Science and Technology, 2004.64 pp. 1605-1611.

12. Aktaş, A. and Dirikolu, M.H., "The effect of stacking sequence of carbon epoxy composite laminates on pinned-joint strength" Composite Structures 62 (2003) pp. 107-111.

13. Aboudi, J. and Benveniste, Y., "The effective Moduli of Cracked Bodies in Plane Deformations," Engineering Fracture Mechanics, 1987, Vol.26, No. 3, pp. 171-184.

14. Aboudi, J., "Constitutive Relations for Cracked Metal Matrix Composites," Mechanics of Materials 6, 1987, pp. 303-315.

15. Aboudi, J., "Stiffness Reduction of Cracked Solids," Engineering Fracture Mechanics," Vol. 26, No. 5, pp. 637-650, 1987.

16. Aboudi, J., "Wave Propagation in Damaged Composite Materials," Int. J. Solids Structures, Vol. 24, No. 2, pp. 117-138, 1988.

17. Abrate, S. "Matrix Cracking in Laminated Composites: A Review," Review Article, pp. 337-353, 1991.

18. Allen, D. H., Harris, C. E. and Groves, S. E., "A Thermomechanical Constitutive Theory for Elastic Composite with Distributed Damage-II. Application to Matrix Cracking in Laminated Composites," Int. J. Solids Structures, Vol. 23, No. 9, pp. 1319-1338, 1987.

19. Allen, D. H., Harris, C. E., Groves, S. E. and Norvell R. G., "Characterization of Stiffness Loss in Cross-Ply Laminates with Curved Matrix Cracks," Journal of Composite Materials, Vol. 22, No. 01/1988 pp. 71-80.

20. Allen, D. H., Harris, C. H., and Groves, S. E., "A Thermomechanical Constitutive Theory for Elastic Composites with Distributed Damage- I. Theoretical Development," Int. J. Solid Structures, Vol. 23, No. 9, pp. 1301-1318, 1987.

21. Attiogbe, E. K. and Darwin, D., "Self-Consistent Model for Transversely Isotropic Cracked Solid," J. of Engineering Mechanics, Vol.113, No. 7, pp. 984-999. 1987.

22. Auersperg, J., Kieselatein, E., Schubert, A. and Michel, B., "Mixed Mode Interfacial Fracture Toughness Evaluation for Flip-Chip Assemblies and CSP Based on Fracture Mechanics Approaches," Proceedings of 2001 ASME International Mechanical Engineering Congress and Exposition, Nov. 11-16, 2001, New York, New York, IMECE2001/DE-25109.

23. Aveston, J. and Kelly, A., "Tensile First Cracking Strain and Strength of Hybrid Composites and Laminates." Phil. Trans. R. Soc. Lond. A294, 519-534, 1980.

24. Baumann, K. J., Kennedy, W. H., and Herbert, D. L., "Computed Tomography X-Ray Scanning NDE of Graphite/Epoxy Coupons," Journal of Composite Materials, Vol. 18, November 1984, pp. 536-543.

25. Benveniste, Y. and Aboudi, J., "A Continuum Model for Fiber Reinforced Materials with Debonding," Int. J. Solids Structures, Vol.20, No. 11/12, pp. 935-951, 1984.

26. Benveniste, Y., "The Effective Mechanical Behaviour of Composite Materials with Imperfect Contact between the Constituents," Mechanics of Materials 4, 1987, pp. 197-208.

27. Berhan, L., Wang, C. W., and Sastry, A. M., "Damage Initiation in Bonded Particulate Networks: 3D Simulations," Proceedings of 2001 ASME International Mechanical Engineering Congress and Exposition, Nov. 11-16, 2001, New York, New York, IMECE2001/AD-25304.

28. Birman, V. and Byrd, L.W., "Effect of Matrix Cracks on Damping in Unidirectional and Cross-Ply Ceramic Matrix Composites," Journal of Composite Materials, Vol. 36, No. 15/2002, pp. 1859-1877.

29. Bogdanovich, A. E. and Yushanov, S. P., "Progressive Failure Analysis of Adhesive Bonded Joints with Laminated Composite Adherents," Proceedings of 13th Annual Technical Conference on Composite Materials, Sept. 21-23, 1998, Baltimore, Maryland.

30. Budiansky, B. and O'Connell, R., "Elastic Moduli of a Cracked Solid," Int. J. Solids Structures, 1976, Vol.12, pp. 81-97.

31. Camanho, P.P. and Matthews, F.L., "A Progressive Damage Model for Mechanically Fastened Joints in Composite Laminates," J. Composite Materials, Vol.33, 1999, pp. 2248-2280.

32. Chamis, C. C. and Minnetyan, L., "A Multi-Factor Interaction Model (MFIM) for Damage Initiation and Progression," Proceedings of 2001 ASME International Mechanical Engineering Congress and Exposition, November 11-16, 2001, New York, New York, IMECE2001/AD-25301.

33. Chang F. K., Scott, R. A. and Springer, G. S., "Design of Composite Laminates Containing Pin Loaded Holes," Journal of Composite Materials, Vol. 18, May 1984, pp. 279-289.

34. Chang F. K., Scott, R. A. and Springer, G. S., "Failure of Composite Laminates Containing Pin Loaded Holes-Method of Solution," Journal of Composite Materials, Vol. 18, May 1984, pp. 255-278.

35. Chang F. K., Scott, R. A. and Springer, G. S., "Failure of Nonlinearly Elastic Composite Laminates Containing Pin Loaded Holes," Journal of Composite Materials, Vol. 18, September 1984, pp. 464-477.

36. Chang F. K., Scott, R. A. and Springer, G. S., "Strength of Mechanically Fastened Composite Joints," Journal of Composite Materials, Vol. 16, November 1982, pp. 470-494.

37. Chang F. K., Scott, R. A. and Springer, G. S., "The Effect of Laminate Configuration on Characteristic Lengths and Rail Shear Strength," Journal of Composite Materials, Vol. 18, May 1984, pp. 290-296.

38. Chang, F. K. and Chang K. Y., "A Progressive Damage Model For Laminated Composites Containing Stress Concentrations," Journal of Composite Materials, Vol. 21, September 1987, pp. 834-855.

39. Chang, F. K. and Chang K. Y., "Post-Failure Analysis of Bolted Composite Joints in Tension or Shear-Out Mode Failure," Journal of Composite Materials, Vol. 21, September 1987, pp. 809-833.

40. Chang, F. K., "The Effect of Pin Load Distribution on the Strength of Pin Loaded Holes in Laminated Composites," Journal of Composite Materials, Vol. 20, July 1986, pp. 401-408.

41. Chang, F. K., Perez, J. L. and Chang, K. Y., "Analysis of Thick Laminated Composites," Journal of Composite Materials, Vol. 24, August 1990, pp. 801-822.

42. Chen, F., Hiltner, A. and Baer, E., "Damage and Failure Mechanisms of Continuous Glass Fiber Reinforced Polyphenylene Sulfide," Journal of Composite Materials, Vol. 26, No. 15/1992, pp. 2289-2306.

43. Chen, W. H. and Lee, S. S., "Numerical and Experimental Failure Analysis of Composite Laminates With Bolted Joints Under Bending Loads," Journal of Composite Materials, Vol. 29, No. 1/1995, pp. 15-36.

44. Cheng, H. H. and Tsao, C. C., "Delamination Models in Drilling of Composite Materials Using Saw Drill and Candle-Stick Drill," Proceedings of 2001 ASME International Mechanical Engineering Congress and Exposition, November 11-16, 2001, New York, New York, IMECE2001/MED-23308.

45. Cheung, C. K., Liaw, B. M., Delale, F., Walser, A. D. and Raju, B. B., "Bending-Induced Damage in S2 Glass/Toughened Epoxy Composites at Room and Elevated Temperatures," Proceedings of 13th Annual Technical Conference on Composite Materials, Sept. 21-23, 1998 Baltimore, Maryland, pp. 981-990.

46. Cheung, C. K., Long, X., Liaw, B. M., Delale, F., Walser, A. D. and Raju, B. B., "Temperature Effect on Damage in S2 Glass/Toughened Epoxy Composites," Proceedings of DDTCMS Durability and Damage Tolerance of Composite Materials and Structures, 14-19 November, 1999, Nashville TN.

47. Chow, C. L. and Lu, T. J., "On Evolution Laws of Anisotropic Damage," Engineering Fracture Mechanics, Vol. 34, No. 3, pp.679-701, 1989.

48. Christensen, R. M. and Lo, K. H., "Solutions for Effective Shear Properties in Three Phase Sphere and Cylinder Models," J. Mech. Phys. Solids, Vol. 27, pp. 315-330, 1979.

49. Christensen, R. M., "Tensor Transformations and Failure Criteria for the Analysis of Fiber Composite Materials Part II: Necessary and Sufficient Conditions for Laminate Failure," Journal of Composite Materials, Vol. 24, August 1990, pp. 796-800.

50. Christensen, R. M., "Tensor Transformations and Failure Criteria for the Analysis of Fiber Composite Materials," Journal of Composite Materials, Vol. 22, September 1988, pp. 874-897.

51. Daniel, I. M. and Anastassopoulos, G., "Failure Mechanisms and Damage Evolution in Crossply Ceramic-Matrix Composites," Int. J. Solids Structures, Vol. 32, No. ¾, pp. 341-355, 1995.

52. Daniel, I. M. and Lee, J. W., "Damage Development in Composite Laminates under Monotonic Loading," Journal of Composites Technology & Research, JCTRER, Vol.12, No. 2, Summer 1990, pp. 98-102.

53. Daniel, I. M. and Tsai, C. L., "Analytical/Experimental study of Cracking in Composite Laminates under Biaxial Loading," Composites Engineering, Vol. 1, No. 6, pp. 355-362, 1991.

54. Daniel, I. M., Gdoutos, E. E., Abot, J. L. and Wang, K. A., "Effect of loading Conditions on Deformation and Failure of Composite Sandwich Structures," Proceedings of 2001 ASME International Mechanical Engineering Congress and Exposition, Nov. 11-16, 2001, New York, New York, IMECE2001/AMD-25412.

55. Dano, M.L., Gendron, G. and Picard, A., "Stress and failure analysis of mechanically fastened joints in composite laminates," Composite Structures 50 (2000), pp. 287-296.

56. Delale, F., Zhang, H. Q., Liaw, B. M. and Zhang, S. J., "Tensile Damage Behavior of Ceramic Matrix Composites Under High Temperature," AD-Vol.27, Fracture and Damage, ASME 1992, pp. 103-108.

57. Delameter, W. R., Herrmann, G. and Barnett, D. M., "Weakening of an Elastic Solid by a Rectangular Array of cracks," Journal of Applied Mechanics, March 1975, pp.74-80.

58. DeTeresa, S. J. and Larsen, G. J., "Derived Interaction Parameters for the Tsai-Wu Tensor Polynomial Theory of Strength for Composite Materials," Proceedings of 2001 ASME International Mechanical Engineering Congress and Exposition, November 11-16, 2001, New York, New York, IMECE2001/AMD-25417.

59. Dougill, J. W. and Rida, M. A. M., "Further Consideration of Progressively Fracturing Solids," Journal of the Engineering Mechanics Division, EM5, ASCE, October 1980, pp. 1021-1038.

60. Dvorak, G. and Laws, N., "Analysis of Progressive Matrix Cracking in Composite Laminates II. First Ply Failure," Journal of Composite Materials, Vol. 21, April 1987, pp. 309-329.

61. Dvorak, G. J., Laws, N. and Hejazi, M., "Analysis of Progressive Matrix Cracking in Composite Laminates I. Thermoelastic Properties of a Ply with Cracks," Journal of Composite Materials, Vol. 19, No. 05/1985 pp. 216-234.

62. Dwivedi, S. K. and Espinosa, H. D., "Modeling Intersonic Crack Propagation in Fiber Reinforced Composites with Contact/Cohesive Laws," Proceedings of 2001 ASME International Mechanical Engineering Congress and Exposition, November 11-16, 2001, New York, New York, IMECE2001/AD-25313.

63. Ely, T., Armentrout, D. and Kumosa, M., "Evaluation of Stress Corrosion Properties of Pultruded Glass Fiber/Polymer Composite Materials," Journal of Composite Materials, Vol. 35, No. 09/2001, pp. 751-773.

64. Eriksson, I., Möller, P. and Bäcklund, J., "Design of Bolted Composite Laminates, A Special Purpose Finite Element Method of Solution," Computer Methods in Applied Mechanics and Engineering, Vol. 53, pp.139-144, 1984.

65. Etheridge, G. A., Johnson, W. S. and Reeve, S., "Effect of Lay-Up and Constraint on Tensile Notch Strength," Proceedings of 13th Annual Technical Conference on Composite Materials, Sept. 21-23, 1998, Baltimore, Maryland.

66. Fanella, D. and Krajcinovic, D., "Continuum Damage Mechanics of Fiber Reinforced Concrete," Journal of Engineering Mechanics, Vol. 111, No. 8, August 1985, pp. 995-1009.

67. Feng, Z. N., Allen, H. G. and Moy, S. S. J., "Theoretical and Experimental Investigation of Progressive Failure of Woven Composite Panels," Journal of Composite Materials, Vol. 33, No. 11/1999, pp. 1030-1047.

68. Fenske, M. T. and Vizzini, A. J., "The Inclusion of In-Plane Stresses in Delamination Criteria," Journal of Composite Materials, Vol. 35, No. 15/2001, pp. 1325-1342.

69. Fonseka, G. U. and Krajcinovic, D., "The Continuous Damage Theory of Brittle Materials, Part 2: Uniaxial and Plane Response Modes," Journal of Applied Mechanics, December 1981, Vol. 48, pp.816-824.

70. Garbo, S. P. and Ogonowski, J. M., "Strength Predictions of Composite Laminates with Unloaded Fastener Holes," AIAA Journal, Vol. 18, No. 5, May 1980, Article No. 79-0800R, pp. 585-589.

71. Genin, G. M. and Hutchinson, J. W., "Failures at Attachment Holes in Brittle Matrix Laminates," Journal of Composite Materials, Vol. 33, No. 17/1999, pp. 1600-1619.

72. Gommers, B., Verpoest, I. and Van Houtte, P., "Determination of the Mechanical Properties of Composite Materials by tensile Tests. Part II: Strength properties," Journal of Composite Materials, Vol. 32, No. 2/1998, pp. 102-122.

73. Goncalves, W. G. and Almeida, S. F. M., "Strength of Carbon/Epoxy Laminates Containing Pin Loaded Holes," ASME Proceeding, pp.105-111, 1993.

74. Grande, D. H., Mandell, J. F. and Hong, K. C. C., "Fiber-Matrix Bond Strength Studies of Glass, Ceramic and Metal Matrix Composites," Chapman and Hall Ltd, pp.311-328, 1988.

75. Groves, S. E., Harris, C. E., Highsmith, A. L., Allen, D. H. and Norvell, R. G., "An Experimental and Analytical Treatment of matrix Cracking in Cross-Ply Laminates," Experimental Mechanics, March 1987, pp.73-79.

76. Guan, H. and Gibson, R. F., "Micromechanical Models for Damping in Woven Fabric-Reinforced Polymer Matrix Composites," Journal of Composite Materials, Vol. 35, No. 16/2001, pp. 1417-1434.

77. Hahn, H. T. and Tsai, S. W., "On the Behavior of Composite Laminates after Initial Failures," Journal of Composite Materials, Vol. 8, No. 07/1974 pp. 288-305.

78. Hale, D. K., "Review. The Physical Properties of Composite Materials," J. Materials Science Vol. 11, pp. 2105-2141, 1976.

79. Hamada, H., Maekawa, Z. I. and Haruna, K., "Strength Prediction of Mechanically Fastened Quasi-Isotropic Carbon/Epoxy Joints," Journal of Composite Materials, Vol. 30, No. 14/1996, pp. 1596-1612.

80. Harlow, D. G., ”Statistical Properties of Hybrid Composites: Asymptotic Distributions for Strain,” International Journal of Solids and Structures 40 (2003) 6813-6837

81. Harlow, D. G. and Phoenix, S. L., ”The Chain-of-Bundles probability model for the strength of fibrous materials I: analysis and conjectures,” Journal of Composite Materials, Vol.12, 1978, pp. 195-214.

82. Harlow, D. G. and Phoenix, S. L., ”The Chain-of-Bundles probability model for the strength of fibrous materials II: a numerical study of convergence,” Journal of Composite Materials, Vol.12, 1978, pp. 314-334.

83. Harris, C. E., Allen, D. H., Nottorf, E. W. and Groves, S. E., “Modeling Stiffness Loss in Quasi-Isotropic Laminates Due to Microstructural Damage,” Journal of Engineering Materials and Technology, April 1988, Vol. 110, pp.128-133.

84. Harris, D. O., Tetelman, A. S. and Darwish, F. A., “Detection of Fiber Cracking by Acoustic Emission,” Acoustic Emission, ASTM STP 505, American Society for Testing and Materials, 1972, pp. 238-249

85. Hart-Smith, L. J., “Generational of Higher Composite Material Allowables Using Improved Test Coupons,” 36th International SAMPE Symposium, April 15-18 1991, pp. 1029-1044.

86. Hashin, Z. and Rosen, B. W., “The Elastic Moduli of Fiber-Reinforced Materials,” Journal of Applied Mechanics, June/1964, pp.223-232.

87. Hashin, Z. and Shtrikman, S., “A Variational Approach to the Theory of the Elastic Behaviour of Multiphase Materials,” J. Mech. Phys. Solid, 1963, Vol.11, pp. 127-140.

88. Hashin, Z., “Analsis of Cracked Laminates: A Variational Approach,” Mechanics of Materials 4, 1985, pp. 121-136.

89. Hashin, Z., “Assessment of the self Consistent Scheme Approximation: Conductivity of Particulate Composites,” Journal of Composite Materials, Vol. 2, No. 3, July 1968, pp. 284-300.

90. Hashin, Z., “On Elastic Behaviour of Fiber-Reinforced Materials of Arbitrary Transverse Phase,” J. Mech. Phys. Solid, 1964, Vol.13, pp. 119-134.

91. Hashin, Z., “Failure Criteria for Unidirectional Fiber Composites,” Journal of Applied Mechanics, Volume 4, 1980, pp. 329-334.

92. Herakovich, C. T., Aboudi, J., Lee, S. W. and Strauss, E. A., "Damage in Composite Laminates: Effects of Transverse Cracks," Mechanics of Materials 7 1988, pp. 91-107.

93. Highsmith, A. L. and Reifsnider, K. L., "Stiffness-Reduction Mechanisms in Composite Laminates," Damage in Composite Materials, ASTM STP 775, K. L. Reifsnider, Ed., American Society for Testing and Materials, 1982, pp. 103-117.

94. Highsmith, A. L., "Edge Replication for Laminated Composites," NASA tech. Memorandum NASP TM-1014, April 1988.

95. Hill, R., "A Self-Consistent Mechanics of Composite Materials," J. Mech. Phys. Solids, Vol.13, pp. 213-222, 1965.

96. Hill, R., "Elastic Properties of Reinforced Solids: Some Theoretical Principles," Int. J. Solids Structures, 1963, Vol. 11, pp. 357-372.

97. Hill, R., "Theory of Mechanical Properties of Fiber-Strengthened Materials---III Self-consistent Model," J. Mech. Phys. Solid, 1965, Vol.13, pp. 189-198.

98. Hill, R., "Theory of Mechanical Properties of Fiber-Strengthened Materials: I. Elastic Behaviour," J. Mech. Phys. Solid, 1964, Vol.12, pp. 199-212.

99. Hoenig, A., "Elastic Moduli of a Non-Randomly Cracked Body," Int. J. Solids Structures, 1979, Vol.15, pp. 137-154.

100. Hoenig, A., "Near-Tip Behavior of a Crack in a Plane Anisotropic Elastic Body," Engineering Fracture Mechanics, 1981, Vol.16, No. 3, pp. 393-403.

101. Hoenig, A., "The Behavior of a Flat Elliptical Crack in an Anisotropic Elastic Body," Int. J. Solids Structures, 1978, Vol.14, pp. 925-934.

102. Horii, H. and Nemat-Nasser, S., "Overall Moduli of Solids with Microcracks: Load-Induced Anisotropy," J. Mech. Phys. Solid, 1983, Vol.31, No. 2, pp. 155-171.

103. Huang, Z. M., "Modeling Strength of Multidirectional Laminates under Thermo-Mechanical Loads," Journal of Composite Materials, Vol. 35, No. 04/2001, pp. 281-315.

104. Hult, J. and Janson, J., "Material Damage in Structural Analysis," Transactions of the 5th International Conference on Structural Mechanics in Reactor Technology, Berlin, Germany, pp. 13-17, August 1979. L11/1*.

105. Hung, C. L. and Chang, F. K., "Bearing Failure of Bolted Composites Joints. Part II: Model and Verification," Journal of Composite Materials, Vol. 30, No. 12/1996, pp. 1359-1400.

106. Hung, C. L. and Chang, F. K., "Strength Envelope of Bolted Composite Joints under Bypass Loads," Journal of Composite Materials, Vol. 30, No. 13/1996, pp. 1402-1435.

107. Hwang, W. and Hans, K. S.," Cumulative Damage Models and Multi-Stress Fatigue Life Prediction," Journal of Composite Materials, Vol. 20, March 1986, pp. 125-165.

108. Hyer, M. W., Klang, E. C. and Cooper, D. E., "The Effects of Pin Elasticity, Clearance, and Friction on the Stresses in a Pin-Loaded Orthotropic Plate," Journal of Composite Materials, Vol. 21, March 1987, pp. 190-206.

109. İçten, B. and Karakuzu, R., "Progressive failure analysis of pin-loaded carbon-epoxy woven composite plates," Composites Science and Technology 62 (2002), pp. 1259-1271.

110. Ilankamban, R. and Krajcinovic, D., "A Constitutive Theory for Progressively Deteriorating Brittle Solids," Int. J. Solids Structures, Vol. 23, No. 11, pp. 1521-1534, 1987.

111. Irvine, T. B. and Ginty, C. A., "Progressive Fracture of Fiber Composites," Journal of Composite Materials, Vol. 20, No. 03/1986 pp. 166-184.

112. Jiang, Y., Huang, B., Zhao, H. and Lee, C. H., "A Study of Early Stage Self-Loosening of Bolted Joints," Proceedings of 2001 ASME International Mechanical Engineering Congress and Exposition, Nov. 11-16, 2001, New York, New York, IMECE2001/DE-25100.

113. Johnson, P. and Chang, F. K., "Characterization of Matrix Crack-Induced Laminate Failure-Part I: Experiments," Journal of Composite Materials, Vol. 35, No. 22/2001, pp. 2009-2035.

114. Johnson, P. and Chang, F. K., "Characterization of Matrix Crack-Induced Laminate Failure-Part II: Analysis and Verifications," Journal of Composite Materials, Vol. 35, No. 22/2001, pp. 2037-2074.

115. Jong, T. D., "Stresses Around Pin-Loaded Holes in Elastically Orthotropic or Isotropic Plates," Journal of Composite Materials, Vol. 11, July 1977, pp. 313-331.

116. Kachanov, M. L., "A Microcrack Model of Rock Inelasticity Part I: Frictional Sliding on Microcracks," Mechanics of Materials 1, 1982, pp. 19-27.

117. Kachanov, M. L., "A Microcrack Model of Rock Inelasticity Part I: Propagation of Microcracks," Mechanics of Materials 1, 1982, pp. 29-41.

118. Kachanov, M., "Continuum Model of Medium with Cracks," Journal of the Engineering Mechanics Division, EM5, October 1980, pp. 1039-1051.

119. Kallmayer, A. R. and Stephens, R. I., "A Finite Element Model For Predicting Time-Deformations and Damage Accumulation in Laminated Composite Bolted Joints," Journal of Composite Materials, Vol. 33, No. 09/1999, pp. 794-826.

120. Kassapoglou, C. and Lagace, P. A., "Closed Form Solutions For The interlaminar Stress Field in Angle-Ply and Cross-Ply Laminates," Journal of Composite Materials, Vol. 21, April 1987, pp. 292-308.

121. Kawai, M., Yajima, S., Hachinohe, A. and Takano, Y., "Off-Axis Fatigue Behavior of Unidirectional Carbon Fiber-Reinforced Composites at Room and High Temperatures," Journal of Composite Materials, Vol. 35, No. 07/2001, pp. 545-576.

122. Kedlaya, D. N. and Pelegri, A. A., "Failure Prediction of Graphite/Epoxy Laminates with Induced Intermittent Surge in Applied Load during Fatigue," Proceedings of 2001 ASME International Mechanical Engineering Congress and Exposition, Nov. 11-16, 2001, New York, New York, IMECE2001/DE-25310.

123. Kelly, G. and Hallström, S., "Bearing strength of carbon fiber/epoxy laminates: effects of bolt-hole clearance," Composites: Part B 35 (2004), pp. 331-343.

124. Khondker, O. A., Herszberz, I. and Leong, K. H., "An Investigation of the Structure-Property Relationship of Knitted Composites," Journal of Composite Materials, Vol. 35, No. 06/2001 pp. 489-508.

125. Kim, J. K., Kim, D. S. and Takeda, N., "Notched Strength and Fracture Criterion in Fabric Composite Plates Containing a Circular Hole," Journal of Composite Materials, Vol. 30, No. 29/1995, pp. 982-998.

126. Kim, T. J. and Ukadgaonker, V. G., "Plane Stress Analysis of Two Rigid Circular Inclusions," AIAA Journal, Vol. 9, No.11, 1971, pp. 2294-2296.

127. Kim, Y. G., Oh, J. H. and Lee, D. G., "Strength of Adhesively-Bonded Tubular Single Lap Carbon/Epoxy Composite-Steel Joints," Journal of Composite Materials, Vol. 33, No. 20/1999, pp. 1897-1917.

128. Krajcinovic, D. and Fonseka, G. U., "The Continuous Damage Theory of Brittle Materials, Part 1: General Theory," Journal of Applied Mechanics, December 1981, Vol. 48, pp.809-815.

129. Krajcinovic, D. and Sumarac, D., "A Mesomechanical Model for Brittle Deformation Processes: Part I," Journal of Applied Mechanics, March 1989, Vol. 56, pp.51-56.

130. Krajcinovic, D., "Continuous Damage Mechanics Revisited: Basic Concepts and Definitions," Journal of Applied Mechanics, December 1985, Vol. 52, pp.829-834.

131. Krajcinovic, D., "Creep of Structures-A Continuous Damage Mechanics Approach," J. Struct. Mech., 11(1), 1-11, 1983.

132. Krajcinovic, D., Srinivasan, M. G., Fonseka, G. U. and Valentin, R. A., "Progressive Damage of a Spalling Rod," Journal of the Engineering Mechanics Division, EM6, December1982, pp. 1186-1197.

133. Laws, N. and Dvorak, G. J., "Progressive Transverse Cracking In Composite Laminates," Journal of Composite Materials, Vol. 22, October 1988, pp. 900-916.

134. Laws, N., "A Note on Interaction Energies Associated with Cracks in Anisotropic Solids," Philosophical Magazine, 1977, Vol. 36, No. 2, pp. 367-372.

135. Laws, N., "The Overall Thermoelastic Moduli of Transversely Isotropic Composites According to the Self-Consistent Method," Int. J. Engng Sci., Vol. 12, pp. 79-87, 1974.

136. Lee, D. E. and Hahn, H. T., "Computational Modeling of Composite Integral Fit Joints," Proceedings of 13th Annual Technical Conference on Composite Materials, Sept. 21-23, 1998, Baltimore, Maryland.

137. Lee, G. D. and Cho, D. H., "Prediction of the Tensile Load Capability of Co-cured Steel-Composite Tubular Single Lap Joints Considering Thermal Degradation," Journal of Composite Materials, Vol. 34, No. 08/2000, pp. 689-722.

138. Lee, J. W. and Daniel, I. M., "Progressive Transverse Cracking of Crossply Composite Laminates," Journal of Composite Materials, Vol. 24, November 1990, pp. 1225-1243.

139. Lemaitre, J. and Plumtree, A., "Application of Damage Concepts to Predict Creep-Fatigue Failures," Journal of Engineering Materials and Technology, July 1979, Vol. 110, pp.284-292.

140. Lemaitre, J., "A Continuous Damage Mechanics Model for Ductile Fracture," Journal of Engineering Materials and Technology, January 1985, Vol. 107, pp.83-89.

141. Lemaitre, J., "Damage Modelling for prediction of Plastic or Creep Fatigue Failure in Structures," Transactions of the 5th International Conference on Structural Mechanics in Reactor Technology, Berlin, Germany, pp. 13-17, August 1979. L5/1*b.

142. Lessard, L. B. and Shokrieh, M. M., "Two-Dimensional Modeling of Composite Pinned-Joint Failure," Journal of Composite Materials, Vol. 29, No. 05/1995, pp. 671-697.

143. Liaw, B. M., Cheung, C. K., Delale, F., Walser, A. D. and Raju, B. B., "Tension-Induced Damage in S2 Glass/Toughened Epoxy Composites at Room and Elevated Temperatures," Proceedings of 13th Annual ESD Advanced Composites Conference, September. 28-29, 1998, Detroit, Michigan.

144. Liaw, B. M., Zhang, S. J. and Delale, F., "An Experimental technique for Tensile Testing of Ceramic Matrix Composites in SEM at Elevated Temperatures," AD-Vol.29/AMD-Vol. 146, Advances in Experimental Mechanics and Biomimetics, ASME 1992.

145. Lim, S. G. and Hong, C. S., "Prediction of Transverse Cracking and Stiffness Reduction in Cross-Ply Laminated Composites," Journal of Composite Materials, Vol. 23, July 1989, pp. 695-716.

146. Lin, W. H. and Jen, M. H. R., "The Strength of Bolted and Bonded Single-Lapped Composite Joints in Tension," Journal of Composite Materials, Vol. 33, No. 7/1999, pp. 640-666.

147. Liu, D., Raju B.B. and You, J., "Thickness Effects on Pinned Joints for Composites," J. Composite Materials, Vol.33, 2-21, 1999.

148. Lyer, K., Rubin, C. A. and Hahn, G. T., "Three-Dimensional Analysis of Double Rivet-Row Lap Joints- Part I: Non-Countersunk Rivets," Proceedings of 2001 ASME International Mechanical Engineering Congress and Exposition, Nov. 11-16, 2001, New York, New York, IMECE2001/DE-25102.

149. Manne, P. M. and Tsai, S. W., "Design Optimization of Composite Plates: Part I Design Criteria for Strength, Stiffness, and Manufacturing Complexity of Composites Laminates," Journal of Composite Materials, Vol. 32, No. 6/1998, pp. 544-571.

150. Masters, J. E. and Reifsnider, K. L., "An Investigation of Cumulative Damage Development in Quasi-Isotropic Graphite/Epoxy Laminates," Damage in Composite Materials, ASTM STP 775, K. L. Reifsnider, Ed., American Society for Testing and Materials, 1982, pp. 40-62.

151. Meske, R. and Schnack, E., "A Micromechanical Model for X-Ray Stress Analysis of Fiber Reinforced Composites," Journal of Composite Materials, Vol. 35, No 11/2001 pp. 972-998.

152. Mi, Y., Crisfield, M. A. and Davies, A. O., "Progressive Delamination Using Interface Elements," Journal of Composite Materials, Vol. 32, No. 14/1998, pp. 1246-1272.

153. Mikata, Y. and Taya, M., "Stress Field in a Coated Continuous Fiber Composite Subjected to Thermo-Mechanical Loadings," Journal of Composite Materials, Vol. 19, November 1985, pp. 554-578.

154. Nemat-Nasser, S. and Taya, M., "On Effective Moduli of an Elastic Body Containing Periodically Distributed Voids," Quarterly of Applied Mathematics, April 1981, pp.43-59.

155. Nguyen, B. N., "Three-Dimensional Modeling of Damage in Laminated Composites Containing a Central Hole," Journal of Composite Materials, Vol. 31, No. 17/1997, pp. 1672-1693.

156. Noh, J. H. and Whitcomb, J. D., "Progressive Damage Simulation of Thick Viscoelastic Laminate with Homogenization Technique," Proceedings of 2001 ASME International Mechanical Engineering Congress and Exposition, Nov. 11-16, 2001, New York, New York, IMECE2001/AD-25314.

157. Nuismer, R. J. and Labor, J. D., "Applications of the Average Stress Failure Criterion: Part II-Compression," Journal of Composite Materials, Vol. 13, January 1979, pp. 49-60.

158. Nuismer, R. J. and Labor, J. D., "Applications of The Average Stress Failure Criterion: Part I-Tension," Journal of Composite Materials, Vol. 12, January 1978, pp. 238-249.

159. Nuismer, R. J. and Tan, S. C., "Constitutive Relations of a Cracked Composite Lamina," Journal of Composite Materials, Vol. 22, No. 04/1988 pp. 306-321.

160. O'Brien, K. T., "Stiffness Change as a Nondestructive Damage Measurement," Mechanics of Composite Materials," 1981, pp.101-121.

161. Oda, M., "A Method for Evaluating the Effect of Crack Geometry on the Mechanical Behavior of Cracked Rock Masses," Mechanics of Materials 2, 1983, pp. 163-171.

162. Ogin, S. L., Smith, P. A. and Beaumont, P. W. R., "Matrix Cracking and Stiffness Reduction during the Fatigue of a (0/90)s GFRP Laminate," Composites Science and Technology 22, 1985, pp.23-31.

163. Ohki, T, Ikegaki, S., Kurasiki, K., Hamada, H. and Iwamoto, M., "Mechanical Properties of Flat Braided Composites with a Circular Hole," Journal of Engineering Materials and Technology, October 2000, Vol.122, pp. 420-424.

164. Okutan, B., Aslan, Z. and Karakuzu, R., "A study of the effect of various geometric parameters on the failure strength of pin-loaded woven-glass-fiber reinforced epoxy laminate," Composites Science and Technology 61 (2001), pp. 1491-1497.

165. Okutan, B., "The effect of geometric parameters on the failure strength for pin-loaded multi-directional fiber-glass reinforced epoxy laminate," Composites: Part B 33 (2002), pp. 567-578.

166. Okutan, B. and Karakuzu, R., "The strength of pinned joints in laminate composites," Composites Science and Technology 63 (2003), pp. 893-905.

167. Peel, L. D. and Jensen, D. W., "The Response of Fiber-Reinforced Elastomers under Simple Tension," Journal of Composite Materials, Vol. 35, No. 02/2001 pp. 96-137.

168. Peters, P. W. M., "The Strength Distribution of 90o Plies in 0/90/0 Graphite-Epoxy Laminates," Journal of Composite Materials, Vol. 18, November 1984, pp. 545-556.

169. Phoenix, S. L. and Smith, R, L., "A Comparison of Probabilistic Techniques for the Strength of Fibrous Materials Under Local Load-Sharing Among Fibers," International Journal of Solids and Structures 19 (1983) 479-496.

170. Prabhu, S. and Lambros, J., "A Numerical Investigation of Three Dimensional Effects in Cracked Orthotropic Plates," Journal of Composite Materials, Vol. 19, November 1985, pp. 554-578.

171. Rawlinson, R. A., "The Use of Crossply and Angleply Composite Test Specimens to Generate Improved Materials Property Data," 36th International SAMPE Symposium, April 15-18, 1991, pp. 1058-1068.

172. Reifsnider, K. L., Henneke, E. G., Stinchcomb, W. W. and Duke, J. C., "Damage Mechanics and NDE of Composite Laminates," Mechanics of Composite Materials, 1983, pp. 399-420.

173. Rhee, K. and Chi, C. H., "Determination of Fracture Toughness, G_c of Graphite/Epoxy Composites from a Cracked Lap Shear (CLS) Specimen," Journal of Composite Materials, Vol. 35, No. 01/2001 pp. 77-93.

174. Schön, J., "Coefficient of friction of composite delamination surfaces," Wear 237 (2000), pp. 77-89.

175. Schulz, K. C., Packman, P. F. and Eisenmann, J. R., "A Tension-Mode Fracture Model for Bolted Joints in Laminated Composites," Journal of Composite Materials, Vol. 29, No. 1/1995, pp. 37-58.

176. Sehgal, R., Gandhi, O. P. and Angra, S., "Failure Mode Analysis of Rolling Element Bearings," Proceedings of 2001 ASME International Mechanical Engineering Congress and Exposition, Nov. 11-16, 2001, New York, New York, IMECE2001/DE-25115.

177. Shannag, M., Hansen, W. and Tjiptobroto, P., "Interface Debonding in Fiber Reinforced Cement-Matrix Composites," Journal of Composite Materials, Vol. 33, No.02/1999, pp. 158-176.

178. Shimokawa, T., Hamaguchi, Y., Kakuta, Y., Katoh, H., Sanda, T., Mizuno, H. and Toi, Y., "Effect of Isothermal Aging on Ultimate Strength of High-Temperature Composite Materials SST Structures," Journal of Composite Materials, Vol. 33, No. 12/1999, pp. 1104-1118.

179. Shokrieh, M. M. and Lessard, L. B., "Progressive Fatigue Damage Modeling of Composite Materials, Part I: Modeling," Journal of Composite Materials, Vol. 33, No.13/2000, pp. 1056-1080.

180. Shokrieh, M. M. and Lessard, L. B., "Progressive Fatigue Damage Modeling of Composite Materials, Part II: Material Characterization and Model Verification," Journal of Composite Materials, Vol. 33, No.13/2000, pp. 1081-1116.

181. Srolovitz, D. J. and Beale, P. D., "Computer Simulation of Failure in an Elastic Model with Randomly Distributed Defects," Journal of the American Ceramic Society, Vol. 71, No. 5, 1987, pp. 362-369.

182. Sumarac, D. and Krajcinovic, D., "A Mesomechanical Model for Brittle Deformation Processes: Part II," Journal of Applied Mechanics, March 1989, Vol. 56, pp.57-62.

183. Sumarac, D. and Krajcinovic, D., "A self-Consistent Model for Microcrack-Weakened Solids," Mechanics of Materials Vol.6, pp. 39-52, North-Holland 1987.

184. Sun, C. T., Achenbach, J. D. and Herrmann, G., "Continuum Theory for a Laminated Medium," Journal of Applied Mechanics, September 1968, pp. 467-475.

185. Talreja, R., “A Continuum Mechanics Characterization of Damage in Composite Materials,” Proc. R. Soc. Lond. A 399, 195-216, 1985.

186. Talreja, R., “Transverse Cracking and Stiffness Reduction in Composite Laminates,” Journal of Composite Materials, Vol. 19, July 1985, pp. 355-375.

187. Tan, S. C. and Nuismer, R. J., “A Theory For Progressive Matrix Cracking in Composite Laminates,” Journal of Composite Materials, Vol. 23, October 1989, pp. 1029-1047.

188. Tan, S. C., “A Progressive Failure Model For Composite Laminates Containing Openings,” Journal of Composite Materials, Vol. 25, May 1991, pp. 556-577.

189. Tan, S. C., “Laminated Composites Containing an Elliptical Opening. I. Approximate Stress Analyses and Fracture Models,” Journal of Composite Materials, Vol. 21, October 1987, pp. 925-948.

190. Tan, S. C., “Laminated Composites Containing an Elliptical Opening. II. Experiment and Model Modification,” Journal of Composite Materials, Vol. 21, October 1987, pp. 949-968.

191. Tang, S., “Failure of Composite Joints under Combined Tension and Bolt Loads,” Journal of Composite Materials, Vol. 15, July 1981, pp. 329-335.

192. Tandon, G. P. and Kim, R. Y., “Damage Evolution and Failure Modeling in Unidirectional Graphite/Epoxy Composite,” Proceedings of 2001 ASME International Mechanical Engineering Congress and Exposition, Nov. 11-16, 2001, New York, New York, IMECE2001/AD-25302.

193. Tao, J. and Sun, C. T., “Influence of Ply Orientation on Delamination in Composite Laminates,” Journal of Composite Materials, Vol. 32, No. 21/1998, pp. 1933-1947.

194. Tay, T. E., Fink, B. K., Mcknight, S. H., Yarlagadda, S. and Gillespie, J. W. Jr., “Accelerated Curing of Adhesives in Bond Joints By induction Heating,” Journal of Composite Materials, Vol. 33, No. 17/1999, pp. 1643-1664.

195. Thomason, J. L., “The Influence of Fiber Properties on the Properties of Glass-Fiber reinforced Polyamide 6. 6,” Journal of Composite Materials, Vol. 34, No.02/2000, pp. 158-172.

196. Tsai, C. L. and Daniel, I. M., “The Behavior of Cracked Cross-Ply Composite Laminates Under Shear Loading,” Int. J. Solids Structures, Vol. 29, No. 24, 1992, pp. 3251-3267.

197. Tsai, C. L., Daniel, I. M. and Lee, J. W., "Progressive Matrix Cracking of Crossply Composite Laminates Under Biaxial Loading," Proceedings of 1990 the Winter Annual Meeting of ASME, Nov. 125-30, 1990, Dallas, Texas, AMD-Vol.111/MD-Vol.22.

198. Tsai, M. Y. and Morton, J., "Stress and Failure Analysis of a Pin-Loaded Composite Plate: An Experimental Study," Journal of Composite Materials, Vol. 24, October 1990, pp. 1101-1121.

199. Ueng, C. E. and Lin, J. K., "Stress Concentration in Composite Laminates," Journal of Engineering Mechanics, ASCE, Vol. 113, No. 8, August 1987, pp. 1181-1193.

200. Ukadgaonker, V. G., "Stress Analysis of a Plate Containing Two Circular Holes Having Tangential Stresses," Technical Notes, January 1980, pp. 125-128.

201. Vinson, J. R. and Woldesenbet, E., "Fiber Orientation Effects on High Strain Rate Properties of Graphite/Epoxy Composites," Journal of Composite Materials, Vol. 35, No. 06/2001 pp. 509-521.

202. Voyiadjis, G. Z. and Park, T., "Interfacial and Local Damage analysis of Metal Matrix Composites," Damage Mechanics In composites, AMD-Vol. 185, ASME 1994, pp. 87-108.

203. Wang, A. S. D., Chou, P. C. and Lei, S. C., "A Stochastic model for the Growth of Matrix Cracks in Composite Laminates," Journal of Composite Materials, Vol. 18, No. 05/1984 pp. 239-254.

204. Wang, A. S. D. and Crossman, F. W., "Some New Results on Edge Effect in Symmetric Composite Laminate," Journal of Composite Materials, Vol. 11, January 1977, pp. 92-106.

205. Wang, H. S., Hung, C. L. and Chang, F. K., "Bearing Failure of Bolted Composites Joints. Part I: Experimental Characterization," Journal of Composite Materials, Vol. 30, No. 12/1996, pp. 1284-1313.

206. Wang, S. S., Suemasu, H and Chim, E. S. M., "Analysis of Fatigue Damage Evolution and Associated Anisotropic Elastic Property Degradation in Random Short-Fiber Composite," Journal of Composite Materials, Vol. 21, December 1987, pp. 1084-1105.

207. Wei, Q. and Sankar, J., "Understanding the Effects of Processing on the Mechanical Behavior of a Si3N4 Ceramic Through Microstructural Investigations," Proceedings of 2001 ASME International Mechanical Engineering Congress and Exposition, Nov. 11-16, 2001, New York, New York, IMECE2001/MD-24802.

208. Whitney, J. M. and Nuismer, R. J., "Stress Fracture Criteria For Laminated Composites Containing Stress Concentrations," Journal of Composite Materials, Vol. 8, July 1974, pp. 253-265.

209. Whitney, J. M., "Effective Thermo-Elastic Constants of Angle-Ply Laminates Containing 90 Degree Ply Cracks," Journal of Composite Materials, Vol. 35, No. 15/2001, pp. 1373-1391.

210. Whitworth, H.A., Othieno, M. and Batron, O., "Failure analysis of composite pin loaded joints," Composite Structures 59 (2003), pp. 261-266.

211. Willis, J. R., "Bounds and Self-Consistent Estimates for the Overall Properties of Anisotropic Composites," J. Mech. Phys. Solids, 1977, Vol. 25, pp. 185-202.

212. Xiao, Y., Wang, W. X., Takao, Y. and Ishikawa, T., "The Effective Friction Coefficient of a Laminate Composite, and Analysis of Pin-load Plates," Journal of Composite Materials, Vol. 34, No. 01/2000, pp. 69-87.

213. Yang, B. and Mall, S., "Investigation of Damage in Unidirectional Ceramic Matrix Composites Using a Cohesive-Shear-Lag Model," Proceedings of 2001 ASME International Mechanical Engineering Congress and Exposition, Nov. 11-16, 2001, New York, New York, IMECE2001/AD-25300.

214. Yang, C., "Design and Analysis of Composite Pipe joints under Tensile Loading," Journal of Composite Materials, Vol. 34, No. 04/2000, pp. 333-349.

215. Yang, F. and Chow, C. L., "Progressive Damage of Unidirectional Graphite/Epoxy Composite Containing a Circular Hole," Journal of Composite Materials, Vol. 32, No. 06/1998, pp. 504-525.

216. Yokozeki, T., Aoki, T. and Ishikawa, T., "Transverse Crack Propagation in the Specimen Width Direction of CFRP Laminates under Static Tensile Loadings," Journal of Composite Materials, Vol. 36, No. 17/2002, pp. 2085-2099.

217. Yu, L. J. and Davidson, B. D., "A Three-Dimensional Crack Tip Element for Energy Release Rate Determination in Layered Elastic Structures," Journal of Composite Materials, Vol. 35, No. 06/2001 pp. 457-488.

218. Zhang, C., Ganesan, R. and Hoa, S. V., "Effects of Fraction on Three-Dimensional Contact Stresses in Pin-Loaded Laminated Composites," Journal of Composite Materials, Vol. 34, No. 16/2000, pp. 1382-1415.

219. Zhang, K. D., and Ueng, C. E. S., "Stresses Around a Pin-loaded Hole in Orthotropic Plates," Journal of Composite Materials, Vol. 18, September 1984, pp. 432-446.

220. Zhang, S. J., Zhang, H. Q., Delale, F., Liaw, B. M. and Bode, J. H., "Tensile Failure Mechanisms of Ceramic and Polymer Matrix Composites at Room and Elevated Temperatures," MD-Vol.52, Processing, Design and Performance of Composite Materials, ASME 1994.